UNIVERSITY OF CALIFORNIA SAN DIEGO

# High Throughput Point-of-Care Diagnostics in High Traffic Areas/ Using Airflow-Driven, Evaporative Gradients to Improve Sensitivity and Fluid Control in Colorimetric Paper-Based Assays/ Formulation of Lipid Nanoparticles for in-vivo Drug Delivery/ Cold Plasma Treatment of Biomolecules and Adherent Cells

A Dissertation submitted in partial satisfaction of the requirements
for the degree Doctor of Philosophy

in

Materials Science and Engineering

by

Zhilin Guo

Committee in charge:

Professor Yu-Hwa Lo, Chair
Professor Shaochen Chen
Professor Drew Hall
Professor Michael Sailor

2023

The Dissertation of Zhilin Guo is approved, and it is acceptable in quality and form for publication on microfilm and electronically.

University of California San Diego

2023

# DEDICATION

I would like to dedicate my PhD journey to the unwavering support and love of my parents, whose sacrifices and encouragement have been my constant motivation. Their belief in my abilities has sustained me through the long nights and challenging moments of this academic pursuit. To my friends, you have been my pillars of strength, cheering me on through every triumph and comforting me in every setback. Your presence in my life has made this journey not only academically rewarding but also emotionally enriching. I am deeply grateful for the invaluable contributions of my family and friends, without whom this accomplishment would not have been possible. Thank you for being my source of inspiration, and for being there with me every step of the way.

TABLE OF CONTENTS

LIST OF FIGURES

LIST OF TABLES

# LIST OF ABBREVIATIONS

| | |
|---|---|
| LAMP | Loop-mediated isothermal amplification |
| RT-LAMP | Reverse-transcription loop-mediated isothermal amplification |
| LFIA | Lateral flow immunoassay |
| SARS | Severe acute respiratory syndrome coronavirus |
| MERS | Middle East respiratory syndrome coronavirus |
| PCR | Polymerase chain reaction |
| BIP | Backward inner primer |
| FIP | Forward inner primer |
| GUI | Graphical user interface |
| ROI | Region of interest |
| μPADs | Microfluidic paper-based analytical devices |
| POCT | Point-of-care testing |
| BSA | Bovine serum albumin |
| PBS | Phosphate-buffered saline |
| LNPs | Lipid nanoparticles |

# ACKNOWLEDGEMENTS

Chapter 1, in full, is a reprint of the material as it appears in L Waller, Z Guo, R Tang, Z Zhang, E Wang, J Yasuhara-Bell, L Laurent, and YH Lo, “High Sensitivity, Rapid Detection of Virus in High Traffic Environments,” Frontiers in Bioengineering and Biotechnology 10, 2022. The dissertation author was the primary investigator and author of this paper.

Chapter 2, in full, is a revise of the material as it appears in E. Wang, Z. Guo, T. Rui and YH. Lo, “Using Airflow-Driven, Evaporative Gradients to Improve Sensitivity and Fluid Control in Colorimetric Paper-Based Assays,” Lab on a Chip 21, 4249-4261. The dissertation author was the co-author of this paper.

## VITA

2014 Bachelor of Science in Chemical Engineering, University of Illinois, Urbana Champaign

2017 Master of Science in Biomedical Engineering, University of Houston

2019 Master of Science in Materials Science and Engineering, University of California San Diego

2023 Doctor of Philosophy in Materials Science and Engineering, University of California San Diego

## PUBLICATIONS

L Waller, **Z Guo (co-first author)**, R Tang, Z Zhang, E Wang, J Yasuhara-Bell, L Laurent, and YH Lo, "High Sensitivity, Rapid Detection of Virus in High Traffic Environments," *Frontiers in Bioengineering and Biotechnology 10*, 2022

E. Wang, **Z. Guo**, T. Rui and YH. Lo, "Using Airflow-Driven, Evaporative Gradients to Improve Sensitivity and Fluid Control in Colorimetric Paper-Based Assays," *Lab on a Chip 21,* 4249-4261

**Z. Guo**, M. Khorrami and MR. Abidian, "Biofunctionalization of Conducting Polymer Nanotube with Laminin-derived Biomolecules," *Materials Research Society 2018 Spring Meeting*, Phoenix, AR. April 2018 (Abstract accepted)

X. Xie, S.H. Jin, M.A. Wahab, A.E. Islam, C. Zhang, F. Du, E. Seabron, T. Lu, S.N. Dunham, H.I. Cheong, Y.-C. Tu, **Z. Guo**, H.U. Chung, Y. Li, Y. Liu, J.-H. Lee, J. Song, Y. Huang, M.A. Alam, W.L. Wilson and J.A. Rogers, "Microwave Purification of Large-Area Horizontally Aligned Arrays of Single-Walled Carbon Nanotubes," *Nature Communications 5*:5332, DOI: 10.1038/ncomms6332 (2014).

ABSTRACT OF THE DISSERTATION

High Throughput Point-of-Care Diagnostics in High Traffic Areas/ Using Airflow-Driven, Evaporative Gradients to Improve Sensitivity and Fluid Control in Colorimetric Paper-Based Assays/ Formulation of Lipid Nanoparticles for in-vivo Drug Delivery/ Cold Plasma Treatment of Biomolecules and Adherent Cells

by

Zhilin Guo

Doctor of Philosophy in Materials Science and Engineering

University of California San Diego, 2023

Professor Yu-Hwa Lo, Chair

The global pandemic caused by the SARS-CoV-2 virus has underscored the need for rapid, simple, scalable, and high-throughput multiplex diagnostics in non-laboratory settings. Here we demonstrate a multiplex reverse-transcription loop-mediated isothermal amplification (RT-LAMP) coupled with a gold nanoparticle-based lateral flow immunoassay (LFIA) capable of detecting up to three unique viral gene targets in 15 min. RT-LAMP primers associated with three separate gene targets from the SARS-CoV-2 virus (Orf1ab, Envelope, and Nucleocapsid) were added to a one-pot mix. A colorimetric change from red to yellow occurs in the presence of a positive sample. Positive samples are run through a LFIA to achieve specificity on a multiplex three-test line paper assay. Positive results are indicated by a characteristic crimson line. The device is almost fully automated and is deployable in any community setting with a power source.

Microfluidic paper-based analytical devices (μPADs) are foundational devices for point-of-care testing yet suffer from limitations regarding their sensitivity and capability in handling complex assays. Here, we demonstrate an airflow-based, evaporative method that is capable of manipulating fluid flows within paper membranes to offer new functionalities for multistep delivery of reagents and improve the sensitivity of μPADs by 100–1000 times. This method applies an air-jet to a pre-wetted membrane, generating an evaporative gradient such that any solutes become enriched underneath the air-jet spot. By controlling the lateral position of this spot, the solutes in the paper strip are enriched and follow the air jet trajectory, driving the reactions and enhancing visualization for colorimetric readout in multistep assays. The technique has been successfully applied to drive the sequential delivery in multistep immunoassays as well as improve sensitivity for colorimetric detection assays for nucleic acids and proteins via loop-mediated isothermal amplification (LAMP) and ELISA. For

colorimetric LAMP detection of the COVID-19 genome, enrichment of the solution on paper could enhance the contrast of the dye to more clearly distinguish between the positive and negative results to achieve a sensitivity of 3 copies of SARS-Cov-2 RNAs. For ELISA, enrichment of the oxidized TMB substrate yielded a sensitivity increase of two-to-three orders of magnitude when compared to non-enriched samples – having a limit of detection of around 200 fM for IgG. Therefore, this enrichment method represents a simple process that can be easily integrated into existing detection assays for controlling fluid flows and improving detection of biomarkers on paper.

LNPs, with their lipid bilayer structure, protect fragile mRNA, extending circulation and improving cellular uptake. They can be engineered for tissue targeting and controlled release. Mouse models, due to their genetic similarity to humans, are vital for studying LNPs' biodistribution, pharmacokinetics, and therapeutic impact, as well as assessing immune responses. In this thesis, two PDMS microfluidic devices were developed for mRNA encapsulated LNPs, optimizing parameters like size, encapsulation efficiency, and zeta potential. Intraperitoneal and intravenous injections in mouse models quantitatively assessed LNP efficacy and performance.

A groundbreaking high-voltage cold plasma device, paired with advanced cooling, revolutionizing biotechnology. This device enables precise detachment of adherent cells, a milestone in tissue engineering and regenerative medicine. Moreover, it enhances protein binding in ELISA assays, promising higher accuracy in diagnostics, biopharmaceuticals, and life sciences research by manipulating protein-surface interactions. This innovation redefines biotech tools, with far-reaching implications.

# INTRODUCTION

In late December 2019, a significant outbreak of a novel zoonotic coronavirus occurred in Wuhan, Hubei province, China, as reported by Wang et al. (2020). The global spread of COVID-19 has had a profound and transformative impact on the world, with 271,376,643 confirmed cases and 5,324,969 deaths worldwide as of December 16, 2021, according to the World Health Organization (2021).

The rise in novel virus emergence has been associated with socioeconomic expansion and increased travel in the modern era. Examples of notable outbreaks include the 2003 severe acute respiratory syndrome coronavirus (SARS), the 2009 swine flu pandemic, the 2012 Middle East respiratory syndrome coronavirus (MERS) outbreak, the 2013-2016 Ebola epidemic, and the 2015 Zika virus epidemic, as mentioned by Baker et al. (2021). The ease of global transportation, allowing a person with a contagious illness to reach any part of the world within 24 hours, presents a significant global health risk associated with highly contagious outbreaks.

Novel respiratory pathogens, such as SARS-CoV-2, have demonstrated increased transmissibility in high-traffic locations such as airports, train stations, and cruise terminals, as observed by Pavia (2007) and Luo et al. (2021). The combination of a high reproduction number, asymptomatic carriers, superspreading events, socioeconomic globalization, and a population lacking immunity has contributed to the devastating impact of COVID-19 worldwide, as highlighted by Hu et al. (2020).

Rapid diagnostic tests have become crucial in mitigating outbreaks, playing vital roles in initial detection, quarantine procedures, and population-level monitoring, as discussed by Oeschger et al. (2021). Among various diagnostic technologies, reverse transcription quantitative polymerase chain reaction (RT-qPCR) is widely considered the gold standard and is commonly

employed in test centers and hospitals. This technique involves collecting patient samples, extracting RNA, and detecting target viral genome sequences through RT-qPCR. The inclusion of reverse transcription allows for the sensitive and specific diagnosis of RNA viruses, making it suitable for laboratory use (Kralik and Ricchi 2017).

However, RT-qPCR is not practical for many high-traffic community settings due to several factors. The multi-step sample handling process can result in a sample-to-result timeframe of 3-24 hours or longer in clinical diagnostic laboratories, depending on the test center, as noted by Dao Thi et al. (2020). Additionally, RT-qPCR requires specialized laboratory equipment, such as thermocyclers and fluorometers, as well as skilled personnel. Implementing these requirements in community settings, especially in underdeveloped or remote areas, would entail significant equipment, training, and staffing costs.

Isothermal amplification techniques have gained popularity as a means of conducting diagnostic testing outside of laboratory settings, primarily due to their remarkable sensitivity and the ability to perform tests with minimal resources (Sahoo et al., 2016). Among the various isothermal amplification methods available, loop-mediated isothermal amplification (LAMP) is particularly favored. LAMP allows for the amplification of nucleic acids within a temperature range of approximately 65°C, using 4 to 6 primers and a polymerase enzyme capable of displacing DNA strands during replication. In the case of reverse transcription LAMP (RT-LAMP), the process is initiated by reverse transcription using a backward inner primer (BIP) that binds to the 3' end. Simultaneously, a new complementary DNA (cDNA) strand is synthesized through the binding of the B3 primer to the template, facilitated by a strand displacing DNA polymerase. This process forms loops at the 3' end as the single-stranded cDNA molecule binds to itself. Subsequently, the forward inner primer (FIP) binds to the 5' end and, with the assistance

of DNA polymerase, synthesizes another complementary strand. The F3 primer, along with DNA polymerase, binds to the newly synthesized complementary strand and generates a double-stranded DNA molecule while displacing the previous single strand. The amplification products consist of a combination of target RNA and primers. The single-stranded DNA forms structures similar to dumbbells as the ends fold and bind to each other. Exponential amplification of these dumbbell-like structures is then initiated, and the addition of loop primers significantly accelerates the reaction (Huang et al., 2020; Mautner et al., 2020; Thompson and Lei, 2020).

In RT-LAMP assays, the detection of amplified target products often utilizes a colorimetric approach. One commonly used method involves incorporating a pH indicator, such as phenol red, into the reaction mixture, which is carried out in a weakly buffered environment. As the amplification reaction progresses, the pH decreases, leading to a visible color change from red to yellow (Dao Thi et al., 2020). With commercially available pre-mixed reagents for reverse transcription and colorimetric LAMP, such as the WarmStart Colorimetric LAMP 2X Master Mix from New England Biolabs, RT-LAMP becomes an attractive technique for implementation in high-traffic community settings. The colorimetric detection process can be expedited by adding certain chemicals (e.g., guanidine hydrochloride) and primers specific to additional target gene segments of the same virus. Similarly, by multiplexing primers for multiple diseases, it is possible to obtain a single positive or negative result within a single reaction mixture.

To achieve specificity for disease targets within this multiplexed reaction mixture, RT-LAMP can be combined with a lateral flow immunoassay (LFIA). LFIAs offer a promising solution for point-of-care diagnostics due to their low cost, high specificity, and user-friendly nature (Koczula and Gallotta, 2016; Zhu et al., 2020; Chen et al., 2021; Zhang et al., 2021).

Lateral flow assays utilize a paper-based platform where the sample is applied to a test device, and the results are displayed within approximately 10 minutes. The device typically consists of a sample pad, a conjugate pad, a nitrocellulose membrane, and an absorbent pad. The sample is mixed with running buffers and placed onto the sample pad. The conjugate pad contains reporter particles, such as functionalized gold nanoparticles, which bind to the analyte if it is present in a positive sample. Striped lines of antibodies on the nitrocellulose membrane capture the analyte, while a control line captures any excess reporter particles to validate the test. Positive results for the analyte appear as a red line.

In chapter one, a high-throughput, rapid diagnostic system that can be deployed in various high-traffic public settings for the swift detection of up to three gene targets is presented. The method can be easily extended to incorporate additional targets from different organisms. The system utilizes RT-LAMP for isothermal amplification of target sequences, providing a rapid yes or no diagnostic response based on the colorimetric change from red to yellow. Subsequently, the RT-LAMP product is subjected to a lateral flow immunoassay to ensure specificity. In this case, we focus on three gene targets of the SARS-CoV-2 virus (Orf1ab, N, and E), but the diagnostic capability can be broadly applied by substituting the appropriate primers for other viral gene targets.

Microfluidic paper-based analytical devices (μPADs) have emerged as a promising platform for point-of-care testing (POCT). These devices utilize paper as a cost-effective and lightweight substrate for fabricating diagnostic assays. The presence of cellulose fibers in paper enables capillary action, allowing easy liquid wicking without the need for external pumps. This, along with the biocompatibility and versatility in detecting various biomarkers, has contributed to the growing use of μPADs as diagnostic tools.

Among the readout methods employed in μPADs, colorimetric detection has gained significant prominence. In colorimetric assays, the presence of a biomarker is indicated by a color change, typically proportional to its concentration. This color change can be achieved using different detection chemistries such as small-molecule organic indicators, metal nanoparticles, or chromogenic enzyme reactions. Colorimetric assays, providing qualitative or quantitative results, are favored in μPAD research due to their user-friendly nature.

Despite the extensive research in colorimetric detection, there are limitations that have hindered its commercialization. One major limitation is the poor sensitivity, with detection limits significantly lower than those achieved by clinical instruments. The limited sensitivity is attributed to the non-uniform distribution of colorimetric substances and background noise from the paper or sample itself. Various approaches have been proposed to address these issues, focusing on novel methods of color generation and amplification. These include the use of enzyme-nanoparticle conjugates, hybrid metallic and organic nanoparticles, and enhanced metallic nanoparticle staining, aiming to enhance color development and contrast.

Furthermore, the lack of fluid control in basic μPADs has restricted their application to single-reaction assays. To enable more complex assays that require sequential delivery of multiple reagents, both passive and active methods of fluid control have been explored. Passive methods involve physical or chemical modifications of the device, such as dissolvable solutes, physical valves, and geometric adjustments. While passive methods offer simplicity and ease of fabrication, they have limitations in controlling the speed and direction of fluid flow. In contrast, active methods incorporate external inputs for fluid control, utilizing mechanical actuation or geometric transformations to design switches and valves. Active methods provide greater flexibility and precise control over fluids.

In chapter two, an active airflow-based enrichment method that improves fluid control and sensitivity in paper-based colorimetric assays is presented. The method involves directing an airflow nozzle perpendicular to a pre-wetted membrane, creating a differential evaporative gradient. This gradient causes the surrounding liquid to migrate towards the area beneath the airflow, resulting in solute enrichment. By dynamically positioning the airflow across the membrane surface, fluid control and sequential delivery of reagents can be achieved.

We demonstrate the simplicity and flexibility of the airflow enrichment method in colorimetric protein and nucleic acid detection using paper-based ELISA and isothermal reverse transcription loop-mediated isothermal amplification (RT-LAMP) assays. The incorporation of evaporative-induced fluid control serves as a delay valve and switch in a multistep immunoassay, enabling sequential delivery of specific reagents. Additionally, the airflow enrichment of the colorimetric substrate in ELISA and RT-LAMP assays enhances sensitivity and visualization by focusing on a single spot, eliminating the need for alternative color generation systems.

In recent years, the field of pharmaceutical and biomedical research has witnessed a paradigm shift in the realm of drug delivery systems, driven by the development of innovative nanotechnologies. Among these, lipid nanoparticles (LNPs) have emerged as a promising platform for efficient and targeted delivery of therapeutic payloads, including mRNA and small drugs. LNPs offer a multifaceted solution to address challenges associated with conventional drug delivery methods, such as poor bioavailability, non-specific distribution, and limited cellular uptake. This paper delves into the application of lipid nanoparticles for mRNA and small drug delivery within the context of mouse model systems, shedding light on their potential to revolutionize the treatment landscape.

The advent of mRNA-based therapies, exemplified by the groundbreaking success of mRNA vaccines against infectious diseases, has propelled the exploration of LNPs as vehicles for nucleic acid delivery. The unique structure of LNPs, typically comprising a lipid bilayer surrounding an aqueous core, facilitates encapsulation and protection of fragile mRNA molecules. This encapsulation shields mRNA from enzymatic degradation, thus extending its circulation time and enhancing its cellular uptake. Furthermore, LNPs can be engineered to exhibit preferential tissue targeting and controlled release, factors crucial for achieving therapeutic efficacy while minimizing off-target effects.

Mouse model systems, owing to their genetic similarity to humans and the ease of experimental manipulation, have played a pivotal role in elucidating the potential of LNPs in drug delivery. These models provide a dynamic platform to assess the biodistribution, pharmacokinetics, and therapeutic impact of LNP-delivered cargo. By tailoring the composition and surface properties of LNPs, researchers can fine-tune their interactions with immune cells, serum proteins, and target tissues, thus optimizing delivery efficiency. Mouse models also enable the evaluation of immune responses elicited by LNPs, a critical consideration for clinical translation.

In addition to mRNA delivery, LNPs have demonstrated remarkable versatility in carrying small drug molecules. Their ability to encapsulate hydrophobic compounds within the lipid bilayer or the core, and hydrophilic drugs within the aqueous core, provides a platform for enhancing the solubility, stability, and bioavailability of various therapeutic agents. The controlled release kinetics of these encapsulated drugs can be tailored through rational design, allowing for sustained therapeutic levels and reduced dosing frequencies. Mouse models serve as

valuable tools for assessing the therapeutic outcomes and potential toxicities associated with LNP-mediated delivery of small drugs.

In conclusion, the integration of lipid nanoparticles into mRNA and small drug delivery systems represents a transformative approach to address the limitations of traditional drug administration methods. The judicious application of LNP-based strategies in mouse model systems has provided insights into their potential for precision medicine and therapeutic advancement. As this research field continues to evolve, a comprehensive understanding of the interactions between LNPs, therapeutic payloads, and biological systems will undoubtedly pave the way for the development of safer and more effective treatment modalities.

In chapter three, we devised and constructed two distinct PDMS microfluidic devices, each tailored for distinct purposes, namely, the creation of mRNA-encapsulated lipid nanoparticles (LNPs). Various experimental conditions were systematically explored in pursuit of optimizing critical parameters including particle size, encapsulation efficiency, polydispersity index, and zeta potential. Following meticulous analysis, the ensuing step encompassed the administration of both intraperitoneal (IP) and intravenous (IV) injections in a murine model. These injections aimed to quantitatively assess the fluorescence and luminescence intensities of the resultant LNPs, thereby contributing to a comprehensive understanding of their efficacy and performance characteristics.

Plasmas stand as intricate amalgamations of gases undergoing partial ionization, encompassing a diverse array of constituents such as molecules, radicals, neutral and excited entities, ions, photons, and electrons. Within the realm of thermal plasma, often identified as "hot" or "equilibrium" plasma, particles coexist at comparable temperatures while being fully ionized. In contrast, nonthermal plasma, recognized as "cold" or "non-equilibrium" plasma,

induces excited species by elevating the electron temperature beyond that of ions and neutrals. Despite the heightened thermal energy carried by electrons, the overall plasma temperature remains "cold," comfortably below 40°C, allowing for tactile interaction during operational procedures.

A pivotal consequence of cold plasma lies in the prodigious generation of reactive species, including but not limited to reactive nitrogen species (RNS) like NO, NO2, N2O, N2O5, and atomic N; reactive hydrogen species (RHS); and reactive oxygen species (ROS) such as O2, H2O2, O, O3, and OH radicals. Moreover, cold plasma emits electromagnetic radiation, particularly within the spectral domains of vacuum ultraviolet (10-200 nm) and ultraviolet (100-400 nm).

The intricate composition of reactive species within the plasma is dictated by an array of factors, encompassing the composition of the operational gas, equipment configuration, power levels, exposure mode, proximity to the target, duration of exposure, and gas flow rate. Among these factors, the composition of the feed gas emerges as a paramount determinant of the spectrum of reactive species within the discharge, while operational parameters primarily modulate the concentration of reactive species that ultimately impact the target. This interplay is encapsulated within the electron energy distribution function (EEDF), which governs the distribution of electron energies that, in turn, influence the ionization coefficient and excitation rate.

While the initial explorations during the late 1980s and 1990s predominantly centered around the utility of cold plasmas in sterilization, hygiene, and wound healing, contemporary insights have illuminated cold plasma's burgeoning role within the biomedical sphere. Characterized by potent oxidative attributes, cold plasma exhibits the remarkable capacity to

trigger signaling pathways within eukaryotic cells. These pathways orchestrate intricate shifts in cellular physiology, metabolism, growth, aging, and programmed cell death (apoptosis). Intriguingly, nonthermal plasma seems to exert a restrained influence on healthy cells while evoking more pronounced responses in cancerous cells, potentially owing to the hyperactive metabolic pathways distinctive to the latter. This duality offers intriguing prospects for targeted therapeutic applications.

In chapter four, we introduced a pioneering high-voltage power induced cold plasma device, seamlessly integrated with an advanced cooling system. This novel device serves as a versatile tool, harnessed for distinct purposes within the realm of biotechnology. Notably, the device exhibits the capability to effect spatial lift-off of adherent cells, thus facilitating the controlled detachment of cells from substrates. This process holds immense significance in cell culture and manipulation, providing a methodological advancement in the realm of tissue engineering and regenerative medicine.

In tandem with its cell manipulation prowess, the high-voltage power induced cold plasma device has been ingeniously employed to modulate the binding efficiency of proteins in the context of Enzyme-Linked Immunosorbent Assays (ELISA). By judiciously manipulating the interactions between proteins and surfaces, this device serves as a powerful instrument for optimizing the performance of assays that rely on protein-substrate interactions. This innovation opens avenues for enhanced accuracy and sensitivity in biochemical assays, bearing direct relevance to fields encompassing diagnostics, biopharmaceuticals, and basic life sciences research.

CHAPTER 1

# 1 Materials and Methods

## 1.1 Automated System Architecture

A customized machine is utilized to automate all steps beyond the loading of patient samples. The machine leverages an existing pipetting robot (OT2-Pipettes, Opentrons, Long Island City, NY, USA) for precision liquid transfer. Customized 96-well plate holders and cassette holders driven by stepper motors are used to convey 96-well plates and LFIA cassettes into and out from the machine. Position sensors are installed to ensure precision and repeatability. A customized heating unit is installed under the 96-well plate to enable LAMP reaction heating. The colorimetric reaction readouts are detected using an overview camera (Flea3 USB3, Model: FL3-U3-13E4C-C, Teledyne FLIR LLC). A process chiller unit (Temperature Module, Opentrons) is adopted for liquid storage (e.g., LAMP reagents).

The machine is controlled by a desktop computer and a two-level user interface. The first level user interface opens to the system developers, which includes the system installation and calibration access. After initial installation and calibration, the second level user interface is opened to system operators for information loading and result display. Given the simplicity of the graphical user interface (GUI), system operators can be trained in minutes.

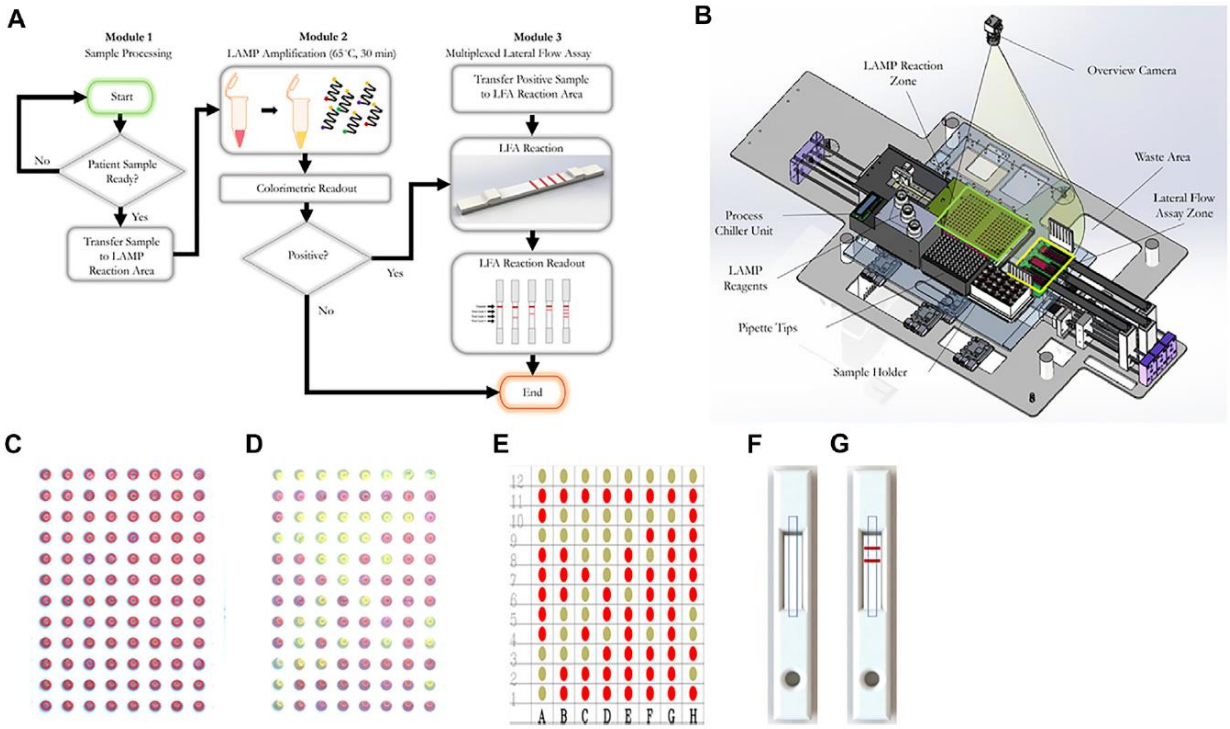


Figure 1.1 The workflow of our RT-LAMP-LFIA prototype system and the schematic of our automatic system. (A) Workflow schematic from initial patient sample placement to end. Samples undergo a colorimetric loop-mediated isothermal amplification reaction. Samples that are positive (as indicated by a colorimetric change from red to yellow) are transferred to a multiplexed lateral flow assay test strip, which can differentiate from up to three target sequences. (B) Machine schematic (C) Example 96-well plate image captured by the overview camera before RT-LAMP reaction. The red circle represents the region of interest (ROI) of each well. The decision matrix is determined by the color change within the red circles (D) Example 96-well plate image captured by the overview camera after RT-LAMP reaction. (E) Final decision matrix for RT-LAMP reaction readout (F) Example rendering of LFIA cassette image captured by the overview camera before LFIA. Dashed rectangles represent ROIs of the LFIA cassettes. (G) Example rendering of LFIA cassette image captured by the overview camera after LFIA.

## 1.2 System Automation and Overarching Workflow

Nasopharyngeal swabs are collected from patients using a nasal swab and stored in iSwab Microbiome-EL (Extraction-Less) buffer (MAWI DNA Technologies, Hayward, CA, USA). Collected patient samples are loaded into the sample holder by a human operator (Fig. 1.1B). All reagents are stored on top of the process chiller unit. Upon initialization, 96-well plates and

cassettes filled with LFIA are conveyed into the LAMP reaction zone and the lateral flow assay zone, respectively. After the system operator enters the sample information (e.g., number of samples, sample identification numbers), the machine first loads the pre-mixed LAMP reaction concoction (Table 1.1, Table 1.2) into a new 96-well plate. Next, the machine pipettes 2 µL of each patient sample into a single well in the 96-well plate. Pipette tips are changed after each sample to prevent cross-contamination of samples. Once all samples are loaded, the heating unit under the LAMP reaction zone heats the plate up to 65℃. A system timer starts once it reaches 65℃. After a preset reaction time (15 - 30 minutes), the RT-LAMP reaction is complete and positive samples are clearly identifiable by a colorimetric change from red to yellow. The colorimetric change is detected and quantitatively measured by the overview camera (Flea3 USB3, Model: FL3-U3-13E4C-C, Teledyne FLIR LLC), and the process is complete for samples that meet the threshold for a negative result. For samples that meet the criteria for a positive result, 3 µL of the LAMP product is mixed with 40 µL of running buffer (1x PBS, pH 7.4 with 2% Tween 20) and deposited onto a lateral flow immunoassay. A system timer begins, and the result is detected and quantified after a predetermined amount of time. On the lateral flow immunoassay, positive results for each specific viral gene target will appear as a characteristic crimson line. A fourth crimson line acts as a control line and serves to validate the test. The positive readings which stand for the presence of COVID-19 RT-LAMP products are visible after 5 to 10 min using the LFIA. The colorimetric change of the LFIA is detected using the overview camera and then quantitatively measured on the computer. The result for each sample is displayed on the user interface and a Portable Document Format (PDF) file including the sample information and detection results will be automatically stored in the local disk (or on the cloud if internet access is enabled). The system automatically displays a warning window on the

user interface for 96-well plates and cassettes replenishment when needed (e.g., all the wells have been used).

Table 1.1 Concentrations of each oligonucleotide in the 10× primer mix.

| Primer | 10× Concentration (stock) | 1 (μM) X Concentration (final) |
|---|---|---|
| F (μM)IP | 16 | 1.6 |
| BIP | 16 | 1.6 |
| F3 | 2 | 0.2 |
| B3 | 2 | 0.2 |
| LF | 8 | 0.8 |
| LB | 8 | 0.8 |

Table 1.2 Concentrations of each reagent in the RT-LAMP assay.

| Reagents Volume (µl) | Reagents Volume (µl) |
|---|---|
| WarmStart Colorimetric LAMP 2X Master Mix 10 | 10 |
| LAMP Primer Mix (10X) 2 | 2 |
| Guanidine Hydrochloride 2 | 2 |
| Nasopharyngeal Swab Sample 2 | 2 |
| dH2O 4 | 4 |
| Total Volume 20 | 20 |

### 1.3 Quantification of the RT-LAMP reaction and LFIA readout

For the RT-LAMP reaction readout, after loading the new 96-well plates, the system first identifies the region of interest (ROI) of all wells. The RT-LAMP colorimetric readout is determined based on the color change within the ROI of each well. Two images are captured, one prior to the RT-LAMP reaction and one after the RT-LAMP reaction. YUV color space is used to compare the difference between two images. Wells that exceed the threshold are considered positive samples. Figure 1.1 (C) and (bD) show an example image captured before and after the RT-LAMP reaction, respectively. The RT-LAMP reaction detection result is shown in Figure 1.1 (E).

For the LFIA readout, after loading the LFIA cassettes, the system will first identify the ROI of each LFIA cassette. The LFIA colorimetric readout is determined by the appearance or

lack thereof of a crimson line within the ROI. Two images are captured, one prior to the LFIA reaction and one after the LFIA reaction. For each image, mean intensity along the width direction is obtained, which compresses the ROIs into two decision lines. YUV color space is used to compare the color difference between two lines. The final LFIA readout is obtained from the peak detection result from the YUV color space difference. Figure 1 (dF) and (G) show an example rendered image captured before and after the LFIA reaction, respectively.

### 1.4 RT-LAMP Primer Design and Viral Targets Information

RT-LAMP primers against Nucleocapsid (N-2), Envelope (E-2), and ORFla-1 genes (Table 1.3) were designed according to previously published specifications (Yinhua Zhang et al. 2020) and were synthesized by Integrated DNA Technologies (IDT, San Diego, CA, USA). The sequence of primers and concentrations of each oligonucleotide in the 10x primer mix are shown in Tables 1 and 2. The 10x primer mix was prepared by dissolving the oligonucleotides in nuclease-free water. It was stored at -20 ℃ before use.

The RT-LAMP primer sets corresponding to the N-2, E-2, and ORF1a-1 genes were each designed to incorporate a unique tag onto each amplified RT-LAMP product. Texas Red was labeled on the 5’ end of the E-2 LF primer, FITC was labeled on the 5’ end of the N-2 FIP primer, and Digoxigenin was labeled on the 5’ end of the ORF1a-1 FIP primers. Biotin was labeled on the 5’ end of the LB primers for all three genes. Accordingly, Anti-Texas Red, Anti-Fluorescein, and Anti-Digoxigenin antibodies were stripped onto the nitrocellulose membrane of the LFIA as test lines, while the biotin-BSA was used as the control line. Leveraging the natural affinity of streptavidin to biotin, which is one of the strongest non-covalent interactions in nature, streptavidin gold nanoparticles (Streptavidin, 40nm 10 OD Colloidal Gold, Attogene, TX, USA) served as the reporter particle. Therefore, the RT-LAMP products for each gene only bind to one

test line, enabling the detection of up to three distinct viral gene target detections on a single LFIA. Because in this instance all three gene targets were from RNA from the same virus and thus competition between templates can occur, gene blocks (sub-sequences of the entire SARS-CoV-2 RNA template) are used to validate the test. In the clinical and contrived viral tests, competition between primer sets can obscure some gene sequences on the LFIA; however, the RT-LAMP colorimetric change from red to yellow will be unaffected.

Table 1.3 Primer sequences against Nucleocapsid (N-2), Envelope (E-2), and Orf1a-1 genes of the SARS-CoV-2 virus.

| Gene target | Primer | Name | Tag | Sequence |
|---|---|---|---|---|
| N2 | FIP | N2 FIP | 5'-FITC | TGCGGCCAATGTTTGTAATCAGCCA AGGAAATTTTGGGGAC |
| | BIP | N2 BIP | - | CGCATTGGCATGGAAGTCACTTTGA TGGCACCTGTGTAG |
| | F3 | N2 F3 | - | AACACAAGCTTTCGGCAG |
| | B3 | N2 B3 | - | GAAATTTGGATCTTTGTCATCC |
| | LF | N2 LF | - | TTCCTTGTCTGATTAGTTC |
| | LB | N2 LB | 5'-Biotin | ACCTTCGGGAACGTGGTT |
| Orf1a | FIP | Orf1a FIP | 5'- DigN | GAGGGACAAGGACACCAAGTGTAT GGTTGAGCTGGTAGCAGA |
| | BIP | Orf1a BIP | - | CCAGTGGCTTACCGCAAGGTTTTAG ATCGGCGCCGTAAC |

Table 1.3 Primer sequences against Nucleocapsid (N-2), Envelope (E-2), and Orf1a-1 genes of the SARS-CoV-2 virus.

| | | | | |
|---|---|---|---|---|
| | F3 | Orf1a F3 | - | CTGCACCTCATGGTCATGTT |
| | B3 | Orf1a B3 | - | AGCTCGTCGCCTAAGTCAA |
| | LF | Orf1a LF | - | CCGTACTGAATGCCTTCGAGT |
| | LB | Orf1a LB | 5'-Biotin | TTCGTAAGAACGGTAATAAAGGAGC |
| E2 | FIP | E2 FIP | - | ACCTGTCTCTTCCGAAACGAATTTGT AAGCACAAGCTGATG |
| | BIP | E2 BIP | - | CTAGCCATCCTTACTGCGCTACTCAC GTTAACAATATTGCA |
| | F3 | E2 F3 | - | CCGACGACGACTACTAGC |
| | B3 | E2 B3 | - | AGAGTAAACGTAAAAAGAAGGTT |
| | LF | E2 LF | 5'- TexRed | TCGATTGTGTGCGTACTGC |
| | LB | E2 LB | 5'-Biotin | TGAGTACATAAGTTCGTAC |
| | | | | |

The SARS-CoV-2 RNA (VR-3280SD) was purchased from the American Type Culture Collection (ATCC, Manassas, Virginia, USA). The COVID-19 RNA was diluted as necessary by nuclease-free water. The Nucleocapsid (N), Envelope (E), and ORF1ab gene blocks were synthesized by Integrated DNA Technologies (IDT, IA, USA), shown in Table 1.4.

Table 1.4 Sequences of N, E, and Orf1ab gene blocks.

| Gene blocks | Sequence |
|---|---|
| N gene (229 nt) | AACACAAGCTTTCGGCAGACGTGGTCCAGAACAAACCCAAG GAAATTTTGGGGACCAGGAACTAATCAGACAAGGAACTGAT TACAAACATTGGCCGCAAATTGCACAATTTGCCCCCAGCGCT TCAGCGTTCTTCGGAATGTCGCGCATTGGCATGGAAGTCACA CCTTCGGGAACGTGGTTGACCTACACAGGTGCCATCAAATTG GATGACAAAGATCCAAATTTC |
| E gene (234 nt) | CCGACGACGACTACTAGCGTGCCTTTGTAAGCACAAGCTGAT GAGTACGAACTTATGTACTCATTCGTTTCGGAAGAGACAGGT ACGTTAATAGTTAATAGCGTACTTCTTTTTCTTGCTTTCGTGG TATTCTTGCTAGTTACACTAGCCATCCTTACTGCGCTTCGATT GTGTGCGTACTGCTGCAATATTGTTAACGTGAGTCTTGTAAA ACCTTCTTTTTACGTTTACTCT |
| Orf1ab gene (289 nt) | TCCAGATGAGGATGAAGAAGAAGGTGATTGTGAAGAAGAAG AGTTTGAGCCATCAACTCAATATGAGTATGGTACTGAAGATG ATTACCAAGGTAAACCTTTGGAATTTGGTGCCACTTCTGCTG CTCTTCAACCTGAAGAAGAGCAAGAAGAAGATTGGTTAGAT GATGATAGTCAACAAACTGTTGGTCAACAAGACGGCAGTGA GGACAATCAGACAACTACTATTCAAACAATTGTTGAGGTTCA ACCTCAATTAGAGATGGAACTTACACCAGTTGTTCAGACT |

## 1.5 Lateral Flow Immunoassay

The lateral flow immunoassay (LFIA) (Fig.1.2) was comprised of a conjugate pad (GFCP203000 Glass Fiber Conjugate Pad Sheets, Millipore Sigma, St. Louis, MO, USA), a nitrocellulose membrane (Whatman FF120HP, Cytiva Life Sciences, Marlborough, MA, USA), an absorbent pad (Blotting Paper, Grade 222, Ahlstrom-Munksjö, Helsinki, Finland), and a backing card (DCN Diagnostics, Carlsbad, CA, USA).

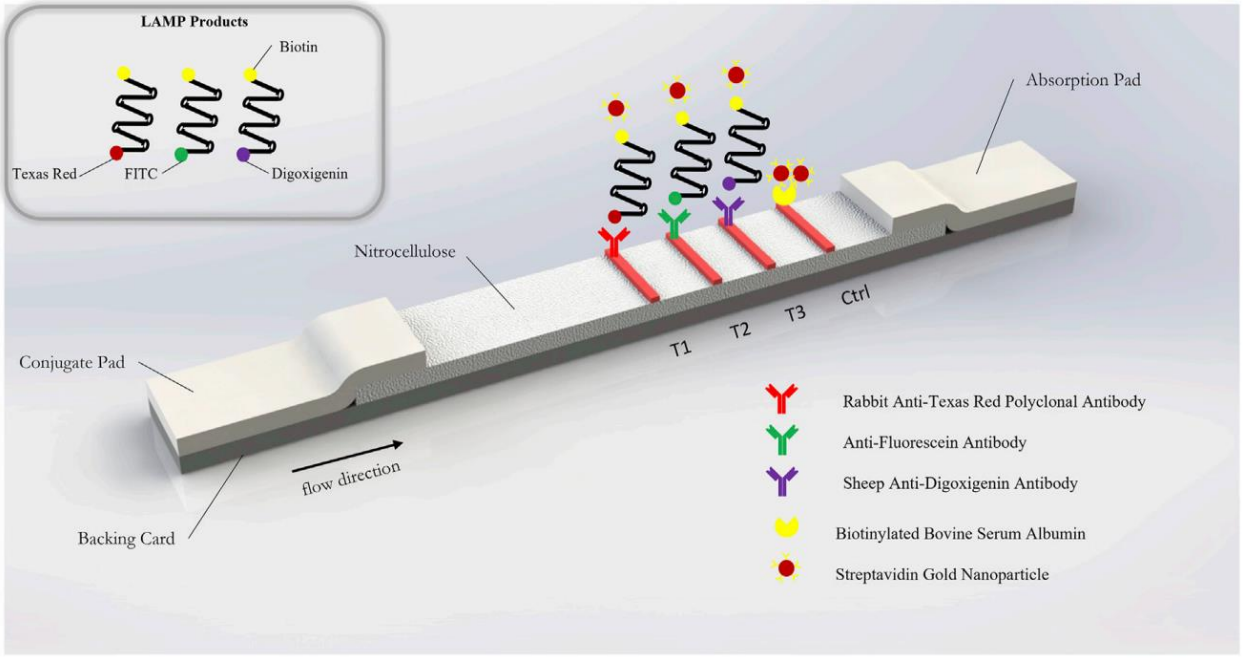


Figure 1.2 Schematic of gold nanoparticle based lateral flow immunosorbent assay for the detection of SARS-CoV-2 Orf1a, N2, and E2 target genes.

The dimensions of the conjugate pad were 2 cm x 30 cm; the dimensions of the nitrocellulose membrane were 2.5 cm x 30 cm; the dimensions of the absorbent pad were 2 cm x 30 cm); and the dimensions of the backing card were 6 cm x 30 cm. The conjugate pad was soaked in a blocking solution (1% bovine serum albumin + .05% Tween 20 + 0.2% sucrose, diluted in PBS) on a shaker at low speed for 10 min and the conjugate pads were dried on a drying rack overnight. Anti-texas red antibody (anti-TexR, 1 mg/ml, Cat. # A-6399,

ThermoFisher Scientific, Waltham, MA, USA), rabbit anti-fluorescein antibody (anti-FITC, 1 mg/ml, Cat. # ab19491, Abcam, Cambridge, UK), sheep anti-digoxigenin antibody (anti-DigN, 2.5 mg/ml, Cat. # 3210-0488, Bio-Rad, Hercules, CA, USA) and biotinylated bovine serum albumin (biotin-BSA, 3 mg/ml, Cat. #B-2007-10, Vector Labs, Burlingame, CA, USA) were stripped at the detection regions on the nitrocellulose using a lateral flow reagent dispenser (Claremont Biosolutions, Upland, CA, USA) at test line 1 (TL1), test line 2 (TL2), test line 3 (TL3) and control line (Ctrl), respectively, with each line separated by 5 mm. The membranes were then assembled and the assembled LFIA were cut into 4-mm dipsticks. Then, 3 µL of streptavidin gold nanoparticles (Streptavidin, 40nm 10 OD Colloidal Gold, Attogene, TX, USA) were immobilized at one end of the conjugate pad for each strip and dried in a vacuum. The dipsticks were packaged in a plastic cassette (DCNDx, Carlsbad, CA, USA) and stored in a 4°C fridge in a heat-sealed foil packet with a silica gel desiccant until use. The LFIAs were tested three months later and found to still be viable.

### 1.6 Quantification of the RT-LAMP Reaction and LFIA Readout

The colorimetric change of the RT-LAMP reaction is quantitatively measured by the overview camera (Flea3 USB3, Model: FL3-U3-13E4C-C, Teledyne FLIR LLC). The prototype algorithm identifies the region of interest (ROI) of all RT-LAMP wells in the 96-well plate. The grayscale and red values of each well are evaluated inside the ROI. In each batch, at least three negative samples are present to serve as negative controls. The average value of the red/grayscale value of these negative controls are used to normalize the red/grayscale value for every well. Intuitively, a larger red/grayscale value means that the sample is redder, corresponding to a negative result of colorimetric RT-LAMP. A smaller red/grayscale value means that the sample is less red – and thus a colorimetric change from red to yellow has

occurred. Accordingly, our algorithm assigns a cutoff value of >0.98 for negative samples and <0.98 for positive samples. Independently, the same algorithm was employed using the built-in tools of ImageJ for quantification for the experiments denoted in the Results section.

### 1.7 Clinical Sample Handling and RT-qPCR

Clinical samples were obtained from the UCSD COVID-19 Research Biobank (University of California, San Diego, CA, USA). Nasopharyngeal swabs from patients both positive and negative for the SARS-CoV-2 virus were collected in iSwab Microbiome-EL (Extraction-Less) buffer. Collected samples were aliquoted into freezer tubes in a BSL2+ hood and were stored at -80°C prior to use. RT-qPCR was performed on all samples. Cq values are noted in Table 1.5.

Table 1.5 Cq values obtained from RT-QPCR for clinical nasopharyngeal specimens.

| Sample number | Test result | Cq value |
|---|---|---|
| 1-30 | Negative | Undetectable |
| 31 | Positive | 27.514 |
| 32 | Positive | 33.405 |
| 33 | Positive | 25.0205 |
| 34 | Positive | 27.708 |
| 35 | Positive | 28.526 |
| 36 | Positive | 32.840 |

Table 1.5 Cq values obtained from RT-QPCR for clinical nasopharyngeal specimens.

| | | |
|---|---|---|
| 37 | Positive | 27.422 |
| 38 | Positive | 32.859 |
| 39 | Positive | 30.810 |
| 40 | Positive | 29.406 |
| 41 | Positive | 27.204 |
| 42 | Positive | 32.703 |
| 43 | Positive | 35.175 |
| 44 | Positive | 25.782 |
| 45 | Positive | 21.299 |
| 46 | Positive | 34.516 |
| 47 | Positive | 26.791 |
| 48 | Positive | 31.589 |
| 49 | Positive | 27.127 |
| 50 | Positive | 25.745 |
| 51 | Positive | 26.304 |
| 52 | Positive | 26.203 |

Table 1.5 Cq values obtained from RT-QPCR for clinical nasopharyngeal specimens.

| | | |
|---|---|---|
| 53 | Positive | 31.114 |
| 54 | Positive | 34.482 |
| 55 | Positive | 33.929 |
| 56 | Positive | 28.251 |
| 57 | Positive | 34.532 |
| 58 | Positive | 35.496 |
| 59 | Positive | 33.400 |
| 60 | Positive | 31.301 |

# 2 Results

## 2.1 Time-to-Result Test

WarmStart Colorimetric LAMP 2X Master Mix and guanidine hydrochloride solution (New England Biolabs, Ipswich, MA, USA) were used to detect the SARS-CoV-2 RNA template. The RNA template was diluted by nuclease-free water into samples with 3, 5, 10, 25, 50, 100, and 1000 genome copies/ well. The three custom RT-LAMP primers against Nucleocapsid (N-2), Envelope (E-2), and ORFla-1 genes (Table 3) were mixed. The colorimetric RT-LAMP reaction was conducted at 65℃ and imaged after 15 minutes and 30 minutes. The test demonstrated a sensitivity of 3 copies/well of SARS-CoV-2 RNA template after 15 minutes, as

observed by the red to yellow color change, while the negative sample stayed red after the reaction (Figure 1.3). The 30-minute time point was chosen for subsequent experiments to allow ample time for the reaction to proceed to completion.

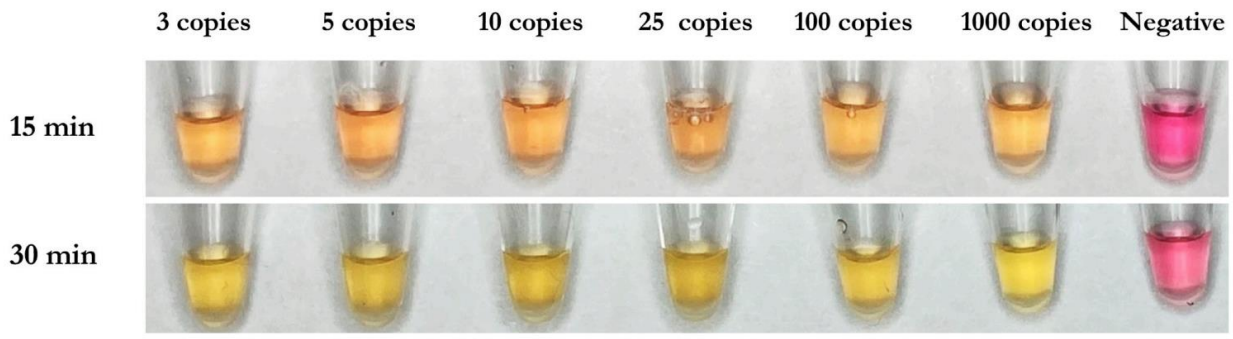


Figure 1.3 Demonstrative colorimetric loop-mediated isothermal reaction using primers as listed in Table 1. Viral RNA from SARS-CoV-2 (ATCC) were spiked in the amounts of 0, 3, 5, 10, 25, 100, and 1000 RNA copies per microwell and reactions were imaged after 15 and 30 minutes, respectively.

## 2.2 Multiplexed Gene Detection by Colorimetric RT-LAMP and LFIA

Using each single gene block (N, E, and Orf1ab), RT-LAMP reactions were carried out in triplicate with all three primers present. Following the reaction, 3 µL of LAMP product was applied to the sample region of the LFIA with 40 µL of running buffer. As expected, only one positive line relative to the corresponding amplified RT-LAMP product was observed on each strip, confirming that in the presence of a single non-competing RNA template (gene block), the three mixed primer sets from Orf1a, E-2, and N-2 genes will produce a single positive result on the LFIA corresponding to their appropriate tag (Digoxigenin, Texas Red, or Fluorescein). The weaker signal for E2 is attributed to natural variation in antibody efficacy but is still clearly visible. The no template control showed no result at any test line. Accumulation of streptavidin AuNPs at the control line was observed in all cases. Results are depicted in Figure 1.4.

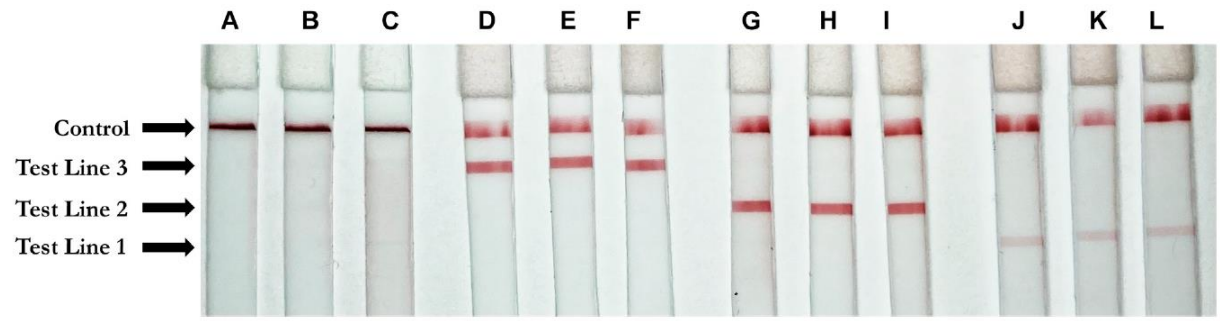


Figure 1.4 Positive test results for three unique gene blocks (subsections of SARS-CoV-2 viral genome). Test Line 1 (Texas Red Antibody, 1 mg/ml, Cat. # A-6399, ThermoFisher Scientific, Waltham, MA, USA); Test line 2 (Fluorescein antibody, 1 mg/ml, Cat. # ab19491, Abcam, Cambridge, UK); Test Line 3 (Digoxigenin antibody, 2.5 mg/ml, Cat. # 3210-0488, Bio-Rad, Hercules, CA, USA); Control line (biotinylated bovine serum albumin, 3 mg/ml, Cat. #B-2007-10, Vector Labs, Burlingame, CA, USA). **(A - C)** Negative control. **(D – F)** Orf1a gene block (1 ng/µL). **(G – I)** N gene block (1 ng/µL). **(J – L)** E gene block (1 ng/µL).

### 2.3 Sensitivity of Colorimetric RT-LAMP and LFIA

To test the sensitivity of the colorimetric RT-LAMP reaction of the SARS-CoV-2 RNA template, N-2, E-2, and ORF1a-1 primer sets were added individually and together in colorimetric RT-LAMP master mix solutions with 3, 5, 10, 25, 50, 100, and 1000 RNA copies per well (Figure1.5). All conditions were tested in triplicate. All positive samples turned yellow within 30 mins, while negative samples remained red. The results were quantified using red/grayscale values measured by ImageJ. Positive samples amplified by primer sets alone or together were distributed between 0.9 to 0.96. For negative samples, these values were around 1. For RT-LAMP products amplified by one set of primers, 3 µL of each amplification product was run on the LFIA. As expected, only one positive line relative to the appropriate amplified gene was observed on each strip for all positive samples.

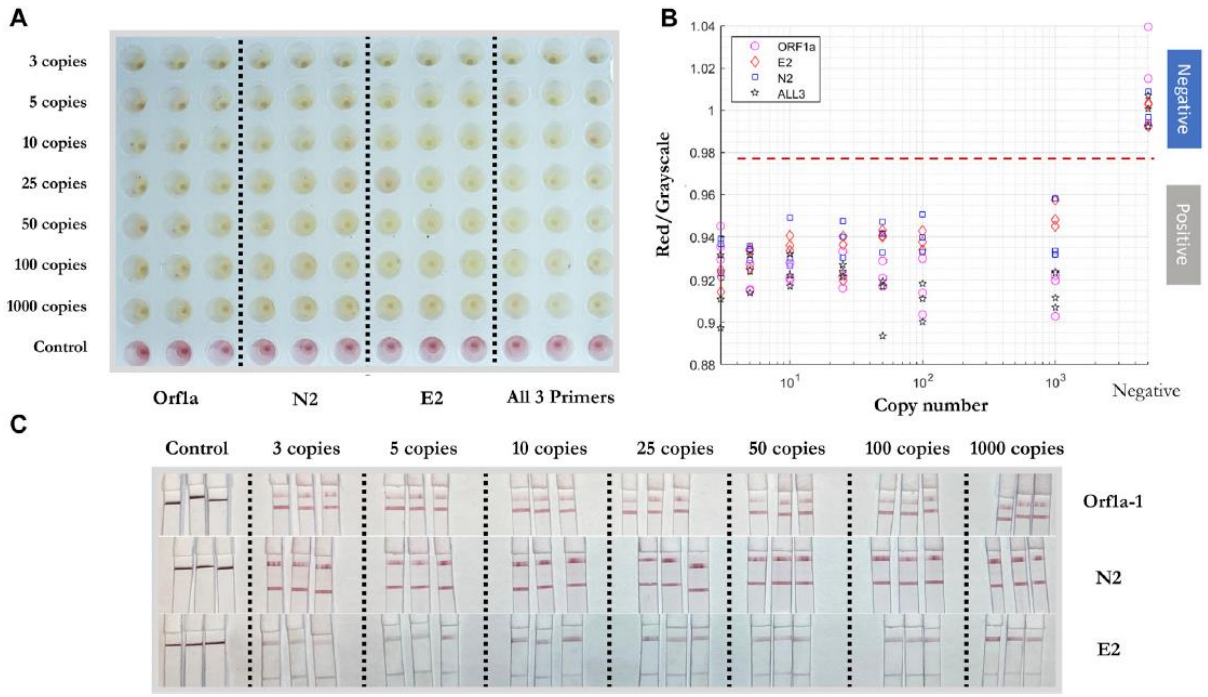


Figure 1.5 Sensitivity test of colorimetric RT-LAMP reaction and LFIA of artificial SARS-CoV-2 RNA template. **A)** Positive/ negative RT-LAMP products with ORF1a-1, N-2, E-2, and all three primer sets after the reaction, taken by overview camera. **B)** Red/grayscale value vs RNA copy numbers of both positive and negative samples. **C)** LFIA read-outs for RT-LAMP products amplified for ORF1ab, N, and E gene blocks.

To test the reproducibility of the RT-LAMP-LFIA prototype system at the lower limit of detection, all three primers were added into the RT-LAMP master mix with 3 copies of SARS-CoV-2 RNA template for twenty replicates, with triplicates of negative controls. The experiment was carried out at 65℃ for 30 min. A red to yellow color change was observed by the prototype camera from above. The red/grayscale values measured by ImageJ distributed below 0.98 for positive samples, while the values for negative control samples were around 1 (Figure 1.6).

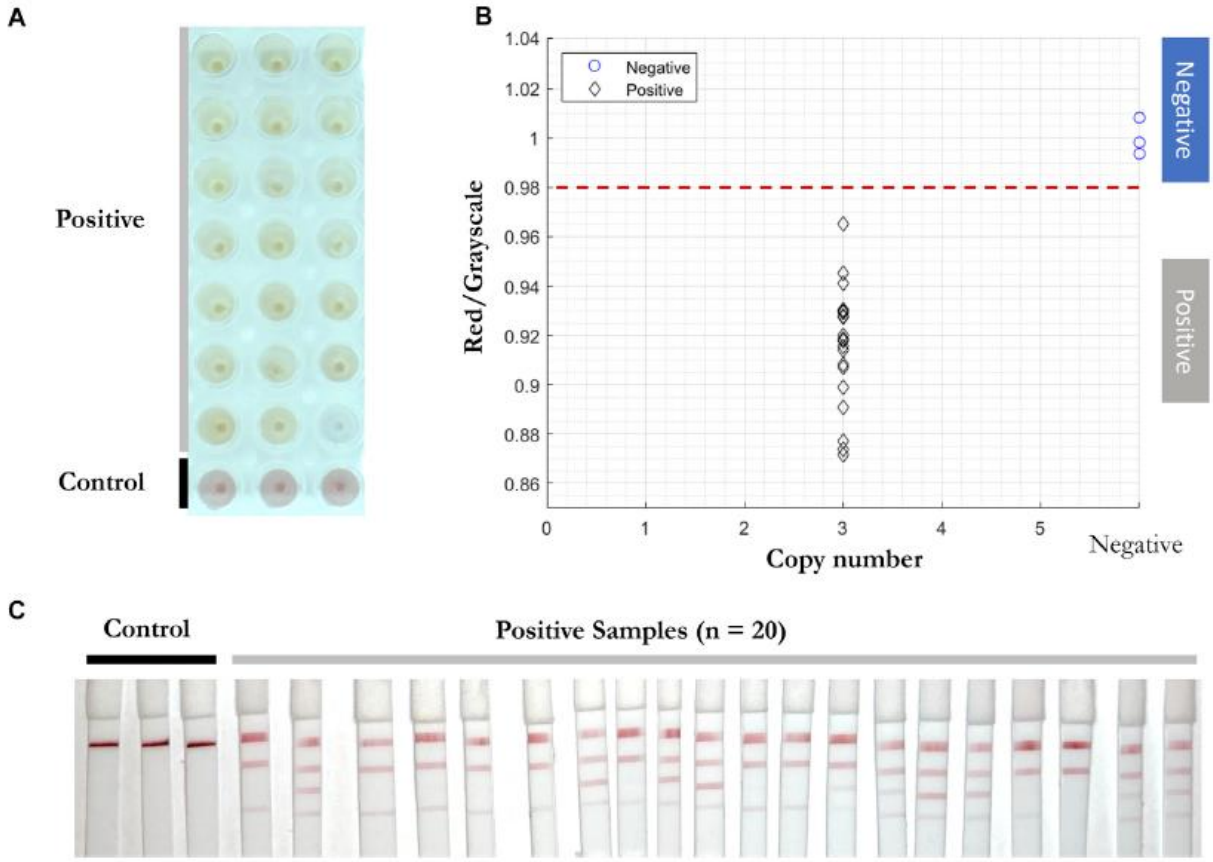


Figure 1.6 Reproducibility test of RT-LAMP-LFIA prototype system at the lower limit of detection. **A)** RT-LAMP products from 3 initial template copies (n=20) and negative control samples (n=3) after the reaction, taken by overview camera. **B)** Red/grayscale vs copy numbers of both positive and negative samples. **C)** LFIA read-outs for RT-LAMP products amplified for all three genes.

As expected, 5 to 10 minutes after adding the RT-LAMP products and running buffer onto each conjugate pad of the LFIA, different positive readings were shown. In the presence of a single RNA target and three sets of primers, competition for a limited amount of template strands means that some reactions can overtake others. As a self-limiting reaction, the process stops when a certain amount of products form or the reaction reaches certain (acid) pH values. Therefore, the amount of N-2, E-2, and ORF1a-1 primer sets' amplified products can vary and show different positive read-outs on the LFIA (Figure 1.6C).

## 2.4 Validation of RT-LAMP and LFIA for Inactivated Whole Viral Particles

RT-qPCR (Ioanna Smyrlaki et al. 2020) (Soon Keong Wee, Suppiah Paramalingam, and Eric Peng Huant Yap 2020) and RT-LAMP assays (Laura E Lamb et al. 2020) (Brian A Rabe and Constance Cepko 2020) are compatible with direct testing of nasopharyngeal and oropharyngeal swab specimens without an RNA purification or extraction step. To test the efficiency of RT-LAMP and LFIA, inactivated viral particles (ATCC, VR-1986HK) diluted into 3, 5, 10, 25, 50, 100, and 1000 copies were added in the RT-LAMP master mix with the three gene primer sets (Figure 1.7). After 30 mins at 65 ℃, a red to yellow color change was captured in wells with the inactivated viral particles by the prototype system camera. The red/grayscale value as measured by ImageJ for positive samples was distributed at around 0.94, while all the negative samples had red/grayscale values above 0.98. Next, 3 µL of each amplification product was mixed with 40 µL of running buffer before being deposited on the conjugate pad of a LFIA strip. Positive read-outs were mainly observed for ORF1a-1 gene amplified products (Figure 1.7C) because of primers competing during the self-limiting RT-LAMP reaction.

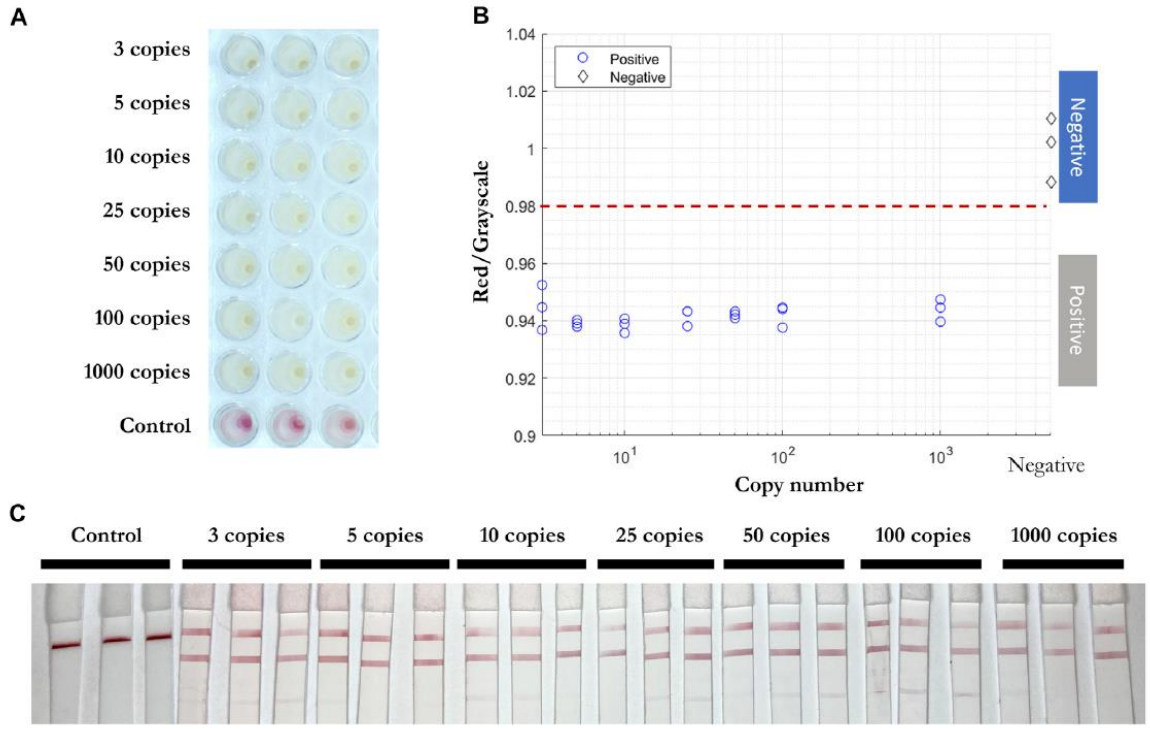


Figure 1.7 Direct RT-LAMP-LFIA testing of inactivated viral particles without prior RNA purification or extraction. **A)** RT-LAMP products for inactivated viral particles (3, 5, 10, 25, 50, 100, and 1000 copies) and negative control samples with three sets of primers, taken by overview camera. **B)** Red/grayscale vs copy numbers of both positive and negative samples. **C)** LFIA read-outs for RT-LAMP products amplified for all three genes.

Next, inactivated viral particles were spiked into unique negative patient swab samples preserved in iSwab Microbiome-EL (Extraction-Less) buffer to mimic patient-to-patient variation of conditions in amounts of 3, 5, 10, 25, 50, 100, and 1000 copies per reaction. All samples were red prior to the RT-LAMP reaction, and positive samples were yellow after 30 minutes at 65 ℃. The red/grayscale values of positive samples were consistently below 0.96, while the negative samples were distributed around 1 (Figure 1.8). Due to primers competing during the self-limiting RT-LAMP reaction, positive read-outs on the LFIA were mainly observed for ORF1a-1 gene amplified products (Figure 1.8C).

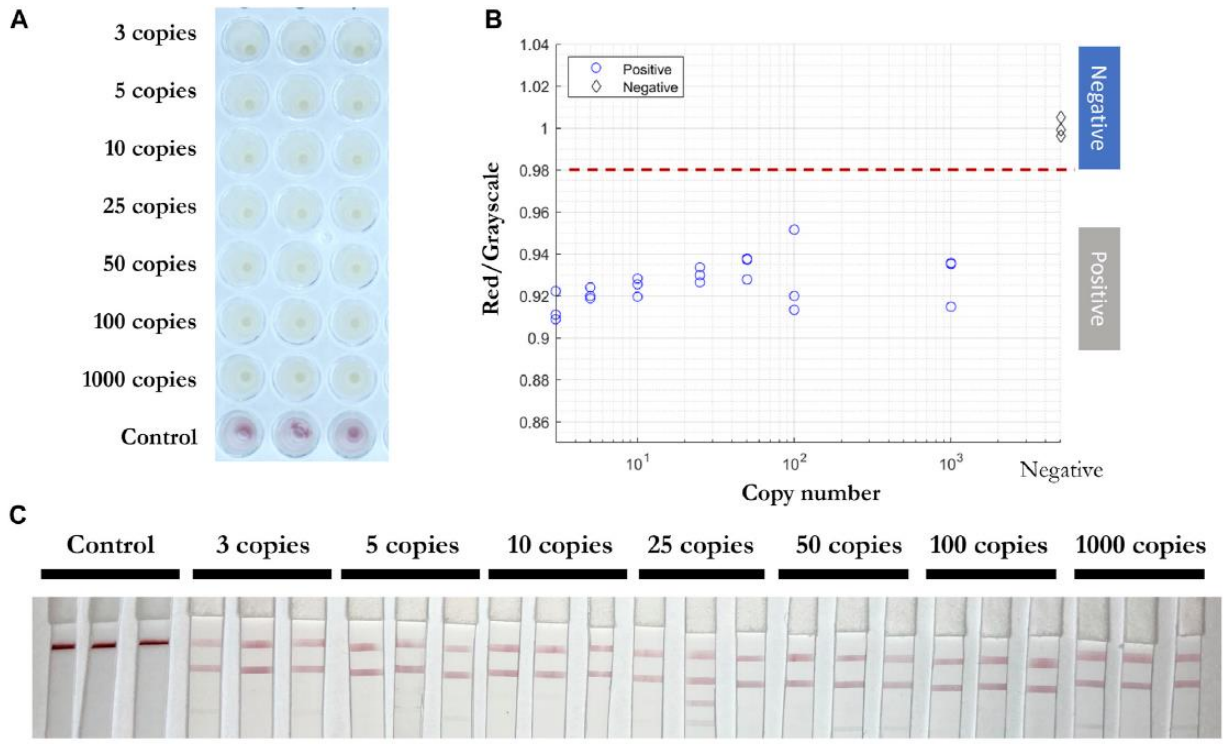


Figure 1.8 Direct RT-LAMP-LFIA testing of spiked inactivated viral particles in nasopharyngeal swab specimens without prior RNA purification or extraction. **A)** RT-LAMP products for inactivated viral particles spiked in nasopharyngeal swab specimens (3, 5, 10, 25, 50, 100, and 1000 copies) and negative control samples with three sets of primers, taken by overview camera. **B)** Red/grayscale vs copy numbers of both positive and negative samples. **C)** LFIA read-outs for RT-LAMP products amplified for all three genes.

## 2.5 Validation of RT-LAMP and LFIA for Clinical Samples

2 µL of solution from 30 positive and 30 negative clinical samples (Table 1.5) were added into RT-LAMP master mix with all three primer sets present. The positive samples turned yellow within 30 mins at 65 ℃ and had red/grayscale values between 0.9 and 0.94. The negative samples remained red with red/grayscale values above 0.98 as quantified by ImageJ (Figure 1.9). For positive samples, read-outs were observed for all samples on at least one test line on the LFIA (Figure 1.9C).

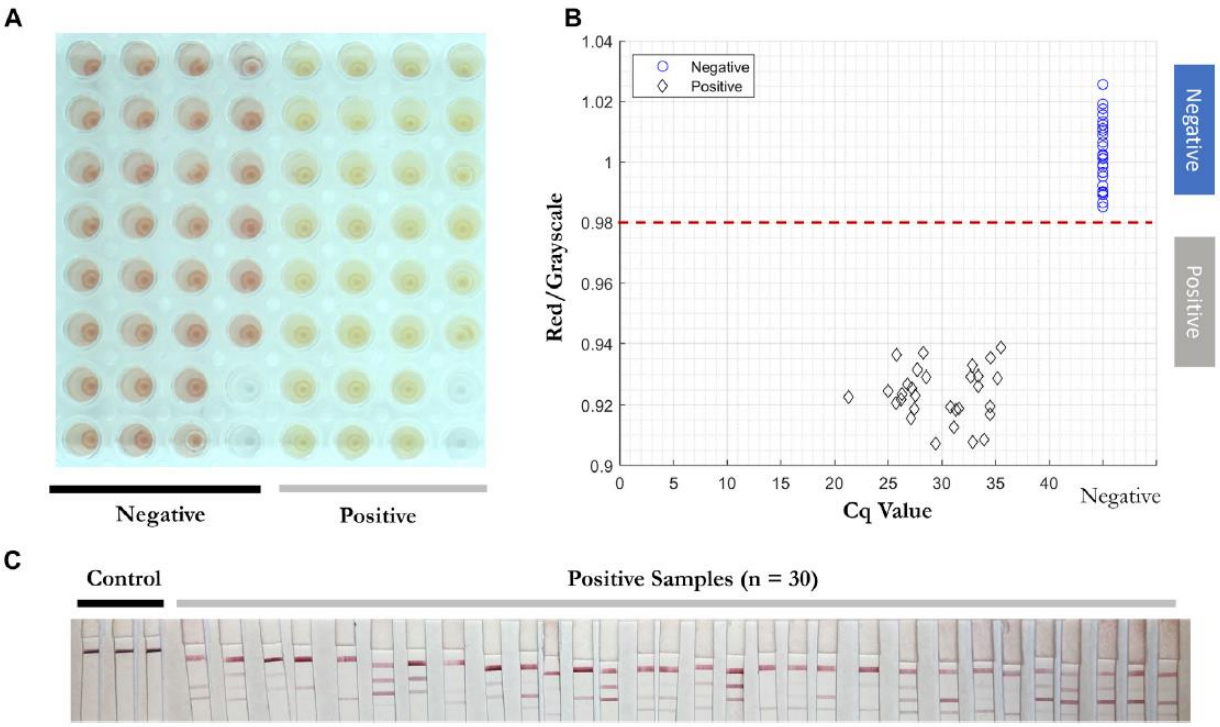


Figure 1.9 Direct RT-LAMP-LFIA testing of 30 positive and 30 negative clinical nasopharyngeal swab specimens without a prior RNA purification or extraction. **A)** RT-LAMP products for 30 positive and 30 negative clinical samples amplified with three sets of primers, taken by overview camera. **B)** Red/grayscale vs copy numbers of both positive and negative samples. **C)** LFIA read-outs for RT-LAMP products amplified for all three genes.

## 3 Discussion

In this chapter, we presented a semi-automated RT-LAMP-LFIA prototype system and evaluated its capability to test nasopharyngeal swab samples from patients without a prior RNA purification or extraction step. The system is almost fully automated and does not require trained personnel or specialized laboratory equipment such as thermocyclers. The simple design and automated sample-to-answer workflow indicate that our system is suitable for implementation in high-traffic community settings such as airports or event centers for rapid and easy to use point-of-care diagnostics.

We tested RT-LAMP primer sets for N, E, and ORF1ab genes of the SARS-CoV-2 virus and validated their results on the LFIA. Multiplexing of colorimetric RT-LAMP reactions in a single pot for the SARS-CoV-2 gene targets accelerated the reaction to yield results within 15 minutes. Moreover, the multiplexed read-out of up to 3 genes on a single LFIA can further distinguish multiple viral public health threats on the same platform - for example, SARS-CoV-2, Ebola, and yellow fever.

The main advantages of the RT-LAMP-LFIA method – its simplicity, low cost, high sensitivity, and high specificity – make it ideal for use as a high-throughput diagnostic device in non-laboratory settings. To apply the method and system to detect multiple viruses or their variants, one can extend the primer set and divide the sample into a few LAMP reaction pots, each containing a chosen set of gene targets for specific organisms. Thus, the overall technique and system reported here are scalable to protect the public from future outbreaks and epidemic.

**Acknowledgements**

Chapter 1, in full, is a reprint of the material as it appears in L Waller, Z Guo, R Tang, Z Zhang, E Wang, J Yasuhara-Bell, L Laurent, and YH Lo, “High Sensitivity, Rapid Detection of Virus in High Traffic Environments,” Frontiers in Bioengineering and Biotechnology 10, 2022. The dissertation author was the primary investigator and author of this paper.

CHAPTER 2

## 1. Results and Discussion

### 1.1 Theoretical basis for evaporative enrichment

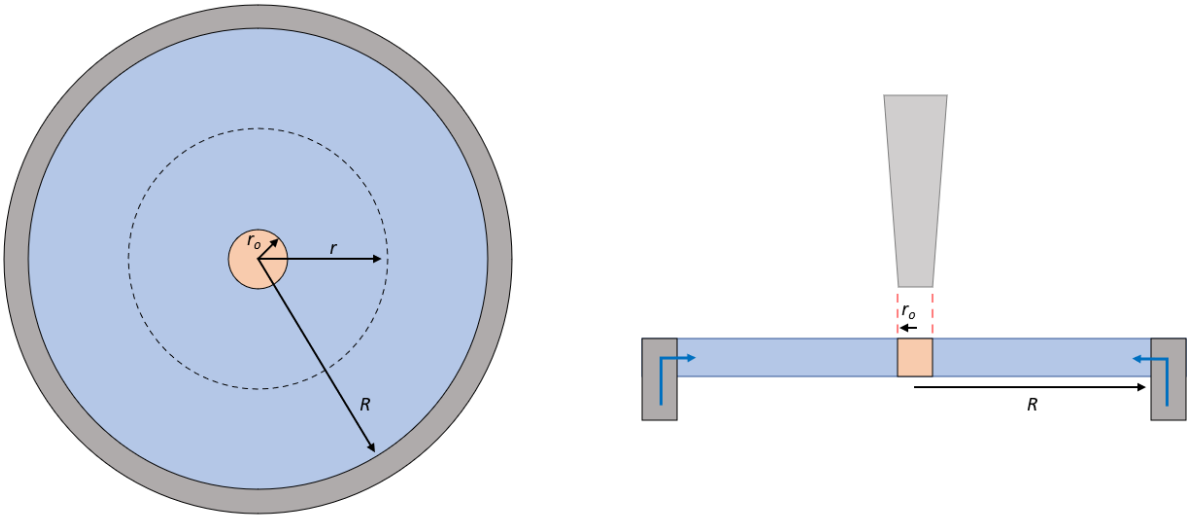


Figure 2.1 Schematic for the inward, radial replenishment of fluid and evaporation by ambient and airflow induced methods.

We define a system where a circular slice of porous media makes peripheral contact with an unlimited reservoir of fluid. At the perimeter of the porous slice, the capillary force induces the inward, radial penetration of liquid towards its center. At the center, a nozzle is positioned above the porous slice and generates a flow of air that is constrained within the nozzle radius. To model the system as a two-dimensional problem using planar coordinates, we assume that the thickness of the slice is much smaller than the radial dimensions.

During the enrichment process, two methods of evaporation occur on the wet surface of the porous slice. The first is the ambient evaporation that is not affected by airflow, and the

second is the airflow-induced evaporation. We therefore consider the total evaporation rate, K, which is the volume of evaporated liquid per area and time ($cm^3/m^2 \cdot s$) and is the sum of the ambient evaporation ($K_o$) and the airflow-induced evaporation ($K_1$):

$$K(r) = K_o + K_1 u(r_o - r) \qquad (1)$$

Where $r_o$ is the radius of the airflow jet and *u* represents a unit step function when traveling away from $r_o$. Here, we assume that all evaporation will only occur on the top surface of the filter and that the airflow speed above the filter surface is negligible outside $r_o$.

When the steady state is reached and the enriched area under the nozzle has not completely dried, the definition of the derivative yields the following:

$$2\pi r K(r) dr = F(r - dr) - F(r)$$

$$2\pi r K(r) = -\frac{dF(r)}{dr} \quad (2)$$

Where *F* refers to the volumetric flux of water per time ($cm^3/s$)

In order to drive the flux, Darcy's law for liquid flow can be expressed as:

$$\frac{F}{A} = -\frac{S}{\eta}\frac{dP}{dr} \quad (3)$$

Where the flux, *F*, of liquid flow is through a cylindrical surface having area $A = 2\pi rh$, S is the permeability of the porous medium, η is the liquid viscosity, and P is the pressure of the liquid. Substituting the cylindrical area into equation 3 and solving for the volumetric flux yields,

$$F = -\frac{2\pi h \gamma S}{\eta} r \frac{dP}{dr} \quad (4)$$

Substituting eq (4) into eq (2) and combining with eq (1),

$$2\pi r[K_o + K_1 u(r_o - r)] = \frac{2\pi h\gamma S}{\eta}\left[r\frac{d^2P}{dr^2} + \frac{dP}{dr}\right]$$

$$[K_o + K_1 u(r_o - r)] = \frac{h\gamma S}{\eta}\left[\frac{d^2P}{dr^2} + \frac{1}{r}\frac{dP}{dr}\right] \qquad (5)$$

We define the boundary conditions as:

$$P(R) = P_c, \ \ \frac{dP}{dr}|_{r=0} = 0 \ \ (see\ Supplmentary\ for\ this\ BC)$$

$$P(r) = \frac{-\eta}{4h\gamma S}(K_o)(R^2 - r_o^2) - \frac{\eta}{4h\gamma S}(K_o + K_1)(r_o^2 - r^2) + P_c \qquad 0 \leq r \leq r_o$$

$$P(r) = \frac{-\eta}{4h\gamma S}(K_o)(R^2 - r^2) + P_c \qquad R \geq r \geq r_o \qquad (6)$$

$$P(r) \geq 0.\ for\ all\ r. \quad When\ P(r) = 0\ at\ a\ certain\ r, the\ region\ is\ dried\ up.$$

$$F(r_o) = -\frac{2\pi h\gamma S}{\eta} r\frac{dP}{dr}|_{r_o} = \pi {r_0}^2(K_o + K_1) \qquad (7)$$

We assume that when the wetted porous slice undergoes evaporation, it experiences varying degrees of water saturation. We therefore use the relation:

$$P(r) = P_c n(r) \qquad 0 \leq n(r) \leq 1. \ (8)$$

where $P_c$ is the capillary pressure, and $n$ is the fraction of the pores (capillaries) that are completely saturated with water. The capillary pressure has the form:

$$P_c = \frac{2\sigma\ cos\theta_S}{R_{eff}} \qquad (9)$$

Where σ is the surface tension, $\theta_s$ is the contact angle formed between solid and liquid, and $R_{eff}$ is the effective pore radius of the porous medium.

Integrating to find the water volume within $r_o$:

$$V(r_o) = 2\pi h\gamma \int_0^{r_o} n(r) r dr = \pi h\gamma r_o^2 - \frac{\pi\eta r_o^2}{8P_c S}[K_o(2R^2 - r_o^2) + K_1 r_o^2] \quad (10)$$

Taking the ratio between the water flux and volume determines the enrichment factor, a value which characterizes how effectively solutes are transported and concentrated under the airflow spot:

$$EF\ (enrichment\ factor) = \frac{F(r_o)t}{V(r_o)} = \frac{(K_o + K_1)t}{h\gamma - \frac{\eta}{8P_c S}[K_o(2R^2 - r_o^2) - K_1 r_o^2]} \quad (11)$$

In the case where the airflow-induced evaporation rate is much greater than the ambient evaporation rate over the entire wetted area ($K_1 r_o^2 \gg K_o R^2$), then (11) becomes.

$$EF\ (enrichment\ factor) = \frac{F(r_o)t}{V(r_o)} \sim \frac{K_1}{h\gamma + \frac{\eta}{8P_c S} K_1 r_o^2} t \quad (12)$$

Therefore, to achieve a high enrichment within a given time period, the physical parameters of the porous slice and liquid should be considered. In addition, the parameters governed by the airflow ($K_1$, $r_o$) can also be controlled to further tune the enrichment factor. While $r_o$ is a simple geometric parameter, $K_1$ is influenced by a variety of factors including airflow speed, humidity, temperature etc. These factors were incorporated into $K_1$ to simplify the model, however present additional areas to modify when looking to further increase the enrichment factor.

### 1.2 Overview of airflow-based enrichment on paper

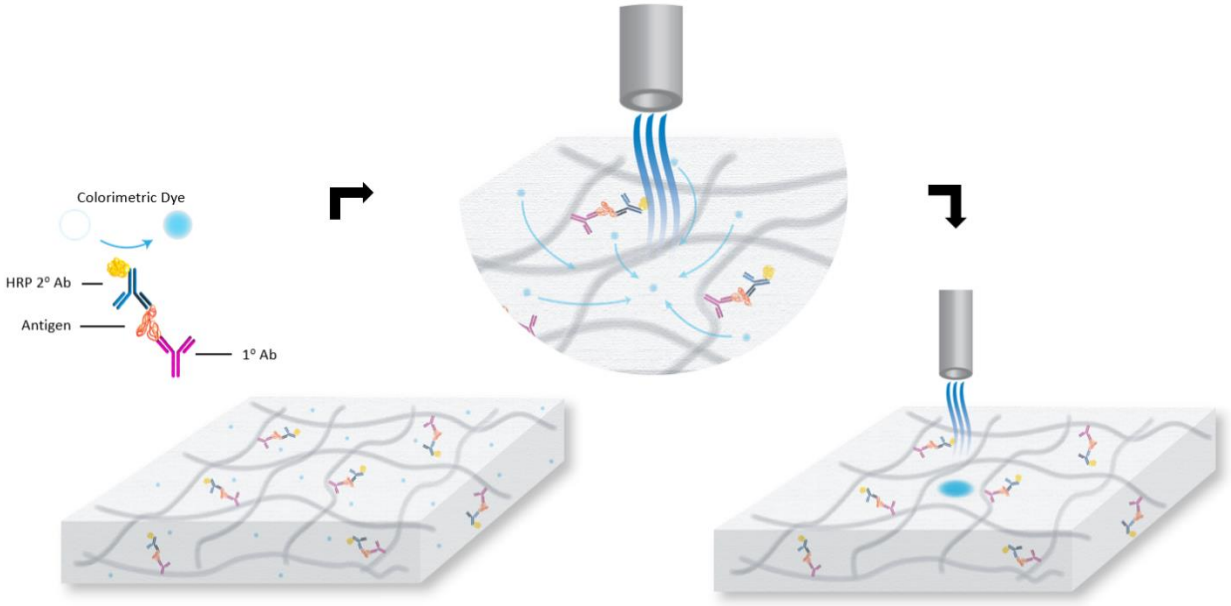


Figure 2.2 Schematic of the airflow-based enrichment for the concentration of colorimetric substrates produced during on-paper ELISA.

Figure 2.2 depicts the principle and setup for airflow-based enrichment in a paper matrix. This technique occurs on a pre-wetted filter that is suspended on a hollowed platform such that it is not contacting any surface underneath it. A nozzle connected to a nitrogen source is brought down perpendicular to the filter, and nitrogen is blown to create an evaporative gradient by reducing the thickness of a boundary layer containing saturated water vapor immediately above the surface. While any compressed air source can accomplish this, nitrogen was chosen as it is a "dry" (low humidity) source of airflow and gave consistent enrichment results when compared to compressed, ambient air. Due to displacement by the nitrogen airflow, the gradient is highest in the area immediately under the nozzle. Therefore, fluid flows driven by capillary action will converge towards this area from the filter's periphery to replenish the lost water. In doing so, any dissolved solutes will be carried by the flow and eventually accumulate underneath the nozzle.

We aim to use this technique to enhance the visibility and sensitivity of nucleic acid and protein colorimetric detection assays – including ELISA. For these assays, the colorimetric substance can be enriched to a single spot under the nozzle to improve the uniformity and concentration in addition to easier detection.

### 1.3 Static or dynamic movement of the airflow nozzle leads to solute enrichment and movement.

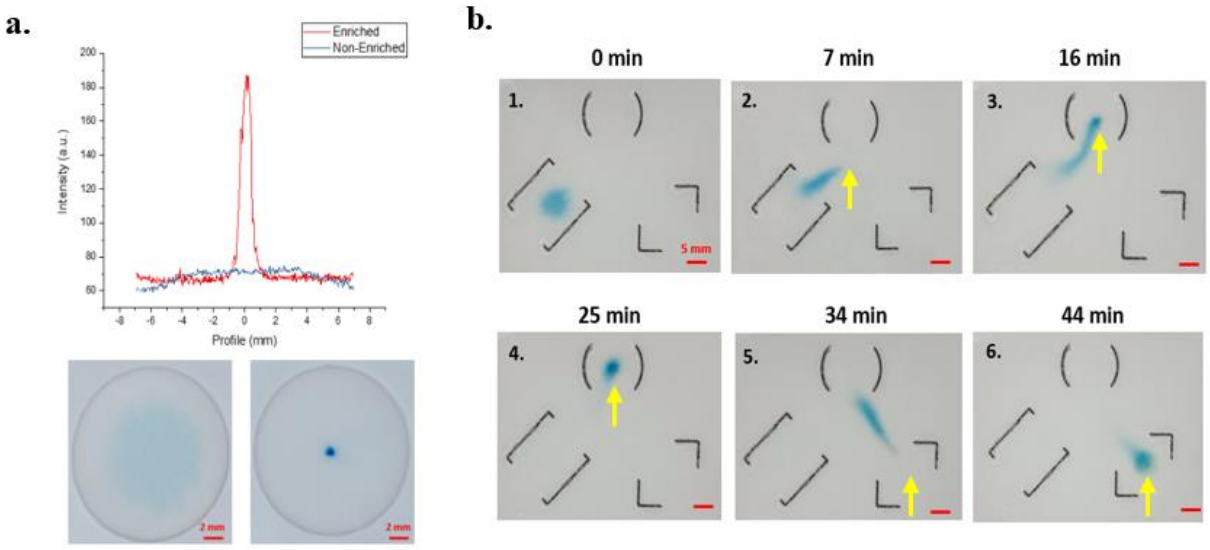


Figure 2.3 (a.) Profile plot of pixel intensity for enriched and non-enriched samples of dye deposited on paper. Images underneath represent corresponding non-enriched (before) and enriched (after) sample. (b.) Image sequence of dye localization in paper with hydrophobically patterned barriers indicated by black outlines. Images were taken during specified time points during dynamic movement of the nozzle. The actual nozzle position is indicated by the yellow arrow.

Airflow enrichment can accommodate two modes of fluid movement depending on whether the nozzle is in a static or dynamic position. When the nozzle position remains fixed (Figure 2.3a), solute enrichment occurs as evaporative-loss leads to capillary-induced replenishment from the surrounding area. To visualize this effect, 7 µL of a blue, diluted dye

solution was deposited on a 16mm diameter filter cutout. The cutout was placed concentric to a hollowed replenishing pad saturated with water, and a 200μm diameter nozzle was aimed perpendicular to the surface. Initiating the airflow establishes an evaporative gradient which generates fluid flows that are directed radially inward and transports the dye from a larger area to a defined spot. In addition to these flows along the 2D plane, any solutes will also move and localize at the paper's surface due to evaporation being a surface-driven phenomenon. As seen in the profile plot, this three-dimensional transport can thereby enhance visualization and detection of the initially diluted dye as it becomes more uniformly concentrated and unobscured from interacting with light.

Dynamic movement of the nozzle allows transportation of the solute to specified positions along the paper surface. The transport mechanism remains the same as the enrichment process, but the continual re-establishment of new evaporative gradients allows the direction of the replenishing flows to be controlled. In Figure 2.3b, 1μL of blue dye was deposited on a wetted filter paper with hydrophobic patterns. The patterned filter paper was placed concentric to a replenishing pad saturated with water to prevent the paper from drying out. As less emphasis is placed on the degree of enrichment and more on the speed of transport, a wider 1.5 cm diameter nozzle accompanied with higher airflow speeds was used in comparison to that of the static enrichment. As shown in Figure 2.3b, the localization of the dye can be controlled simply by changing the position of the nozzle above the paper surface.

### 1.4 Demonstration of sequential delivery using airflow-enrichment method

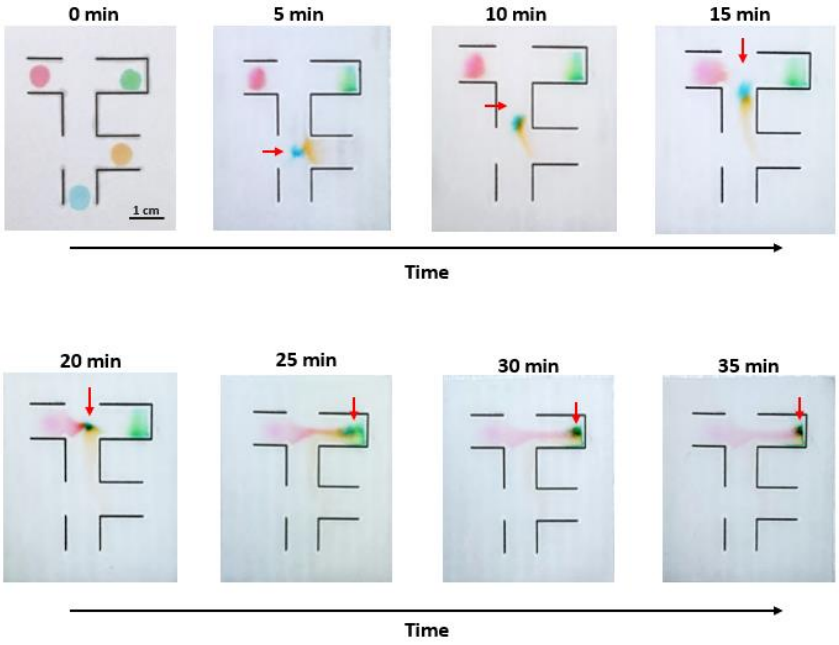


Figure 2.4 Image sequence for the sequential delivery of colored dyes by moving the airflow spot (red arrow) on a paper device patterned with PDMS channels. Black outlines represent the hydrophobic barriers and breaks in the outline indicate inlets to the channel design.

We demonstrate how controlled delivery of multiple reagents, visualized by different dye colors, can be accomplished using the airflow enrichment technique (Figure 2.4). On a piece of filter paper patterned with hydrophobic channels, a combination of static and dynamic nozzle movements serves to mix, and transport specified reagents, respectively. The filter paper is overlayed concentric to a hollow replenishing pad cutout, such that contact between the two materials was only made at the paper's perimeter. Then, 1uL of each dye color was spotted on the paper and could be mixed in a stepwise fashion based on the position of the nozzle - indicated by the red arrow. For this setup, water is transferred from the replenishing pad to the filter paper and eventually moves towards the interior of the channel through the openings in the design. While the openings act as inlets, the movement of the nozzle governs the position of the

outlet and determines where fluid flows will converge. As there is only one nozzle (outlet) in this system, additional openings were incorporated to reduce backflow and prevent early mixing of downstream reagents. For sections where the dye was to remain stationary throughout the process, such as the green dye, a closed channel was created by walling off three sides to create an area of dead volume.

The advantage of airflow-enrichment lies in the mechanism responsible for fluid control. For many designs focused on sequential delivery, the primary driving force for fluid transport is through capillary action. While capillarity is still present during airflow enrichment, it plays a secondary role with evaporation being the main driver of fluid movement. This has considerable effects when determining the overall design and costs of the assay. For one, conventional assays that rely on capillarity require relatively large sample volumes as they must continually imbue the device with the sample to reach the detection zone. For evaporative-driven transport, delivery of a small, initial volume of sample can be dragged to downstream detection zones simply by guiding it with the nozzle. In this case, the nozzle was able to transport 1μL of the initial blue dye from beginning to end. In addition, for assays that require interactions between molecules to occur, the airflow technique allows for more efficient mixing. Rather than relying on the slower process of diffusion, the nozzle can be left in a static position such as in the 20- and 35-minute time points (Figure 2.4) to facilitate the enrichment of different molecules and promote binding events. Finally, in designs that transport fluid through capillary action, the fluid flow is always "on", and specific obstructions are implemented in order to slow and control the flow rate for sequential delivery. For evaporative driven transport, the fluid flow can be turned "on" and "off" depending on whether any air is being blown on the paper surface. The lack of any obstructions

keeps the fabrication process simple and reduces the amount of space needed to accommodate the obstruction itself.

### 1.5 Improving visualization on paper for colorimetric RT-LAMP

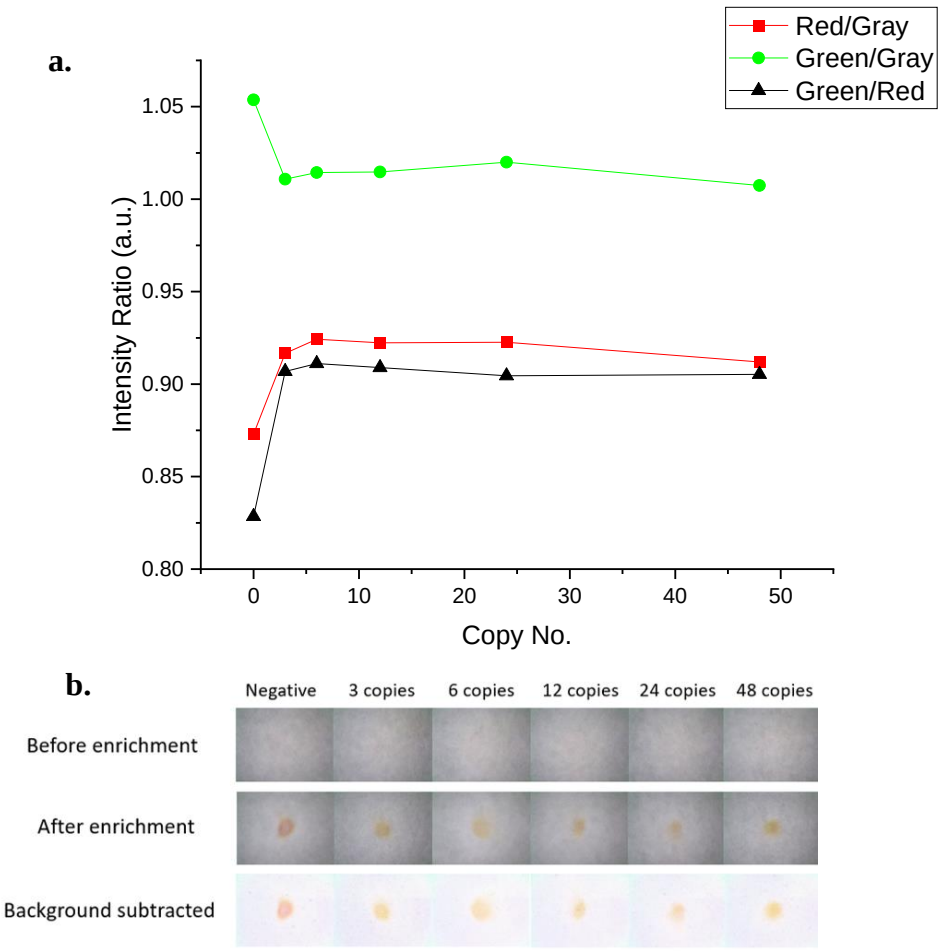


Figure 2.5 (a.) Plot of intensity ratio v. copy number between red and grayscale, green and grayscale, and green and red pixels. (b.) Before and after enrichment photos corresponding to different initial RNA copy numbers of the COVID-19 genome. Includes bottom "background subtracted" row to better visualize the color of each spot.

To test whether the airflow enrichment could improve visualization in already established colorimetric assays, the technique was incorporated on paper RT-LAMP in the detection of the COVID-19 genome (Figure 2.5). Heat inactivated viral particles were spiked in nuclease-free water to the desired concentrations and then amplified using a commercially available RT-

LAMP kit. For all copy numbers, amplification via LAMP was performed in test tubes for 60 minutes prior to depositing 3μL of the LAMP product onto paper strips. The strips were connected to a replenishing flow of nuclease-free water, and the airflow was turned on for 5 minutes before imaging. As shown in Fig.2.5b, comparison between the “before” and “after” enrichment demonstrates how the process drastically improves the visibility of the dye. Furthermore, the enrichment did not alter the results of the test. The pH-sensitive color of the RT-LAMP result, either red (negative) or yellow (positive), is influenced by polymerase activity which releases a proton per each incorporated nucleotide. As the enrichment involves the concentration of molecules, we may expect false positives to occur due to co-enrichment of hydronium ions. However, a large shift in the green/red pixel intensity ratio from 0 (negative control) to 3 RNA copies supports the validity of the results as the negative control remains red.

Due to the presence of buffer in the master mix solution, the final enrichment spot remains larger than previously demonstrated in Figure 2.3a as early salt crystallization inhibits further condensation. While additives can be considered to reduce salt build up, we chose not to include any as it may affect the pH of the solution and therefore the accuracy of the test. Even with a larger spot size however, the results of the tests were still clear to the naked eye. The ease of integrating the airflow-based enrichment to various colorimetric assays, coupled with its short process time, demonstrates the flexibility and simplicity of the technique.

## 1.6 Improving on-paper ELISA sensitivity.

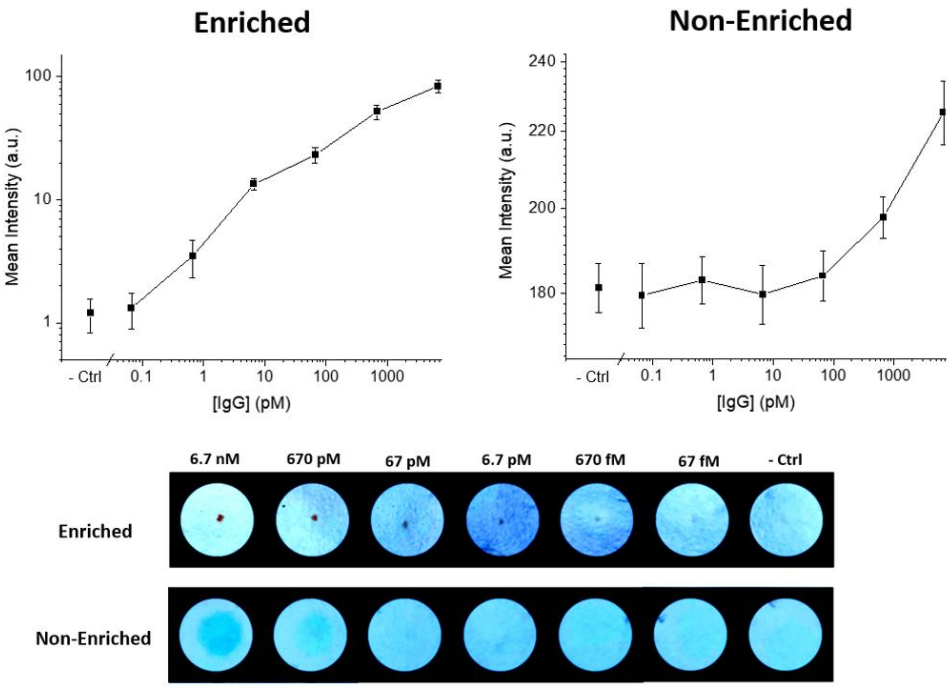


Figure 2.6 (a.) Comparison of Non-enriched and Enriched intensity plots for IgG concentrations from 67fM to 6.7nM. Error bars were calculated from three sets of experiments. (b.) Respective images from enriched and non-enriched samples from a single experimental set. Brightness and contrast were adjusted for better visualization of the TMB product.

We next use ELISA to model our enrichment method in improving the sensitivity for protein detection assays (Figure 2.6). While ELISA on paper has attracted multiple studies in the past, a key obstacle in detection is due to the non-uniformity and unequal distribution of the colored substrate. For this assay, TMB was chosen as the colorimetric substate as it has been shown to elicit one of the most sensitive responses in comparison with others. However, a drawback of using TMB lies in the relative insolubility of the oxidized product in water which is detrimental in the formation of an airflow-enriched spot. Therefore, the addition of the 0.1% glycerol (v/v) in 2M HCl “stop” solution served multiple purposes. The first was to prevent further development of the substrate during enrichment and keep the colorimetric development times consistent between the enriched and non-enriched samples. The second was to protonate

the TMB product to increase its solubility for enrichment. Glycerol was also added in small amounts to prevent early salt crystallization which halts spot formation during the evaporative process. The addition of an acidic solution to the TMB product causes a color change from blue to yellow which explains the different colors between the enriched and non-enriched samples. Despite the color change, the enriched samples were able to distinguish antigen concentrations by up to 2 orders of magnitude as compared to the non-enriched samples while only spending 15 minutes under airflow. This demonstrates the ease at which airflow enrichment can be integrated in current detection-based assays given the fraction of time needed to conduct the process and the much-improved detection sensitivity.

## 2. Materials and Methods

### 2.1 Colorimetric Assay Reagents

For the RT-LAMP assay, WarmStart Colorimetric RT-LAMP 2X Master Mix (DNA and RNA) were purchased New England Biolabs. The RT-LAMP primers against Nucleocapsid (N-1) and ORFla-1 genes were synthesized by Integrated DNA Technologies (IDT) and were designed according to a similar assay.The SARS-CoV-2 RNA (VR-3280SD) was purchased from American Type Culture Collection (ATCC) with an initial copy number of $3.4x10^5$ genome copies/ µL. For ELISA, Rabbit IgG, goat anti-rabbit IgG, TMB, Ultrapure water, 25% glutaraldehyde and chitosan were purchased from Millipore Sigma. Anti-rabbit IgG antibody conjugated with HRP was purchased from VectorLabs. The blocking buffer comprised of 0.05% v/v Tween-20 and 1% w/v bovine serum albumin (BSA) in 1X phosphate-buffered saline (PBS).

The antibody incubation solution consisted of the blocking buffer with the conjugated antibody at a 1:4000 ratio.

### 2.2 Enrichment Setup

Pre-pulled, 1mm O.D. capillaries were purchased from Tritech Research, and they were tips sanded down to roughly 20 μm in diameter. A single tip was mounted on an xyz-stage through a 3D-printed holder and connected to a nitrogen source by rubber tubing. The mass flow rate was adjusted by pressure valves incorporated along the rubber tubing and specific values were determined by a mass flow meter purchased from Sierra Instruments. The specified sample was deposited on a cutout of Watman No. 1 filter paper and placed on a hollowed-out replenishing pad comprised of blotting paper saturated with water. The contact between the filter cutout and the replenishing pad only occurred at the perimeter of the filter cutout. This arrangement was then placed on a 3D-printed platform that also contained a hollow section and the capillary tip was brought about 2mm above the filter piece.

### 2.3 Enrichment of dye

The filter paper was punched into circular, 16 mm diameter cutouts and initially wetted with 10uL of DI water. After allowing the water to spread, 3uL of a diluted food dye solution was added to the center of the cutout which was then overlayed on top of a hollowed-replenishing pad saturated with DI water. The section was placed under the capillary tip and the nitrogen flow was turned on to a rate of 0.1 l/min. Airflow enrichment occurred for 15 minutes before imaging the section under a desktop ring-light using an iPhone 10 camera.

### 2.4 Fluid control

Patterns and outlines were designed using CAD software and printed directly on filter paper. The outlines were then traced overusing a syringe containing a 10:1 ratio of PDMS to curing agent and subsequently placed in a 60$^{o}$C oven to cure for 1 hour. Prior to enrichment, the patterned filter paper was dampened with DI water and 1µ of dye was spotted in the starting positions. The patterned filter paper was then placed on a water-saturated replenishing pad and positioned 2mm under a 1.5 cm diameter metal nozzle with a nitrogen flow of 0.25 l/min. The relative position of the nozzle was changed by moving the platform with the filter paper.

**2.5 Enrichment of RT-LAMP products on paper**

Colorimetric LAMP was performed by adding 1 µL of the specified copy number of isolated SARS-CoV-2 RNA, 12.5 µL of the WarmStart Colorimetric RT-LAMP 2x Master Mix, 2.5 µL of the 10x primer mix and diluting with nuclease free water up to 25µL in total volume. All the solutions were prepared fresh and kept in closed test tubes to limit exposure to atmospheric $CO_2$. The reactions were then incubated in a 65 °C oven for 60 min. The RT-LAMP samples were then taken out and placed on ice for 30 seconds before being stored at room temperature. For the enrichment, filter paper was cut into strips and 3µL each RT-LAMP product was deposited in the middle. Enrichment was carried out for 5 minutes with at 5µL/min replenishing flow of nuclease-free water from syringe pumps purchased from Harvard Apparatus. Before and after images were taken by a digital microscopic camera (AM7115MZT, Dino-Lite) with preset image capture settings.

**2.6 RT-LAMP colorimetric readout signal analysis**

The effect of the GAMMA correction on the captured image is eliminated on the original image to remove the biased on the pixel intensity introduced by GAMMA correction. The

original image is subtracted by the background level first to remove the noise introduced from the background. A binary mask is generated through fixed intensity thresholding and preset enrichment spot size to determine the region of interest (ROI). The processed image is then convoluted with the binary mask to exclude pixels outside of the ROI. The convoluted color image is split into single color channels, and the average pixel intensity is calculated based on the average pixel intensity of the RGB color channel images. The image processing pipeline is developed based on ImageJ and MATLAB. All enrichment sample paper is processed using the same pipeline and parameter setting.

### 2.7 On-Paper ELISA

Double-sided tape was placed on a 3D-printed plate containing a 3 x 3 array of 12mm diameter holes. The tape was cut out around the holes and 16mm diameter filter circles were overlayed on top with only the perimeter making contact. Enhanced antibody immobilization was performed by adding 20μL of 0.25mg/mg chitosan (in 1% acetic acid) to all filter circles and letting them dry completely. After, 20μL of 2.5% glutaraldehyde in 1X PBS was added to the circles and the plate was covered with a petri dish for 1 hour to avoid evaporation. Each circle was then washed four times with 20μL of PBS with the excess liquid being removed between washes by pressing the plate against blotting paper. After washing, 10uL of the capture antibody solution was deposited and allowed to incubate for 30 minutes. The circles were washed four times with 20μL of PBS and successively blocked with 30uL of blocking buffer for an additional 30 minutes. After blocking, the circles were washed once with 20μL of PBS and 3μL of the Rabbit IgG at specified concentrations was added to each circle. This was incubated for 15 minutes before adding 7μL of the secondary antibody solution and incubating for another 2 minutes. The circles were then removed from the plate and put into a wash bath containing

0.05% Tween in 1X PBS and a separator to prevent individual circles from contacting each other. The wash bath was placed on a shaker for 30 minutes with the wash solution being changed out every 10 minutes. The circles were then stored in 1X PBS until use.

### 2.8 Comparison between Enriched and Non-enriched Samples

For the non-enriched sample, the circles were removed from the PBS and transferred on blotting paper to remove excess liquid prior to being placed on a cleaned plate. The color development was initiated by adding 7μL of TMB solution and allowing 80 seconds for the reaction to proceed before imaging under a desktop ring light. A similar procedure was performed with the enriched samples except that the reaction time was shortened 70 seconds to include a washing step afterwards. This step consisted of transferring the circle onto blotting paper and depositing 1mL of ultrapure water to reduce salt levels. Then, 6μL of 0.1% glycerol (v/v) in 2M HCl was added to the circle to stop the reaction during the enrichment process. The circle was enriched under the 200μm diameter capillary nozzle for 15 minutes until completely dry and imaged under the ring light.

### 2.9 ELISA Imaging

The images were processed through ImageJ by first subtracting the background by 50 pixels, then enhancing the contrast by 0.3%. The images were then split into RGB color channels and inverted. For the non-enriched samples, the selected ROI consisted of the entire filter circle diameter. In the enriched samples, a binary mask was used to highlight the enriched area and the ROI consisted of a 2mm diameter section around the highlight. After finding the mean respective mean intensities from each channel, the magnitude of the combined channels was calculated for the mean intensity.

## 3. Conclusion

To summarize, we present a simple, airflow-based method that can manipulate fluid flows in paper matrices. Depending on how the method is used, enrichment or lateral transportation of solutes can be performed using minimal external equipment. The enrichment process was integrated into existing colorimetric assays for genomic and proteomic detection to significantly enhance the visualization and sensitivity of the assays. While the enrichment aspect was explored in depth for this study, we also demonstrate how multistep, sequential delivery of reagents can be accomplished for future assays requiring higher complexity. This method ultimately presents a unique example where sensitivity improvement and fluid control can be accomplished using a single technique. Despite focusing on colorimetric detection assays in this study, we envision that this method can be easily incorporated into the broader field of mPADs.

## Acknowledgements

Chapter 2, in full, is a revise of the material as it appears in E. Wang, Z. Guo, T. Rui and YH. Lo, “Using Airflow-Driven, Evaporative Gradients to Improve Sensitivity and Fluid Control in Colorimetric Paper-Based Assays,” Lab on a Chip 21, 4249-4261. The dissertation author was the co-author of this paper.

CHAPTER 3

# 1 Materials and Methods

## 1.1 Fabrication of etched microfluidics silicon molds and PDMS device

The inaugural microfluidics device design was executed through a meticulously orchestrated sequence of procedures, commencing with the photolithography of NR-9 photoresist followed by a subsequent dry etching process. The schematic representation of the devised pattern was designed by AutoCAD and is meticulously depicted in Figure 3.1. For this endeavor, a silicon wafer measuring four inches in diameter underwent a preliminary pre-cleaning process through gentle sonication within an acetone solution, followed by a subsequent air-drying phase.

Subsequently, the wafer was subjected to a spin-coating process using NR-9 3000 photoresist, administered at a spin speed of 3500 rpm, bolstered by an acceleration of 500 for a duration of 45 seconds. The coated wafer was subjected to baking on a hotplate at 150°C for 60 seconds and then underwent exposure within a Heidelberg MLA150 Laser Writer machine, with emission occurring at a wavelength of 365 nm with an energy dose of 570 mJ/cm². Post-exposure, an additional baking step was executed on a hotplate set to 100°C for 60 seconds. A development phase of 20 seconds was performed by immersing the wafer in resist developer RD6, followed by a thorough rinsing in deionized water until the water's resistivity attained the specified threshold.

After a meticulous air-drying process, the silicon wafer was subjected to a comprehensive cleaning procedure within the Plasma Etch PE100 machine, immediately preceding its

introduction into the Oxford Plasmalab 80+ RIE machine for dry etching. The execution of 44 etching cycles was embarked upon, encompassing a cumulative duration of 16 minutes. The resultant T-junction channel, incorporating both inlets and outlets, spanned a length of 2.8 cm, exhibited a width of 1 mm, and possessed a depth of 50 µm, in addition to featuring integrated mixing components. This detailed fabrication process orchestrates a complex interplay of precise methodologies to realize the intended microfluidic architecture.

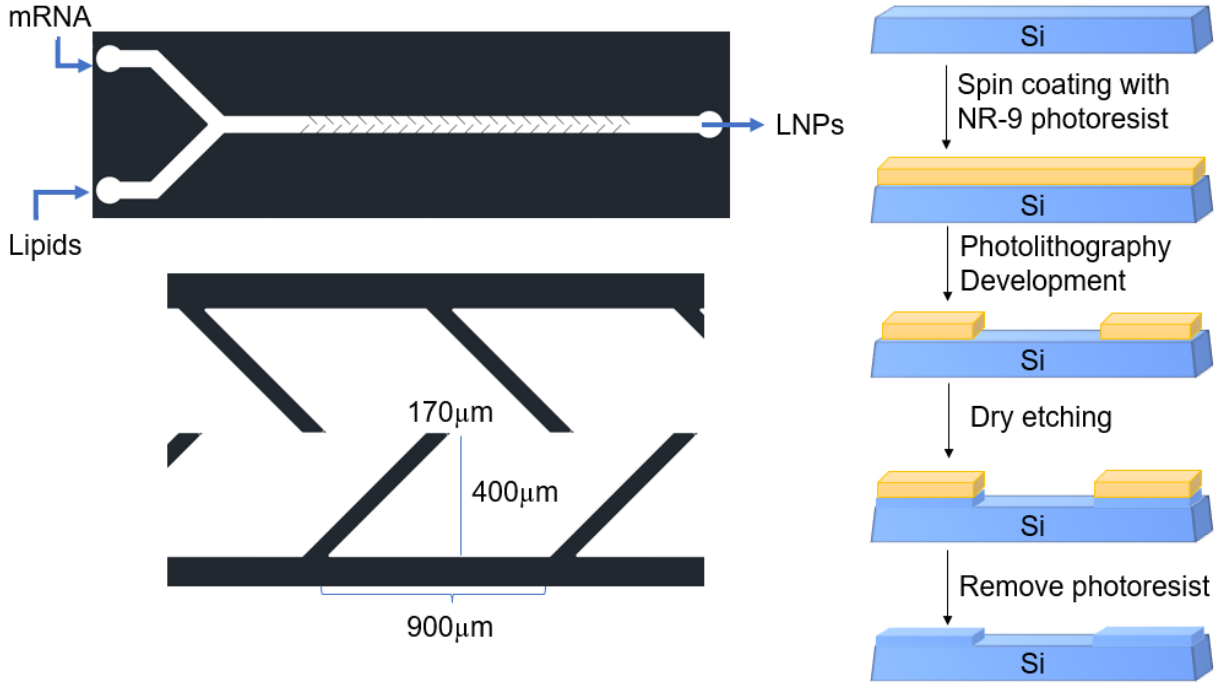


Figure 3.1 The schematic representation of the microfluidics pattern designed with AutoCAD for silicon photolithography and dry etching.

To prevent the undesirable adhesion of polydimethylsiloxane (PDMS) to the master mold, a silanization process was meticulously carried out on the etched silicon mold. This procedure involved exposing the silicon mold to a silane agent within a vacuum desiccator for a duration of 15 minutes, resulting in the formation of a monolayer on the surface of the mold. Subsequently, the wafer bearing the silanized mold was subjected to a baking process on a

hotplate, with the temperature set at 150°C, and this was maintained for a period of 10 minutes. This heat treatment served the dual purpose of curing the silane monolayer and facilitating the evaporation of any excess silane residue.

### 1.2 Fabrication of SU-8 photoresist microfluidics silicon molds.

To further downsize the lipid nanoparticles (LNPs), another microfluidic channel was meticulously designed and manufactured employing SU-8 photoresist on a silicon wafer. The intricate design blueprint was meticulously rendered through AutoCAD software and is visually delineated in Figure 3.2. The fabrication process entailed a layered approach (Figure 3.3), with the first mixing layer commencing by applying SU-8 2005 photoresist at a rotational speed of 3000 rpm for a duration of 45 seconds. Subsequent baking at 95°C was performed for 2 minutes to enhance the structural integrity. Following this, a coating of SU-8 2050 photoresist at 3000 rpm for 45 seconds was executed, succeeded by baking at 65°C for 3 minutes and then at 95°C for 6 minutes.

The prepared wafer underwent exposure within a Heidelberg MLA150 Laser Writer machine, emitting light at a wavelength of 375 nm with an energy dose of 2000 mJ/cm². Post-exposure, the wafer was subjected to another baking session, this time at 65°C for 1 minute followed by 95°C for 5 minutes. A development stage lasting 5 minutes was executed, involving immersion in MicroChem's SU-8 developer, followed by a meticulous rinsing process in deionized water until the resistivity of the rinsing water met the prescribed standard. The first layer of this multi-layered structure attained a thickness of 70 µm.

For the fabrication of the second layer, featuring herringbone structures, SU-8 2050 photoresist was evenly coated at a rotational speed of 4500 rpm for a duration of 45 seconds. This was succeeded by baking at 65°C for 5 minutes, succeeded by another baking at 95°C for a

span of 20 minutes. The exposed wafer was subjected to the Heidelberg MLA150 Laser Writer machine, employing a wavelength of 375 nm at an energy dose of 2000 mJ/cm². Following exposure, the wafer underwent subsequent baking sessions, first at 65°C for 5 minutes and then at 95°C for 10 minutes.

The ensuing development phase spanned 4 minutes, involving immersion in MicroChem's SU-8 developer, followed by an exhaustive rinsing process in deionized water until the resistivity of the rinsing water attained the prescribed threshold. The resulting second layer featured a thickness of 25 µm, thus culminating in the fabrication of a multi-layered structure with intricate herringbone features, primed for applications in enhancing the size reduction of LNPs. The fabrication conditions were shown in Table 3.1.

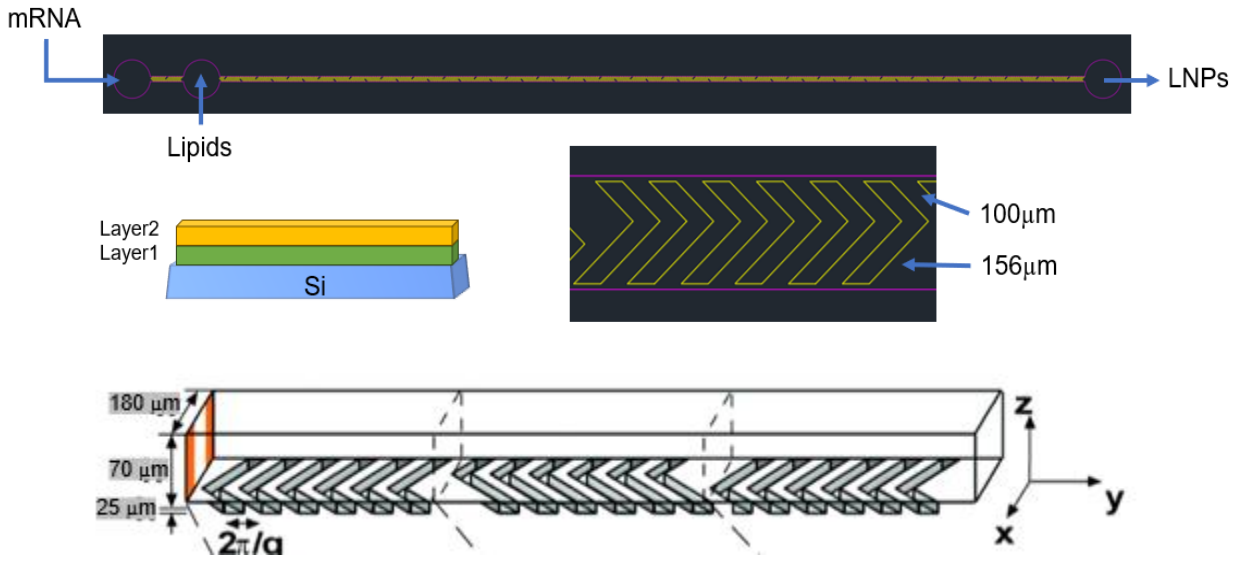


Figure 3.2 The schematic representation of the microfluidics pattern designed with AutoCAD and fabricated with SU-8 photoresist.

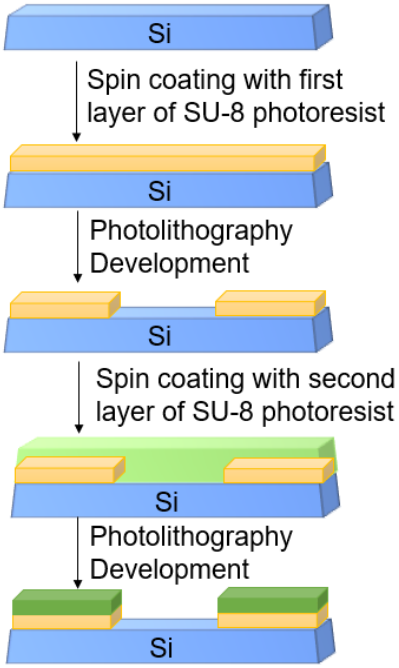


Figure 3.3 The fabrication steps for SU-8 photoresist silicon mold.

Table 3.1 The fabrication conditions for SU-8 photoresist

| | Photo resist | Spin coating conditions | Pre-exposure baking condition | Post-exposure baking condition |
|---|---|---|---|---|
| Mixing channel | SU-8 2005 | 3000 rpm, 45 seconds | 95°C, 2 minutes | 65°C, 1minute<br>95°C, 5 minutes |
| | SU-8 2050 | 3000 rpm, 45 seconds | 65°C, 3 minutes<br>95°C, 6 minutes | |
| Herringbone channel | SU-8 2050 | 4500 rpm, 45 seconds | 65°C, 5 minutes<br>95°C, 20 minutes | 65°C, 5 minutes<br>95°C, 10 minutes |

To prevent the undesirable adhesion of polydimethylsiloxane (PDMS) to the master mold, a silanization process was meticulously carried out on the SU-8 photoresist mold. This procedure involved exposing the silicon mold to a silane agent within a vacuum desiccator for a

duration of 15 minutes, resulting in the formation of a monolayer on the surface of the mold. Subsequently, the wafer bearing the silanized mold was subjected to a baking process on a hotplate, with the temperature set at 150°C, and this was maintained for a period of 10 minutes. This heat treatment served the dual purpose of curing the silane monolayer and facilitating the evaporation of any excess silane residue.

### 1.3 Fabrication of PDMS device.

In accordance with the experimental protocol, a precise mixture of 23 grams of PDMS base and 2.3 grams of curing agent, maintaining a ratio of 10:1 as specified in the Polydimethylsiloxane (PDMS) kit (SYLGARD™ 184 Silicone Elastomer Kit, Dow), was meticulously prepared. This PDMS mixture was then transferred to a plastic weighing dish, specifically a Polystyrene weighing dish with a capacity of 50 mL from Uline, and thoroughly homogenized. Subsequently, the weighing dish containing the PDMS mixture was carefully placed within a vacuum desiccator to facilitate the removal of any entrapped bubbles.

Following the deaeration process, the PDMS mixture was cast into a silicon mold and subjected to curing in an oven maintained at a temperature of 65°C. This curing process was extended overnight to ensure complete solidification. Subsequently, the PDMS slab was excised from the silicon mold using a scalpel, and the PDMS material was gently separated from the silicon wafer.

To prepare the PDMS device for further experimentation, both the PDMS piece and a glass slide (CHEMGLASS Microscope Cover made of Quartz measuring 19 mm x 19 mm, Grainger), were immersed in pure isopropanol (IPA, Thermo Scientific) and subjected to ultrasonic treatment for a duration of 5 minutes. Following this step, the PDMS piece and glass slide were allowed to air-dry.

To promote effective bonding between the PDMS and glass surfaces, the PDMS piece and the glass slide were subjected to a UV-ozone plasma treatment process using a UVO system. During this treatment, oxygen was supplied at a flow rate of 6 L/min for a period of 6 minutes. Immediately after the plasma treatment, the PDMS piece was affixed to the glass slide, ensuring the removal of any air bubbles. To further enhance the bonding strength, the assembled device was placed on a hotplate and maintained at a temperature of 80°C for a duration of 3 hours, thereby solidifying the attachment.

### 1.4 Formulation of LNPs

The ionizable lipids employed in this experimental investigation were subject to a synthesis and purification process, which included the use of mass spectrometry (MS) and nuclear magnetic resonance (NMR) techniques to ensure their integrity and quality. These lipids were subsequently dissolved in ethanol to achieve a specified concentration. The mRNA employed in the encapsulation experiments, specifically the CleanCap Firefly luciferase mRNA (Catalog Number L-7602) sourced from TriLink Biotechnologies, underwent a dilution process using a citrate buffer to attain the required concentrations.

The flow of the lipid solution within the PDMS microfluidics devices was meticulously regulated using a syringe pump (Harvard Apparatus Pump 11 Elite Programmable Syringe Pumps, Grayline Medical), maintaining a consistent flow rate of 500 µL/min with a targeted volume of 60 µL. Conversely, the mRNA solution was administered at a flow rate of 1.5 mL/min, with a targeted volume of 180 µL. This ensured precise control over the experimental parameters and volumes.

Following the mixing of these solutions within the microfluidics channels, the resultant LNPs solution was carefully collected in 10kDa dialysis cassette and subjected to a minimum of

2 hours of dialysis before being subjected to a filtration process using a 0.22 μm PSA syringe filter. This comprehensive procedure ensured the readiness and suitability of the LNPs for subsequent experimentation and analysis.

Before injection of LNPs for mice model, we employed a dynamic light scattering instrument (Zetasizer, Malvern Panalytical) to perform a comprehensive characterization of the LNPs produced. This characterization encompassed the determination of critical parameters such as particle size, polydispersity index (PDI), and Zeta potential, which collectively provide insights into the LNPs' physicochemical properties.

To assess the encapsulation efficiency of mRNA within the LNPs, we utilized the Quant-iT RiboGreen reagent (Life Technologies). The quantification of RNA within the LNP formulation involved the creation of a standard curve through a series of dilutions derived from the corresponding RNA standard stock solution. Both the standards and the test samples underwent dilution using 1x Tris-EDTA (TE) buffer, pH 8.0, with the aim of achieving a final sample concentration of 0.1 ng $\mu L^{-1}$ in the polystyrene cuvette. Fluorescence measurements were conducted utilizing a spectrofluorophotometer (Varian Cary Eclipse) configured for 500 nm excitation and 525 nm emission wavelengths.

The standard curve was constructed by employing linear regression analysis to correlate the fluorescence intensity against the concentration of the standard RNA. The quantification of RNA encapsulated within the LNPs was determined by comparing the fluorescence signal emitted by the RNA-binding fluorescent dye RiboGreen in two distinct conditions: absence and presence of a detergent (0.1% Triton X-100). In the absence of detergent, the signal exclusively originated from accessible, unencapsulated RNA. Conversely, in the presence of detergent, the LNPs were disrupted, causing the measured signal to encompass both encapsulated and non-encapsulated

RNA. This method allowed us to quantitatively evaluate the extent to which the mRNA was successfully encapsulated within the LNPs, providing valuable information about the efficiency of our encapsulation process.

### 1.5 Delivery of LNPs in mice models

Following the thorough characterization process, LNPs demonstrating optimal attributes were subject to dilution and administered via injection into the mice subjects. The desired properties for these LNPs included a size below 100 nm, indicative of their nano-scale nature, and notably high encapsulation efficiency. Furthermore, the ideal polydispersity index (PDI) for these LNPs was stipulated as equal to or less than 0.3, signifying a narrow size distribution. Additionally, considering the use of negatively charged lipids in the LNPs' composition, the preferred zeta potential range for these LNPs was desired to be neutral. These stringent criteria were employed to ensure the optimal performance and therapeutic potential of the LNPs in vivo.

Add information: All animal use was in accordance with the guidelines and approval from the University of California, San Diego Animal Care Program. Female BALB/c mice aged 7 months were purchased from Envigo. 0.2 mg/kg of mRNA-LNPs in Phosphate Buffered Saline (PBS) were injected into animals intraperitoneally (100 μL), and intravenously (100 μL) with 1 mL syringe with 27G needle using standard techniques (Machholz et al).

### 1.6 Luminescence and fluorescence imaging studies

Bioluminescence imaging was performed with an IVIS Spectrum imaging system (Caliper Life Sciences). Mice were administered D-luciferin (Regis Technologies) at a dose of 2 mg/kg after 7 hours of intraperitoneal injection. Mice were anesthetized after receiving D-luciferin in a chamber with 3% isoflurane (Piramal Healthcare Limited) and placed on the imaging platform while being maintained on 2% isoflurane via a nose cone. Mice were imaged at 15 minutes post

administration of D-luciferin using an exposure time of 30 seconds or longer to ensure that the signal acquired was within effective detection range (above noise levels and below CCD saturation limit). Luminescence values were quantified by measuring photon flux (photons/second) in the region of interest where bioluminescence signal emanated using the Living IMAGE Software provided by Caliper.

For fluorescence imaging of DID-labeled LNPs, euthanize the mice in a chamber with a CO2 fill rate of 30–70% of the chamber volume per minute. Dissect the mouse and collect the major organs (heart, lungs, liver, spleen, and kidneys) and blood for blood circulation experiments. The same pieces of tissue (I mean the same weight) were placed into 1xPBD + 1% SDS. Tissues were homogenized, then samples were sonicated for 5 min and then 5 min 20K rpm spin was performed. 10 uL of supernatant was added to the 90 uL of 1xPBSD and read out. Fluorescence intensity was detected by Tecan plate reader. Parameters: ex 644 nm em 689 nm, gain 20 nm, gain value 225.

## 2 Results

### 2.1 Characterization of LNPs made with silicon etched PDMS device.

In this study, ionizable lipids were combined with DSPC, cholesterol, and PEG-2000 in varying ratios, along with mRNA at specified concentrations. These constituents were introduced into a polydimethylsiloxane (PDMS) microfluidic device. Within this device, LNPs were fabricated utilizing a silicon etched mold characterized by a 1mm width. The production process involved the precise manipulation of flow rates to achieve the desired LNP formulations. Lower flow rates were specifically employed to generate LNPs, and the results are meticulously presented in Figure 3.4. For the lipid solution, a mixture of DSPC, cholesterol, and PEG-2000 in

different molar ratio, the flow rate was set at 466 µL/min, while the mRNA solution was administered at a flow rate of 1.4 mL/min.

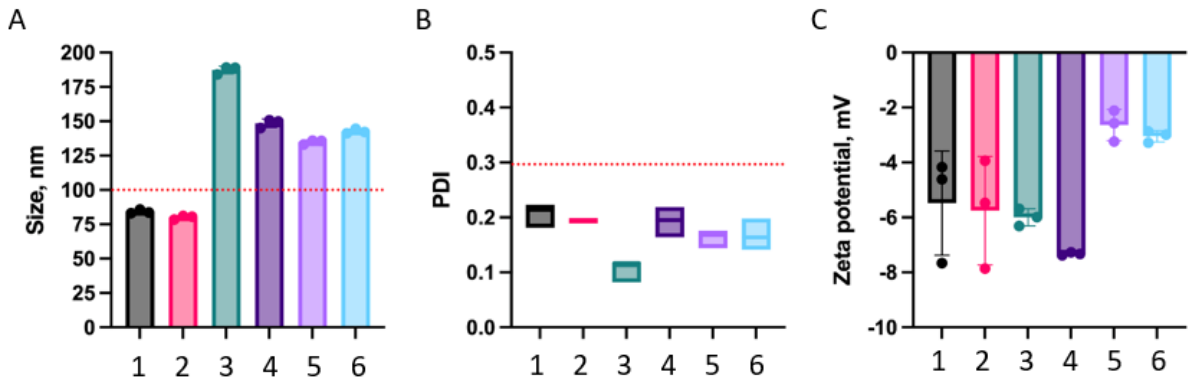


Figure 3.4. Size, PDI and zeta potential for mRNA encapsulated LNPs

Upon characterization, it was observed that the majority of the generated LNPs exhibited diameters exceeding 100 nm, except for lipid 1 and 2 within the experimental dataset. Remarkably, the polydispersity index (PDI) values consistently fell within the desired range, which was defined as being less than 0.3. Additionally, the zeta potential values spanned from -2 to -8, indicative of the surface charge properties of the LNPs. Encapsulation efficiencies were quantified utilizing the Quant-iT RiboGreen reagent and are itemized in Table 3.2. LNPs 1, 2, and 5 showcased remarkably high encapsulation efficiencies, exceeding 90%, while the remaining LNPs exhibited values ranging from 66% to 84%.

Typically, LNPs intended for mRNA delivery to the liver, our target organ, are ideally designed to exhibit diameters of less than 100 nm, with an optimal size falling within the range of 60 to 80 nm. To attain this desired size range, adjustments were made by increasing the flow rates for both the lipid and mRNA solutions to 660 µL/min and 2 mL/min, respectively.

As demonstrated in Figure 3.5a, the modifications in flow rates led to a significant reduction in the sizes of the LNPs produced using three distinct lipid formulations, in comparison to those generated with lower flow rates in T-junction microfluidic devices and the conventional pipetting method.

Table 3.2 mRNA encapsulation efficiency for different LNPs

| Sample | 1 | 2 | 3 | 4 | 5 | 6 |
|---|---|---|---|---|---|---|
| Encapsulation efficiency (%) | 92.38 | 92.74 | 66.88 | 74.46 | 96.93 | 83.79 |
| Concentration (ng/ μL) | 49.96 | 53.04 | 39.55 | 40.01 | 51.57 | 50.59 |

Furthermore, the stability of LNPs produced with lipid 1 was assessed over a 10-day period in a PBS solution at room temperature. Remarkably, the particle sizes remained unchanged for both high and low flow rate preparations, underscoring the robust stability of these LNPs.

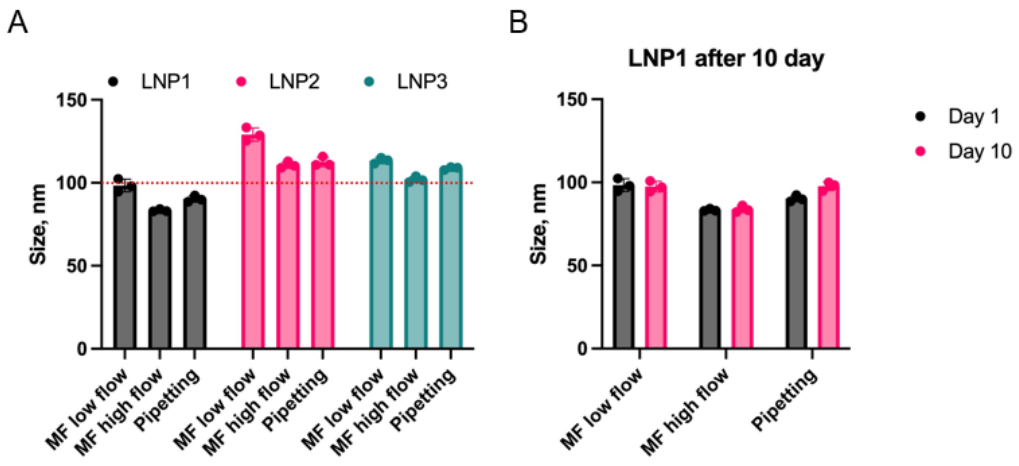


Figure 3.5 The size of the LNPs reduced by increasing the flow rates of lipid and mRNA solutions produced by microfluidic device.

Nevertheless, it's worth noting that, apart from LNPs created using lipid 1, the particles produced with the other two lipids at higher flow rates still exhibited diameters exceeding 100 nm. Furthermore, the elevation in flow rates led to an increase in pressure within the microfluidic device, resulting in issues related to leakage. This had a substantial impact on production efficiency and resulted in significant solution wastage. Consequently, a redesign of the device became imperative.

## 2.2 Characterization of LNPs made with SU-8 silicon PDMS device.

A novel silicon mold was meticulously crafted, featuring a width of 180 µm. This mold consisted of two distinct layers: the first layer comprised a 70 µm mixing channel, while the second layer incorporated a 25 µm herringbone structures channel. The manufacturing process involved the utilization of SU-8 photoresist, which was employed to create the structure through photolithography on the surface of a silicon wafer. For the experimental setup, the flow rate of the lipid solution was precisely adjusted to 500 µL/min with a corresponding volume of 60 µL.

Similarly, the flow rate of the mRNA solution was meticulously set at 1.5 mL/min, with a volume of 180 µL.

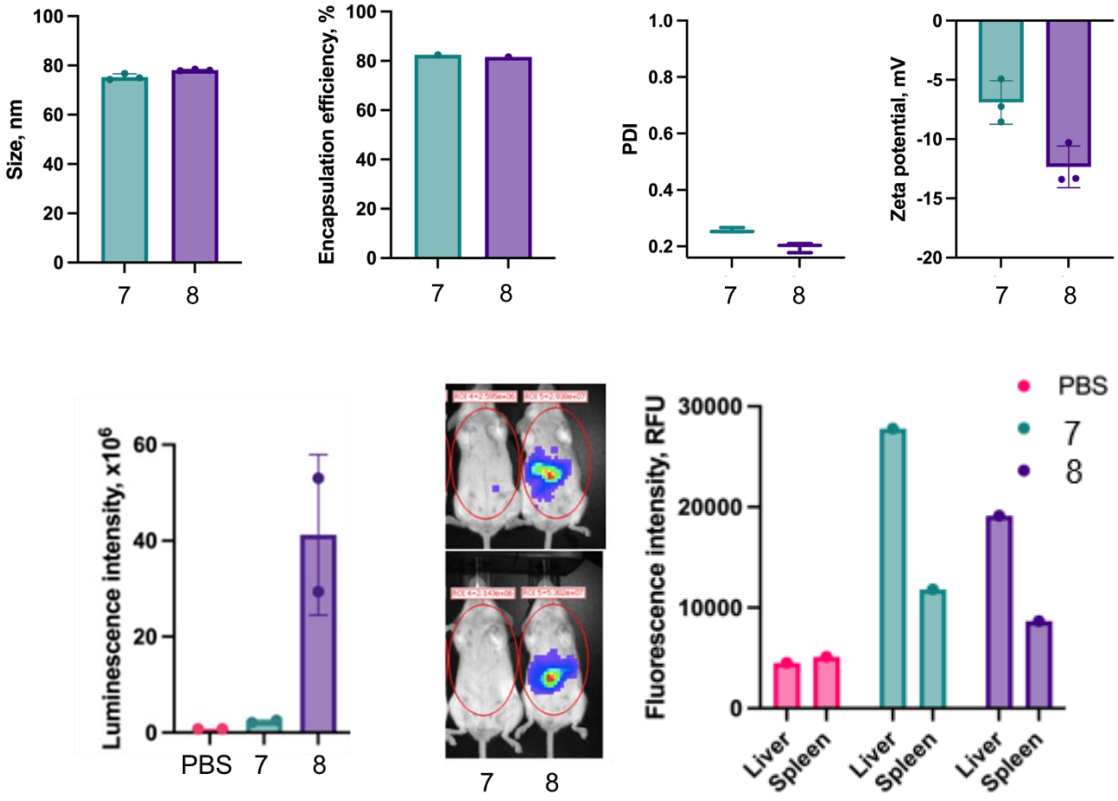


Figure 3.6 Size, encapsulation efficiency, PDI, zeta potential, luminescence intensity and fluorescence intensity for LNPs made with structure modified Alc 315-DSG lipids, and Alc 315-DSG lipids.

As illustrated in Figure 3.6, the lipid nanoparticles (LNPs) crafted using both 315-TAGal-DSG and Alc-DSG exhibited sizes falling within the range of 77 to 79 nanometers. Both LNPs achieved an encapsulation efficiency of 80% and displayed a low polydispersity index (PDI, approximately 0.2). In terms of electrostatic properties, the zeta potential of LNPs formed with structure modified Alc 315-DSG lipids measured approximately -7, whereas for those produced with Alc 315-DSG lipids, the zeta potential was around -12.

Subsequently, 7 hours post-injection in murine subjects, we measured the luminescence intensities in the live animals and the fluorescence signals within the liver and spleen for both LNPs encapsulating mRNA and a negative control PBS solution. Notably, both LNPs demonstrated the ability to primarily transport mRNA payloads to the liver, the intended target organ, as opposed to the spleen. However, LNPs formulated with structure modified Alc 315-DSG lipids exhibited superior performance in this regard.

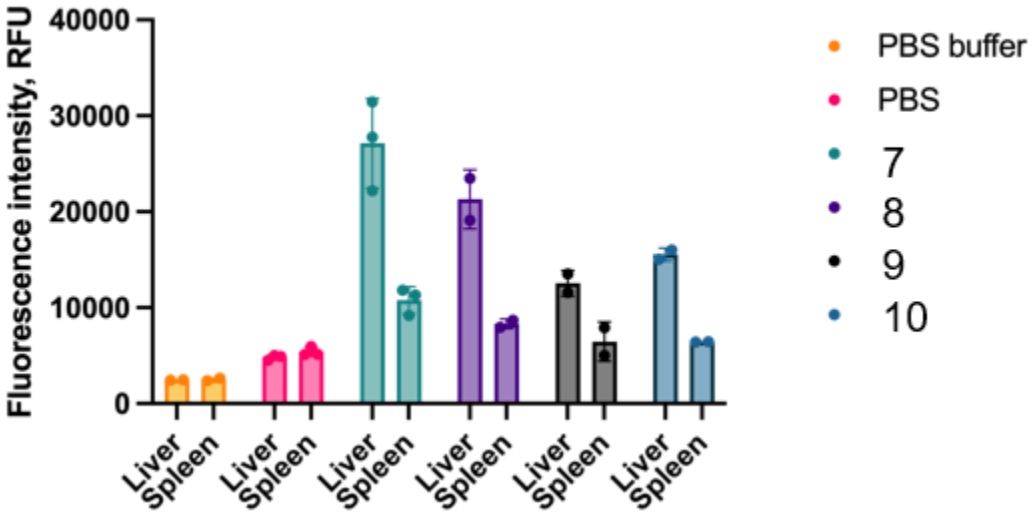


Figure 3.7 Fluorescence intensities in mouse liver and spleen of PBS buffer (negative control), PBS (negative control), lipids 7, 8, 9, and 10 made LNPs. (lipid 7: structure modified Alc 315-DSG, lipid 8: Alc 315- DSG, lipid 9: structure modified Alc 315- DSG with Glu, and lipid 10: structure modified Alc 315- DSG with PEG.)

To further substantiate the preferential mRNA delivery to the liver, the designated target organ, we employed the microfluidics-based approach to generate lipid nanoparticles (LNPs) using four distinct lipid formulations, lipid 7: structure modified Alc 315-DSG, lipid 8: Alc 315-DSG, lipid 9: structure modified Alc 315- DSG with Glu, and lipid 10: structure modified Alc 315- DSG with PEG. Subsequently, we assessed the fluorescence intensities generated by these four LNPs in comparison to both PBS and PBS buffer, employed as negative controls, shown in

Figure 3.7. The LNPs made with lipid 7, structure modified Alc 315-DSG, performed the best for target delivery of mRNA to liver comparing to others.

In accordance with Figure 3.8, lipid nanoparticles (LNPs) were synthesized utilizing lipids7, 8, 9, and 10. Subsequently, these LNPs underwent comprehensive characterization employing dynamic light scattering (DLS) analysis to assess their dimensions, polydispersity index (PDI), and zeta potential. The outcomes established that all four LNP variants exhibited diameters falling within the targeted range of 60 to 80 nanometers. Furthermore, the recorded PDI values consistently remained below 0.3, while zeta potential measurements demonstrated a spectrum ranging from -3 to -15, consistent with the anticipated behavior under physiological pH conditions of both 7.4 and lower pH conditions of 5.4.

It is imperative to highlight that the acidic environment within endosomal compartments triggers the protonation of ionizable lipids, leading to a notable shift in their electrostatic charge. This protonation event plays a pivotal role in facilitating endosomal escape and subsequently enabling the release of encapsulated payloads, such as mRNA, into the cytoplasm. This underscores the significance of assessing the zeta potential of LNPs under lower pH conditions, such as 5.4, mirroring the conditions encountered within the endosomal milieu.

In our investigation, we quantified the luminance intensities arising from the chemical reaction between D-luciferin and luciferase enzyme as an indicator of mRNA delivery efficacy. This assessment was performed on lipid nanoparticles (LNPs) encapsulating mRNA, specifically those composed of lipids 11, 12, 13, and 14. As a comparative baseline, phosphate-buffered saline (PBS) was employed as a negative control (see Figure 3.8E). Notably, among the various LNP formulations, it was observed that the highest luminescence signal was achieved when

utilizing LNPs comprised of lipid 12. This outcome underscores the superior mRNA delivery performance associated with this lipid composition.

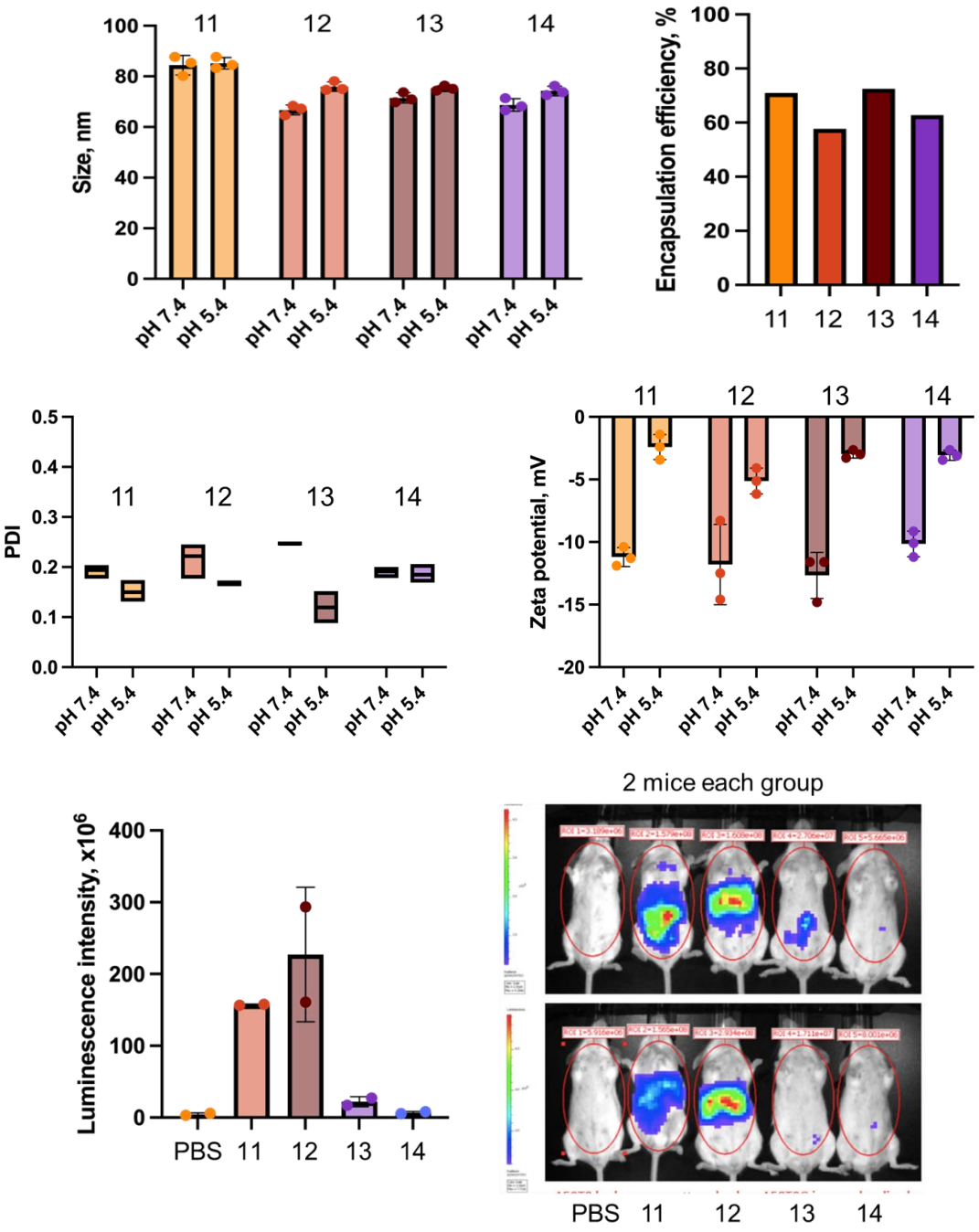


Figure 3.8 Size, encapsulation efficiency, PDI, zeta potential and luminescence intensity for LNPs made with 11, 12, 13, and 14 lipid solutions. (A: Alc 315 lipid, T: structure modified Alc 315 lipid. Lipid solution 11: A+T, 12: 11+ GalNAC targeting domain, 13: A+T in a different ratio, 14: 13+ GalNAC targeting domain)

However, despite these favorable physicochemical characteristics, the encapsulation efficiencies of all four LNP variants were observed to be less than 80%, which falls short of the requisite levels for efficient delivery within mouse models.

Lipid solution 15, 16, and 17 were used to make three kinds of LNPs and the characterization information for size, encapsulation efficiency, PDI and the luminescence intensity of delivered LNPs in the mice systems are shown in Figure 3.9.

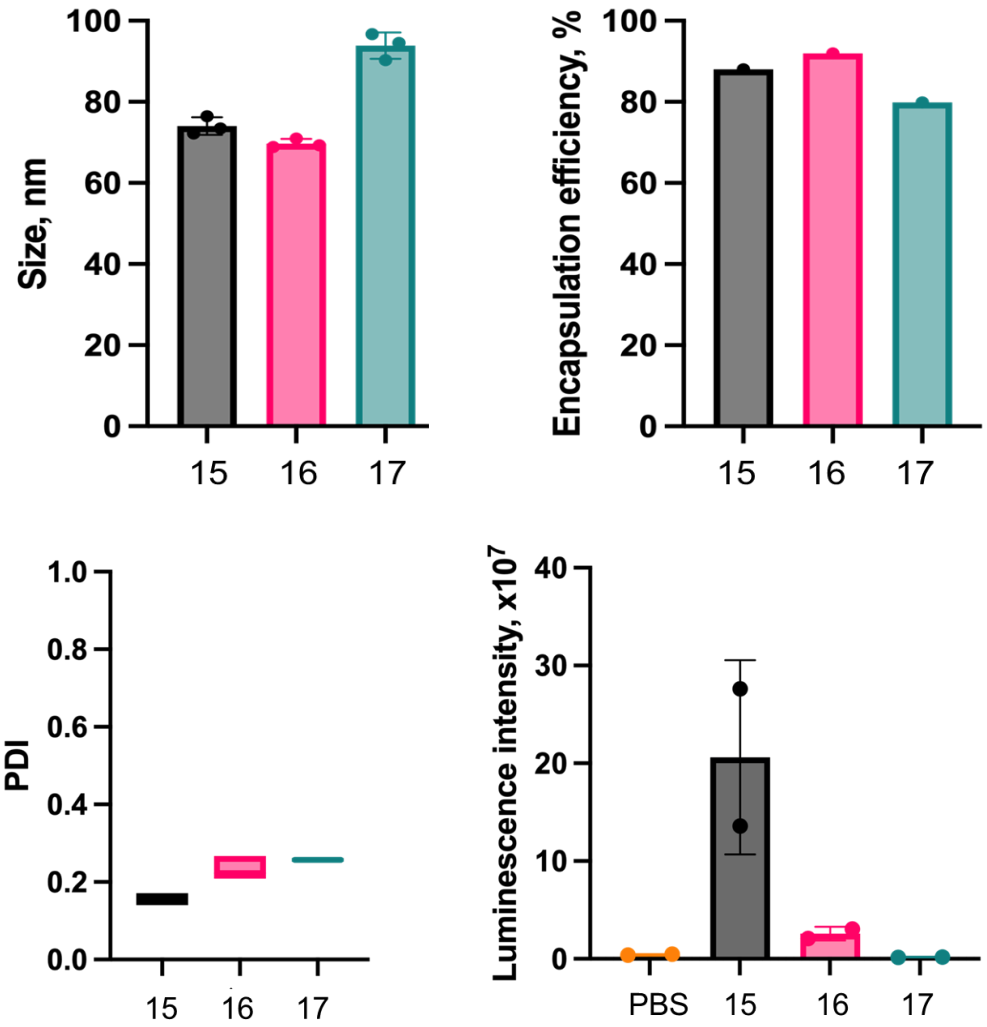


Figure 3.9 Size, encapsulation efficiency, PDI and luminescence intensity for LNPs made with lipid solutions 15, 16, and 17. (lipid solutions 15-17 were mixture of Alc 315 lipid and structure modified Alc 315 lipid in different ratios)

The dimensions of lipid nanoparticles (LNPs) constructed using lipid 15 and lipid 16 were approximately 70 nanometers in diameter, while LNPs formed with lipid 17 exhibited a slightly larger size, nearing 90 nanometers. In addition, the LNPs comprised lipid 15 displayed a lower encapsulation efficiency, approximately 80%, in contrast to the two other LNPs which achieved encapsulation efficiencies approaching 90%. Importantly, the polydispersity index (PDI) for all three LNP formulations fell within the range of 0.18 to 0.3, indicative of a relatively uniform particle distribution. Notably, among the three LNP types, those created using lipid 15 yielded the highest luminescence signals, underscoring their superior performance in facilitating the intended biological response.

As depicted in Figure 3.7, LNPs crafted with Alc-TAGal-DSG (lipid 7) and Alc-DSG lipids (lipid 8) exhibited notably elevated signals within the liver, indicative of effective delivery through the bloodstream. Conversely, LNPs produced with Alc-TAGlu-DSG (lipid 9) and Alc-PEG-DSG lipids (lipid 10) displayed relatively diminished signals within the liver. Given our primary objective of mRNA delivery to the liver while minimizing delivery to other organs, we intend to select the lipid formulations yielding higher liver-to-spleen signal ratios. These selected lipids will subsequently be employed in conjunction with a targeting domain modified GalNac, known to bind extensively with asialoglycoprotein receptors (ASGPR) highly expressed on liver cells.

Based on the outcomes of our prior in vivo mRNA delivery experiments, we have selected the Alc-DSG, ALC-TAGlu-A-DSG, and Alc-PEG-DSG lipids for conjugation with our modified GalNac targeting domain, which is designed to target liver cells. As depicted in Figure 3.10, there were no substantial alterations observed in terms of the sizes, encapsulation efficiencies, or polydispersity index (PDI) values of the lipid nanoparticles (LNPs) when

comparing those formulated with Alc-DSG, Alc-TA-Glc-DSG, and Alc-PEG-DSG lipids, both with and without the incorporation of the targeting domain represented by modified GalNac molecules.

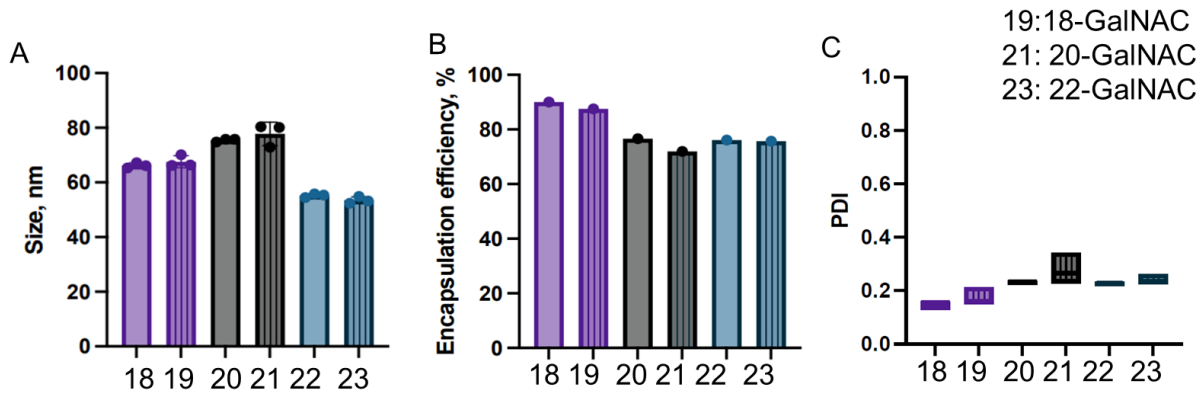


Figure 3.10 Size, encapsulation efficiency, PDI and zeta potential for LNPs made with lipids with and without targeting domain protein (modified GalNac). (lipid 18: Alc 315- DSG, lipid 19: lipid 18 + GalNac targeting domain protein, lipid 20: structure modified Alc 315- DSG with Glu, lipid 21: lipid 20 + GalNac targeting domain protein, lipid 21: structure modified Alc 315- DSG with PEG, and lipid 22: lipid 21 + GalNac targeting domain protein.)

As illustrated in Figure 3.10, the incorporation of the targeting domain molecule, GalNac, was found to have no discernible impact on the size or polydispersity index (PDI) of lipid nanoparticles (LNPs). Furthermore, the addition of this larger targeting domain molecule did not result in any significant alteration in the encapsulation efficiency of messenger RNAs (mRNAs). These observations collectively affirm the robustness and reliability of our microfluidics devices, designed, and fabricated for the production of LNPs with specific properties. Importantly, these findings underscore the device's consistent performance, even when subjected to variations in formulation.

## 3 Discussion

In this chapter of our study, we undertook the design and fabrication of two distinct microfluidic silicon molds, with the primary objective of facilitating the encapsulation of mRNA within lipid nanoparticles, intended for subsequent delivery to murine models. To achieve this, we synthesized two different types of ionized lipids, each prepared in varying ratios, to explore their influence on the resulting lipid nanoparticles (LNPs). These LNPs were subjected to rigorous characterization encompassing measurements of their size, encapsulation efficiency, polydispersity index, and zeta potential. This detailed assessment was conducted before the LNPs were administered via intraperitoneal (IP) and intravenous (IV) injection routes in our mouse model experiments.

The experimental evaluation of our LNP formulations in live mice involved the measurement of luminescent signals originating from the mRNA payloads within the animals, the assessment of fluorescent signals emanating from the mRNA within various organs, and the monitoring of mRNA circulation within the bloodstream. These assessments are essential in providing insights into the performance and efficacy of our mRNA delivery system within the murine model.

Our utilization of the custom-designed microfluidics device played a crucial role in achieving the desired characteristics of the LNPs. Specifically, our fabricated microfluidics device enabled the production of LNPs with sizes ranging from 60 to 80 nanometers, high encapsulation efficiency, a monodisperse distribution, and the attainment of the desired zeta potential. These optimized LNPs hold great promise for enhancing the targeted delivery of mRNA to specific organs within the mouse model, marking a significant advancement in our research endeavor.

CHAPTER 4

# 1 Materials and Methods

## 1.1 Nitrogen-cold plasma set-up

Nitrogen gas underwent ionization through exposure to a 15 kV alternating current (AC) source, resulting in the generation of cold plasma at a temperature of 35°C shown in Figure 4.1. The high voltage AC source was constructed by interconnecting a 3.5 V direct current (DC) power supply (Lwlongwei DC Power Supply Variable, 30V 10A), a DC/AC converter, and a step-up transformer (Miniature DC 3.6~6V to 20KV High Voltage Transformer), as illustrated in Figure 4.2.

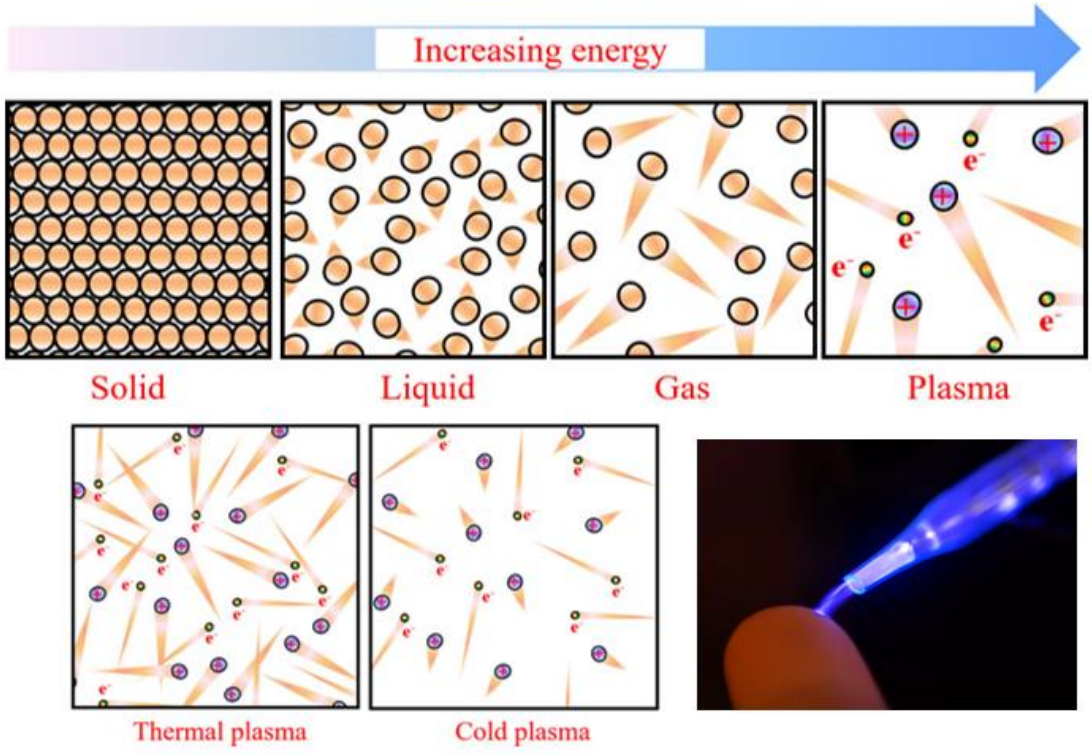


Figure. 4.1 Ionization of nitrogen gas with high AC voltage to produce cold plasma.

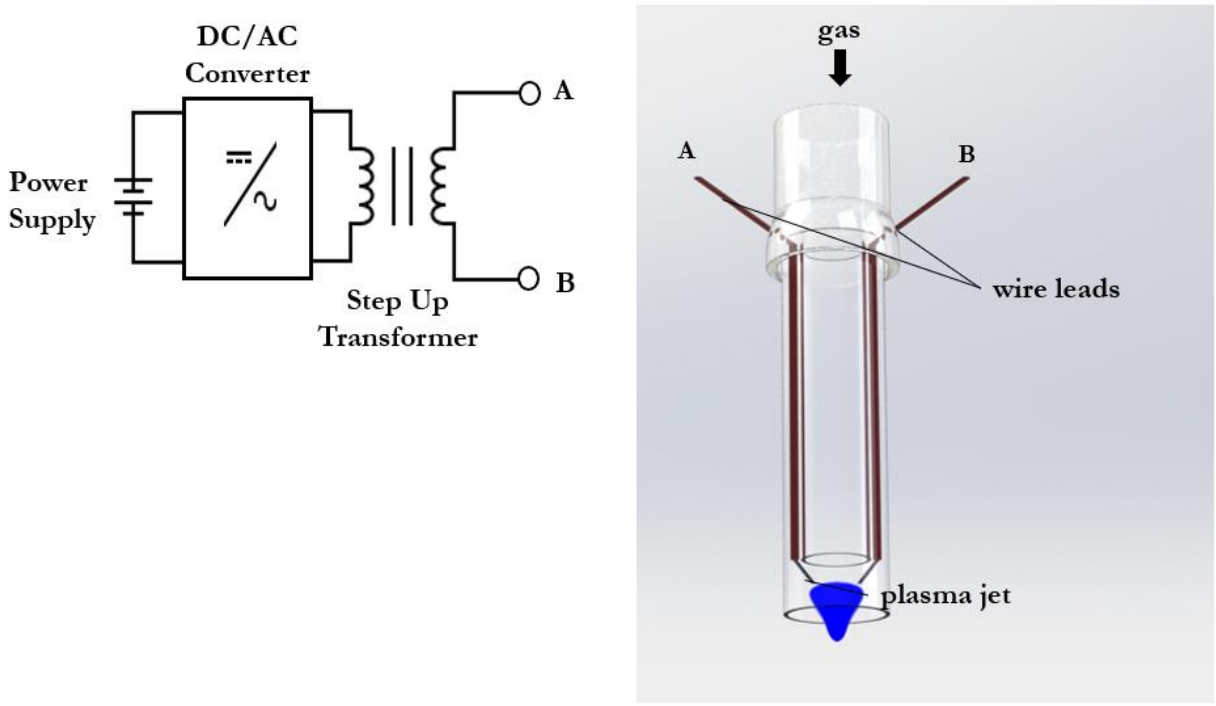


Figure. 4.2 Set-up of cold plasma jet.

The DC/AC converter and the step-up transformer were affixed onto a heat sink (TEC1-12706 Heat Sink Thermoelectric Cooler Peltier Plate Module) using a layer of thermos-glue (SYY 2 Grams CPU Paste Thermal Compound Paste, Shenzhen Tensan Co,.Ltd, B07BNDPKL5) for thermal management. An electric fan was strategically situated beneath the heat sink to facilitate the dissipation of heat generated during the operational phases of the plasma configuration. A pair of electrons, linked to the high voltage source, were positioned between the inner and outer glass tubes. These electrons were strategically positioned with their tips in proximity to the outer glass edge. Nitrogen gas (N2) was meticulously regulated via a gas mass meter (SmartTrak® 50 Digital Mass Flow Controllers & Mass Flow Meters) to maintain a consistent flow rate. Subsequently, the N2 gas was introduced into the plasma system through the interconnected tubes.

## 1.2 Cold plasma treatment on adherent cells

For the cold plasma treatment experimentation, we employed MCF-7 adherent cells (human breast cancer cell line, ATCC). The cells were allowed to adhere to the base of the petri dish in a culture medium, reaching this state approximately twelve hours after seeding. The specifics of the treatment conditions are comprehensively outlined in Table 4.1, encapsulating a comprehensive overview of the parameters governing the experimental protocol.

Table 4.1 Parameters of cold plasma jet treatment on adherent cells

| Distance between plasma jet and sample (mm) | N2 flow rate (L/min) | Treatment time (min) |
|---|---|---|
| 5 | 8 | 2 |
| | | 4 |
| | | 6 |
| | | 8 |
| | | 10 |

Upon removal of surplus cell culture medium, a succession of microscopy images was captured for MCF-7 cells within a designated region. These images encompassed the cellular state prior to treatment as well as at 2, 4, 6, 8, and 10 minutes post the cold plasma exposure. The imaging was executed utilizing a Keyence microscope. After the 10-minute treatment interval, the cells were re-suspended within the culture medium. The acquired images were subsequently

juxtaposed with the initial images, allowing for a systematic assessment of the cellular responses to the cold plasma treatments.

### 1.3 Cold plasma treatment on proteins

As part of our investigation into cold plasma treatment effects, we expanded our experimental scope to include rabbit immunoglobulin G (IgG) protein (Rabbit IgG Isotype Control, ThermoFisher Scientific), thereby elucidating the impact of cold plasma on protein entities. The specific conditions under which these experiments were conducted are meticulously documented in Table 4.2, providing a comprehensive overview of the parameters guiding the study. Employing a consistent treatment distance, we executed two distinct trials employing varying nitrogen flow rates, each corresponding to differing treatment durations. This deliberate bifurcation facilitated a comprehensive assessment of the interplay between nitrogen flow rate, treatment duration, and the resultant protein responses to cold plasma exposure.

The assessment of binding efficiency between plasma-treated and untreated rabbit immunoglobulin G (IgG) proteins was conducted utilizing an Enzyme-Linked Immunosorbent Assay (ELISA) protocol. In this process, a 96-well plate was meticulously coated with 20 µg/mL of anti-rabbit IgG capture antibody within 100 µL of BupH Carbonate-Bicarbonate Buffer Packs (Cat. No. 28382) per well, followed by an overnight incubation at 4°C. Subsequently, the capture antibody solution was removed, and a singular washing step was performed using either Tris-buffered or phosphate-buffered saline containing 0.05% Tween 20 detergent (Pierce 20X TBS Tween 20 Buffer, Cat. No. 28352, or Pierce 20X PBS Tween 20 Buffer, Cat. No. 28360).

Table 4.2 Parameters of cold plasma jet treatment on rabbit Igg proteins.

| Distance between plasma jet and sample (mm) | N2 flow rate (L/min) | Treatment time (min) |
|---|---|---|
| 5 | 5 | 1 |
| | | 3 |
| | 8 | 1 |
| | | 3 |

Table 4.3 Parameters of cold plasma jet treatment on anti-rabbit Igg proteins.

| | |
|---|---|
| Concentrations of rabbit Igg solution for control ELISA experiments (ng/mL) | 5000, 1000, 500, 100, 10,1, 0.1, negative |
| Concentrations of cold plasma treated rabbit Igg solution for ELISA experiments (ng/mL) | 1000, 100, 10, 1, negative |

Each well underwent a blocking step with over 300 µL of SuperBlock (TBS) Blocking Buffer (Cat. No. 37535) for a duration of one hour at room temperature. Following the removal of the blocking buffer and a single washing iteration, 100 µL of rabbit IgG solution, featuring concentrations delineated in Table 4.3, was added to each well, subsequently incubated at room temperature for one hour. After five washing cycles using the washing buffer, 100 µL of an HRP-conjugated anti-rabbit IgG detection antibody solution (Rabbit anti-Human IgG (H+L) Secondary Antibody, ThermoFisher Scientific), suitably diluted in a 1:2000 ratio with blocking

buffer, was introduced to each well. This incubation step spanned one hour at room temperature. For negative control samples, the blocking buffer served as the medium.

Following the removal of the detection antibody solution and subsequent washing cycles, 100 µL of a chemiluminescent substrate solution (N-Acetyl-3,7-dihydroxyphenoxazine or ADHP, Amplex® Red, Biotium) containing horseradish peroxidase (HRP) was meticulously introduced into each well. This substrate solution was meticulously prepared by combining one part of stable peroxide solution with a thousand parts of the working solution. The resulting mixture was then allowed to incubate at room temperature for a duration of 15 minutes.

Following the incubation period, the ensuing chemiluminescent signals were quantitatively assessed using a Keyence microscope. Notably, a brief exposure time of 1/800 was employed during the imaging process, thereby enabling the capture and measurement of the luminescent emissions emitted by the reaction between the HRP-labeled detection antibody and the chemiluminescent substrate.

This meticulous ELISA procedure enabled the quantitative evaluation of the interaction between plasma-treated and untreated rabbit IgG proteins, offering insights into their differential binding affinities within the experimental framework.

## 2 Results

### 2.2 Cold plasma treatment on adherent cells

MCF-7 cancer cells were meticulously seeded within 3 cm petri dishes, supplemented with cell culture media, and subsequently positioned within a controlled 37°C incubator for an

overnight incubation period. After the removal of any excess cell media, the cells underwent treatment with N2-cold plasma across diverse time intervals. It was noteworthy that a desiccated region became evident directly beneath the plasma jet; however, no discernible alteration in cell morphology was observed after treatments spanning durations of 2, 4, 6, 8, and 10 minutes. The consistent absence of significant morphological changes within these treated cells is comprehensively depicted in Figure 4.3, further affirming the controlled nature of the experimental conditions and the limited impact of the cold plasma on cellular morphology.

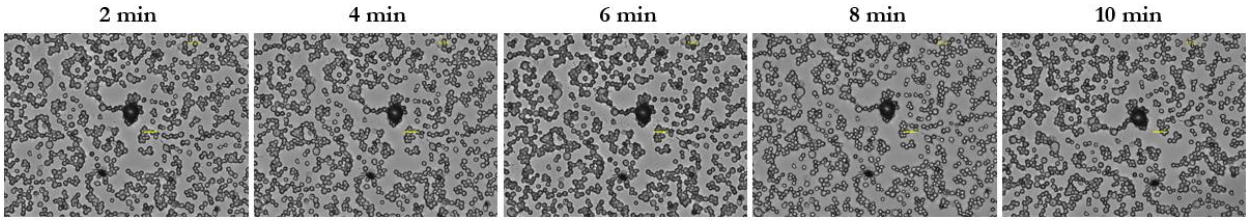


Figure 4.3 Microscope images for MCF-7 cells treated with cold plasma jet for 2, 4, 6, 8, and 10 minutes.

Nevertheless, following a 10-minute cold plasma treatment, a distinct phenomenon was observed: within the region subjected to plasma treatment, the adherent cells underwent lift-offs when subsequently rehydrated with cell culture media within a span of 2 minutes. This phenomenon is illustrated in detail within Figure 4.4. In stark contrast, the MCF-7 cells positioned outside the treated area sustained their adherence to the dish's bottom and conserved their spatial positioning. Consequently, it can be deduced that the controlled application of N2 cold plasma for specific time intervals exhibits the potential to instigate selective and specialized lithography of adherent cells, effectively manipulating their spatial arrangement within the experimental setup. This intriguing capability provides avenues for controlled cellular

manipulation and spatial patterning, indicative of the intricate interplay between plasma treatment and cellular behavior.

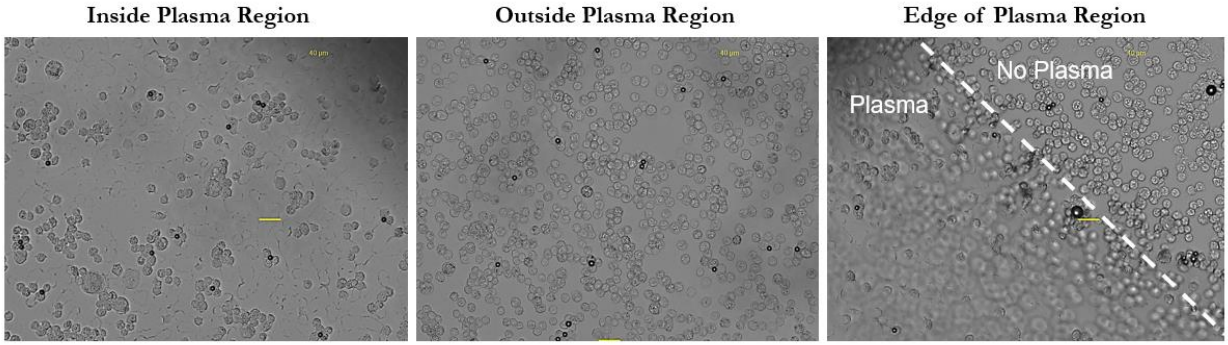


Figure 4.4 Microscope images for resuspended MCF-7 cells treated with cold plasma for 10 minutes.

## 2.3 Cold plasma treatment on proteins

The influence of cold plasma treatment on proteins was systematically evaluated by subjecting distinct concentrations of rabbit immunoglobulin G (IgG) solutions to a spectrum of treatment conditions. These conditions encompassed two distinct nitrogen (N2) flow rates—5 L/min and 8 L/min—along with two treatment durations of 1 minute and 3 minutes. Throughout these experiments, the treatment distance was maintained as a constant parameter.

Subsequently, to gauge the binding efficiency of both untreated and plasma-treated rabbit IgG proteins, a well-established Enzyme-Linked Immunosorbent Assay (ELISA) approach was adopted. The experimental setup comprised anti-rabbit IgG as the capture antibody and anti-rabbit IgG conjugated with horseradish peroxidase (HRP) as the detection antibody. These binding interactions facilitated the measurement of specific protein-protein interactions within the experimental framework.

The execution of this ELISA procedure was complemented by the introduction of a chemiluminescent substrate solution, which upon catalysis by the HRP-conjugated detection antibody, yielded luminescent signals. This chemiluminescence provided a quantifiable readout of the binding interactions taking place on the microplate surface. The resultant images were subsequently captured using a microscope, while the signal intensities were methodically analyzed using the widely utilized software, Image J. This multi-step assessment, elucidated in Figure 4.5, Figure 4.6 and Figure 4.7, affords a comprehensive evaluation of the effects of cold plasma on protein binding behavior and opens pathways for deeper insights into protein-plasma interactions within controlled experimental conditions.

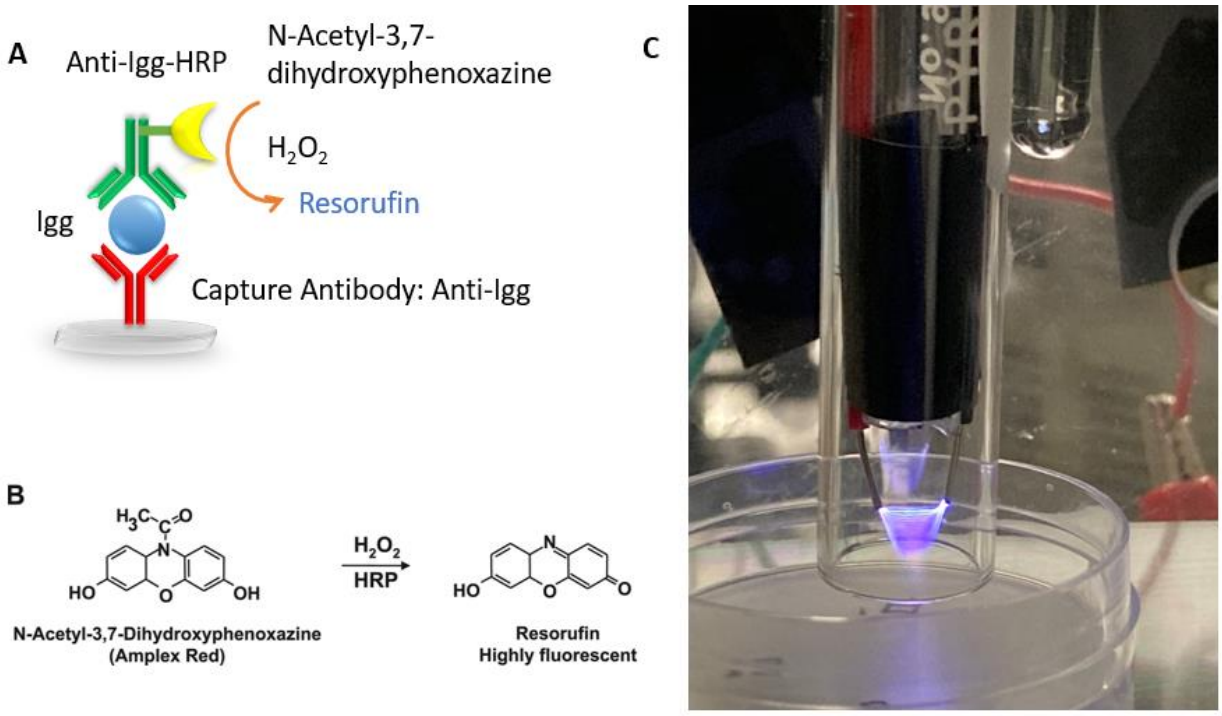


Figure 4.5 Experiment set-up for cold plasma treatment on rabbit IgG protein. A) Illustration of sandwich ELISA diagnosis of rabbit IgG protein. B) Chemiluminescent reaction of Amplex Red with hydrogen peroxide and HRP. C) The set-up of cold plasma treatments.

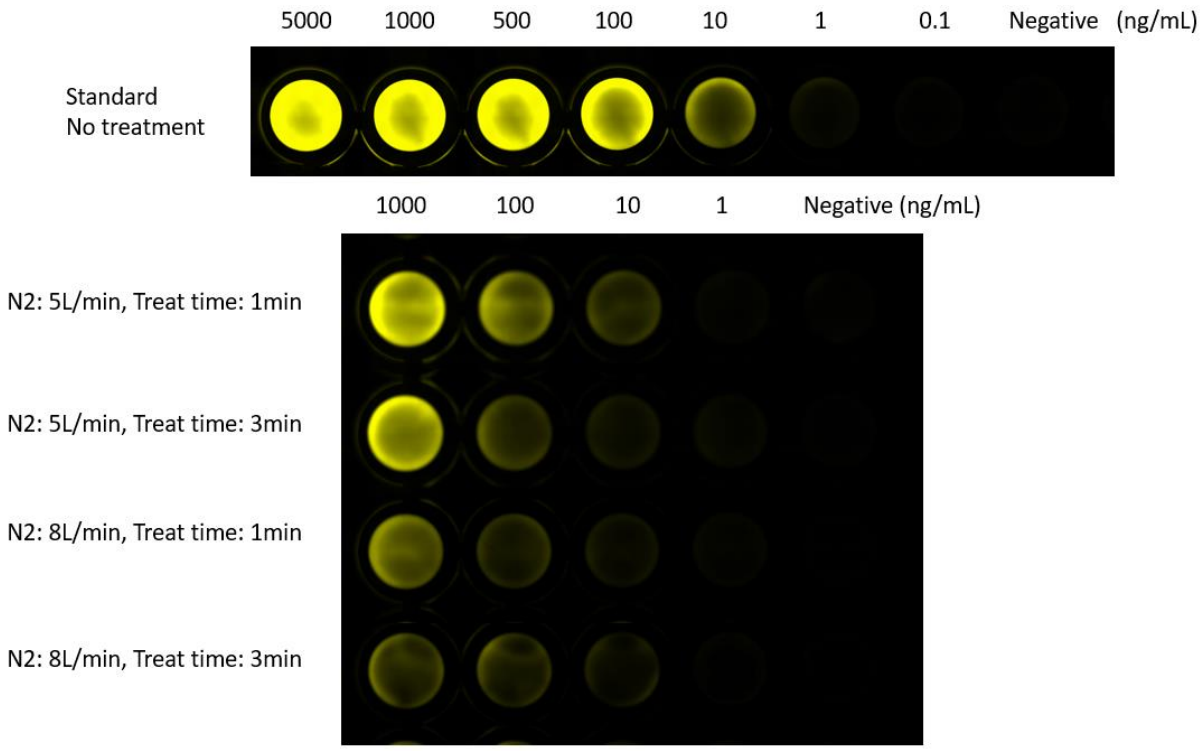


Figure 4.6 Luminescent images taken for untreated (control), and plasma treated rabbit IgG ELISA signals.

As illustrated in Figure 4.6, a noticeable reduction in luminescent signals was observed for the samples subjected to plasma treatment when contrasted with the untreated control samples. Notably, when subjected to identical nitrogen (N2) flow rates, an observable trend emerged wherein the signal intensity exhibited a discernible decrease as the treatment duration was extended. Similarly, under conditions of consistent treatment time, a parallel trend was observed: higher N2 flow rates were associated with lower signal intensities. This nuanced interplay between treatment parameters and resulting signal intensities underscores the intricate and interdependent relationship between cold plasma exposure and the resulting molecular interactions within the experimental milieu.

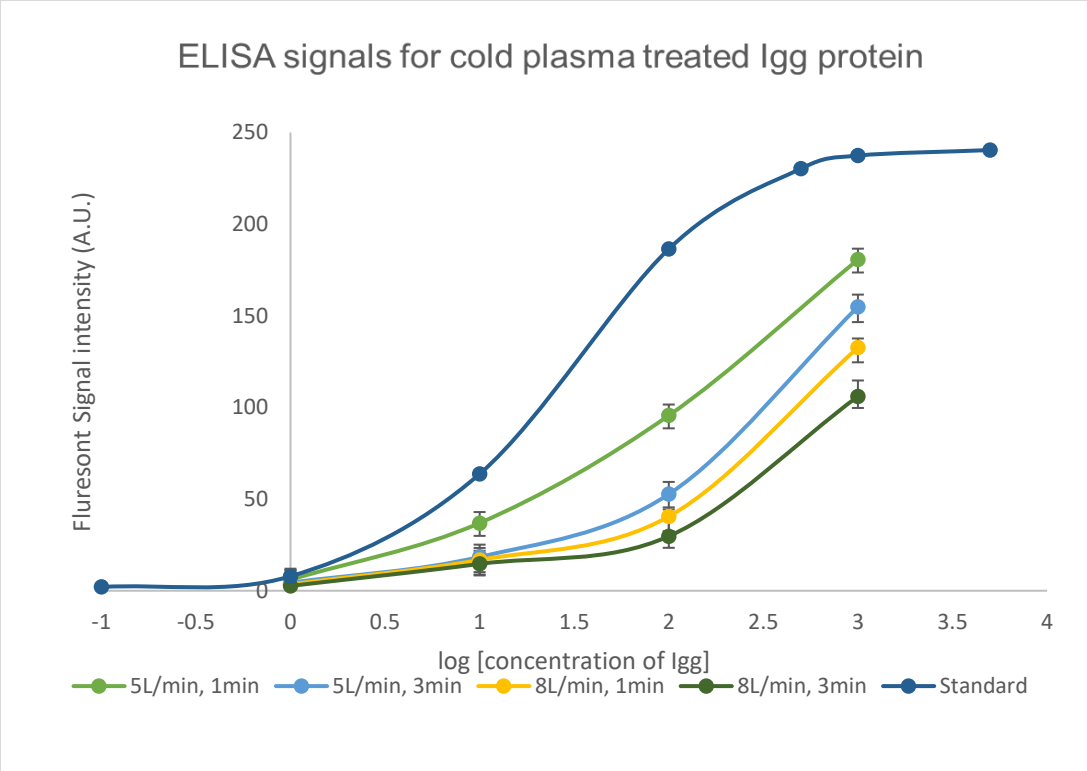


Figure 4.7 ELISA signals for untreated (control), and plasma treated rabbit IgG analyzed by image J.

The luminescent signal intensities presented in Figure 4.6 underwent subsequent comprehensive analysis employing the Image J software. The obtained data was subsequently plotted against the logarithmic values of the concentrations of rabbit immunoglobulin G (IgG) utilized in the Enzyme-Linked Immunosorbent Assay (ELISA) assays. In direct comparison with the standard curve constructed for samples devoid of plasma treatment, the resulting curves representing the treated samples exhibited a distinctive displacement towards the right within the plot. This pronounced shift signifies a substantial alteration in the binding dynamics of treated proteins.

## 3 Discussion

According to the cold plasma treated MCF-7 adherent cell experiments, it can be inferred that the deliberate and controlled administration of nitrogen (N2) cold plasma over defined time intervals manifests the inherent potential to trigger precise and specialized lithography of adherent cells. This strategic application of cold plasma governs the intricate spatial arrangement of these cells within the controlled experimental milieu. The emergent result is an innovative avenue for orchestrating regulated cellular manipulation and orchestrating spatial patterning, offering a deeper understanding of the intricate interplay between plasma treatment dynamics and cellular responses.

Fundamentally, in the cold plasma treated protein experiments, the conspicuous shift observed in the luminescent signal curves for ELISA assay representing treated samples towards the right on the plotted graph serves as a clear indicator of the substantial reduction in the binding efficiency of proteins ensuing from their exposure to cold plasma treatment. This phenomenon may be attributed to the plausible alteration of protein tertiary structures, potentially leading to the concealment of binding sites crucial for antibody recognition. This observation underscores a shift in protein conformation that directly affects their interaction with respective binding partners. The resultant binding affinity modifications carry profound implications for the comprehensive comprehension of the multifaceted interplay between cold plasma-induced molecular transformations and the inherent functionality of proteins.

The unfolding modifications in binding dynamics present captivating insights into the intricate biochemical mechanisms at play, shaping the intricate relationship between plasma-induced perturbations and the functional behavior of proteins. These narrative paints a comprehensive picture of the multifarious and dynamic molecular interactions resulting from

cold plasma exposure, contributing to the elucidation of the broader and interconnected mechanisms governing cellular responses to plasma treatments.

# REFERENCES


Baker, R. E., Mahmud, A. S., Miller, I. F., Rajeev, M., Rasambainarivo, F., Rice, B.L., Takahashi, S., Tatem, A.J., Wagner, C.E., Wang, L.F., &Wesolowski, A. (2022). Infectious disease in an era of global change. Nature Reviews Microbiology, 20(4), 193-205.

Chen, X., Wang, S., Tan, Y., Huang, J., Yang, X., & Li, S. (2021). Nanoparticle-Based Lateral Flow Biosensors Integrated with Loop-Mediated Isothermal Amplification for the Rapid and Visual Diagnosis of Hepatitis B Virus in Clinical Application. Front. Bioeng. Biotechnol. 9, 731415. doi:10.3389/fbioe.2021.731415

Thi, V. D., Herbst, K., Boerner, K., Meurer, M., Kremer, L. P. M., Kirrmaier, D., Freistaedter, A., Papagiannidis, D., Galmozzi, C., Stanifer, M.L., & Boulant, S. A colorimetric RT-LAMP assay and LAMP-sequencing for detecting SARS-CoV-2 RNA in clinical samples, Sci. Transl. Med.(2020).

Hu, B., Guo, H., Zhou, P., and Shi, Z.-L. (2020). Characteristics of SARS-CoV-2 and COVID-19. Nat. Rev. Microbiol. 19, 141–154. doi:10.1038/s41579-020-00459-7

Huang, W. E., Lim, B., Hsu, C. C., Xiong, D., Wu, W., Yu, Y., Jia, H., Wang, Y., Zeng, Y., Ji, M., & Chang, H. (2020). RT-LAMP for rapid diagnosis of coronavirus SARS-CoV-2. Microbial biotechnology, 13(4), 950-961.

Koczula, K. M., and Gallotta, A. (2016). Lateral Flow Assays. Lateral Flow Assays" 60 60 (1), 111–120. doi:10.1042/EBC20150012

Kralik, P., and Ricchi, M. (2017). A Basic Guide to Real Time PCR in Microbial Diagnostics: Definitions, Parameters, and Everything. Front. Microbiol. 8. doi:10.3389/fmicb.2017.00108

Lamb, L. E., Bartolone, S. N., Ward, E., &Chancellor, M. B. (2020). Rapid Detection of Novel Coronavirus/Severe Acute Respiratory Syndrome Coronavirus 2 (SARS-CoV-2) by Reverse Transcription-Loop-Mediated Isothermal Amplification. PLoS ONE 15, e0234682. doi:10.1371/journal.pone.0234682

Luo, Z., Wang, W., Ding, Y., Xie, J., Lu, J., Xue, W., Chen, Y., Wang, R., Li, X., &Wu, L. (2021). Epidemiological characteristics of infectious diseases among travelers between China and foreign countries before and during the early stage of the COVID-19 pandemic. Frontiers in Public Health, 9, 739828.

Mautner, L., Baillie, C. K., Herold, H. M., Volkwein, W., Guertler, P., Eberle, U., Ackermann, N., Sing, A., Pavlovic, M., Goerlich, O., & Busch, U. (2020). Rapid point-of-care detection of SARS-CoV-2 using reverse transcription loop-mediated isothermal amplification (RT-LAMP). Virology journal, 17, 1-14.

Wilson-Davies, E. S., Mahanama, A. I., Samaraweera, B., Ahmed, N., Friar, S., & Pelosi, E. (2021). Concerning the OptiGene Direct LAMP assay, and it's use in at-risk groups and hospital staff. Journal of Infection, 82(2), 282-327.

Alves, P. A., de Oliveira, E. G., Franco-Luiz, A. P. M., Almeida, L. T., Gonçalves, A. B., Borges, I. A., Rocha, F.D.S., Rocha, R.P., Bezerra, M.F., Miranda, P., & Capanema, F.D. (2021). Optimization and clinical validation of colorimetric reverse transcription loop-mediated isothermal amplification, a fast, highly sensitive and specific COVID-19 molecular diagnostic tool that is robust to detect SARS-CoV-2 variants of concern. Frontiers in Microbiology, 12, 713713.

Oeschger, T. M., McCloskey, D. S., Buchmann, R. M., Choubal, A. M., Boza, J. M., Mehta, S., & Erickson, D. (2021). Early warning diagnostics for emerging infectious diseases in developing into late-stage pandemics. Accounts of Chemical Research, 54(19), 3656-3666.

Pavia, A. T. (2007). Germs on a Plane: Aircraft, International Travel, and the Global Spread of Disease. J. Infect. Dis. 195 (5), 621–622. doi:10.1086/511439

Rabe, B. A., & Cepko, C. (2020). SARS-CoV-2 Detection Using Isothermal Amplification and a Rapid, Inexpensive Protocol for Sample Inactivation and Purification. Proc. Natl. Acad. Sci. U.S.A. 117, 24450–24458. doi:10.1073/pnas.2011221117

Sahoo, P. R., Sethy, K., Mohapatra, S., & Panda, D. (2016). Loop Mediated Isothermal Amplification: An Innovative Gene Amplification Technique for Animal Diseases. Vet. World 9, 465–469. doi:10.14202/vetworld.2016.465-469

Smyrlaki, I., Ekman, M., Lentini, A., Rufino de Sousa, N., Papanicolaou, N., Vondracek, M., Aarum, J., Safari, H., Muradrasoli, S., Rothfuchs, A.G., & Albert, J. (2020). Massive and rapid COVID-19 testing is feasible by extraction-free SARS-CoV-2 RT-PCR. Nature communications, 11(1), 4812.

Thompson, D., and Lei, Y. (2020). Mini Review: Recent Progress in RT-LAMP Enabled COVID-19 Detection. Sensors Actuators Rep. 2, 100017. doi:10.1016/j.snr.2020.100017

Wang, C., Horby, P. W., Hayden, F. G., & Gao, G. F. (2020). A Novel Coronavirus Outbreak of Global Health Concern. The Lancet 395 (10223), 470–473. doi:10.1016/S0140-6736(20)30185-9

Wee, S. K., Sivalingam, S. P., and Yap, E. P. H. (2020). Rapid Direct Nucleic Acid Amplification Test without RNA Extraction for SARS-CoV-2 Using a Portable PCR Thermocycler. Genes 11 (6), 664. doi:10.3390/genes11060664

World Health Organization (2021). WHO Coronavirus (COVID-19) Dashboard. Available at: https://covid19.who.int/.

Zhang, C., Zheng, T., Wang, H., Chen, W., Huang, X., Liang, J., Qiu, L., Han, D., &Tan, W. (2021). Rapid one-pot detection of SARS-CoV-2 based on a lateral flow assay in clinical samples. Analytical chemistry, 93(7), 3325-3330.

Zhang, Y., Odiwuor, N., Xiong, J., Sun, L., Nyaruaba, R. O., Wei, H., & Tanner, N. A. (2020). Rapid molecular detection of SARS-CoV-2 (COVID-19) virus RNA using colorimetric LAMP. MedRxiv, 2020-02.

Zhu, X., Wang, X., Han, L., Chen, T., Wang, L., Li, H., Li, S., He, L., Fu, X., Chen, S., & Xing, M. (2020). Multiplex reverse transcription loop-mediated isothermal amplification combined with nanoparticle-based lateral flow biosensor for the diagnosis of COVID-19. Biosensors and Bioelectronics, 166, 112437.

Lisowski, P., & Zarzycki, P. K. (2013). Microfluidic paper-based analytical devices (μPADs) and micro total analysis systems (μTAS): Development, applications and future trends. Chromatographia, 76(19-20), 1201-1214.

Whitesides, G. M. The origins and the future of microfluidics. Nature [Internet]. 2006; 442 (7101): 368–73.

Yetisen, A. K., Akram, M. S., & Lowe, C. R. (2013). based microfluidic point-of-care diagnostic devices. Lab on a Chip, 13(12), 2210-2251.

Akyazi, T., Basabe-Desmonts, L., & Benito-Lopez, F. (2018). Review on microfluidic paper-based analytical devices towards commercialisation. Analytica chimica acta, 1001, 1-17.

Nery, E. W., & Kubota, L. T. (2013). Sensing approaches on paper-based devices: a review. Analytical and bioanalytical chemistry, 405, 7573-7595.

Abe, K., Suzuki, K., & Citterio, D. (2008). Inkjet-printed microfluidic multianalyte chemical sensing paper. Analytical chemistry, 80(18), 6928-6934.

Martinez, A. W., Phillips, S. T., Butte, M. J., & Whitesides, G. M. (2007). Patterned paper as a platform for inexpensive, low-volume, portable bioassays. Angewandte Chemie, 119(8), 1340-1342.

Ornatska, M., Sharpe, E., Andreescu, D., & Andreescu, S. (2011). Paper bioassay based on ceria nanoparticles as colorimetric probes. Analytical chemistry, 83(11), 4273-4280.

Choleva, T. G., Kappi, F. A., Giokas, D. L., & Vlessidis, A. G. (2015). based assay of antioxidant activity using analyte-mediated on-paper nucleation of gold nanoparticles as colorimetric probes. Analytica Chimica Acta, 860, 61-69.

Teengam, P., Siangproh, W., Tuantranont, A., Vilaivan, T., Chailapakul, O., & Henry, C. S. (2017). Multiplex paper-based colorimetric DNA sensor using pyrrolidinyl peptide nucleic acid-

induced AgNPs aggregation for detecting MERS-CoV, MTB, and HPV oligonucleotides. Analytical chemistry, 89(10), 5428-5435.

Chen, W., Fang, X., Li, H., Cao, H., & Kong, J. (2016). A simple paper-based colorimetric device for rapid mercury (II) assay. Scientific reports, 6(1), 31948.

Wang, X., Li, F., Cai, Z., Liu, K., Li, J., Zhang, B., & He, J. (2018). Sensitive colorimetric assay for uric acid and glucose detection based on multilayer-modified paper with smartphone as signal readout. Analytical and bioanalytical chemistry, 410, 2647-2655.

Hu, J., Wang, S., Wang, L., Li, F., Pingguan-Murphy, B., Lu, T. J., & Xu, F. (2014). Advances in paper-based point-of-care diagnostics. Biosensors and Bioelectronics, 54, 585-597.

Parolo, C., de la Escosura-Muñiz, A., & Merkoçi, A. (2013). Enhanced lateral flow immunoassay using gold nanoparticles loaded with enzymes. Biosensors and Bioelectronics, 40(1), 412-416.

Sakurai, A., Takayama, K., Nomura, N., Yamamoto, N., Sakoda, Y., Kobayashi, Y., Y., Kida, H. , &Shibasaki, F. (2014). Multi-colored immunochromatography using nanobeads for rapid and sensitive typing of seasonal influenza viruses. Journal of virological methods, 209, 62-68.

Yao, L., Teng, J., Zhu, M., Zheng, L., Zhong, Y., Liu, G., Xue, F., &Chen, W. (2016). MWCNTs based high sensitive lateral flow strip biosensor for rapid determination of aqueous mercury ions. Biosensors and Bioelectronics, 85, 331-336.

Shirshahi, V., Tabatabaei, S. N., Hatamie, S., & Saber, R. (2019). Functionalized reduced graphene oxide as a lateral flow immuneassay label for one-step detection of Escherichia coli O157: H7. Journal of Pharmaceutical and Biomedical Analysis, 164, 104-111.

Kim, W., Lee, S., & Jeon, S. (2018). Enhanced sensitivity of lateral flow immunoassays by using water-soluble nanofibers and silver-enhancement reactions. Sensors and Actuators B: Chemical, 273, 1323-1327.

Rodríguez, M. O., Covián, L. B., García, A. C., & Blanco-López, M. C. (2016). Silver and gold enhancement methods for lateral flow immunoassays. Talanta, 148, 272-278.

Kasetsirikul, S., Shiddiky, M. J., & Nguyen, N. T. (2020). Challenges and perspectives in the development of paper-based lateral flow assays. Microfluidics and Nanofluidics, 24, 1-18.

Kim, T. H., Hahn, Y. K., & Kim, M. S. (2020). Recent advances of fluid manipulation technologies in microfluidic paper-based analytical devices (μPADs) toward multi-step assays. Micromachines, 11(3), 269.

Jahanshahi-Anbuhi, S., Henry, A., Leung, V., Sicard, C., Pennings, K., Pelton, R., ... & Filipe, C. D. (2014). based microfluidics with an erodible polymeric bridge giving controlled release and timed flow shutoff. Lab on a Chip, 14(1), 229-236.

Lutz, B., Liang, T., Fu, E., Ramachandran, S., Kauffman, P., & Yager, P. (2013). Dissolvable fluidic time delays for programming multi-step assays in instrument-free paper diagnostics. Lab on a Chip, 13(14), 2840-2847.

Lafleur, L. K., Bishop, J. D., Heiniger, E. K., Gallagher, R. P., Wheeler, M. D., Kauffman, P., ... & Yager, P. (2016). A rapid, instrument-free, sample-to-result nucleic acid amplification test. Lab on a Chip, 16(19), 3777-3787.

Koo, C. K., He, F., & Nugen, S. R. (2013). An inkjet-printed electrowetting valve for paper-fluidic sensors. Analyst, 138(17), 4998-5004.

Li, X., Tian, J., & Shen, W. (2010). Progress in patterned paper sizing for fabrication of paper-based microfluidic sensors. Cellulose, 17, 649-659.

Park, J., Shin, J. H., & Park, J. K. (2016). Pressed paper-based dipstick for detection of foodborne pathogens with multistep reactions. Analytical chemistry, 88(7), 3781-3788.

Preechakasedkit, P., Siangproh, W., Khongchareonporn, N., Ngamrojanavanich, N., & Chailapakul, O. (2018). Development of an automated wax-printed paper-based lateral flow device for alpha-fetoprotein enzyme-linked immunosorbent assay. Biosensors and Bioelectronics, 102, 27-32.

Fu, E., Lutz, B., Kauffman, P., & Yager, P. (2010). Controlled reagent transport in disposable 2D paper networks. Lab on a Chip, 10(7), 918-920.

Kim, T. H., Hahn, Y. K., Lee, J., Van Noort, D., & Kim, M. S. (2018). Solenoid driven pressure valve system: toward versatile fluidic control in paper microfluidics. Analytical chemistry, 90(4), 2534-2541.

Toley, B. J., Wang, J. A., Gupta, M., Buser, J. R., Lafleur, L. K., Lutz, B. R., Fu, E.,& Yager, P. (2015). A versatile valving toolkit for automating fluidic operations in paper microfluidic devices. Lab on a Chip, 15(6), 1432-1444.

Fratzl, M., Chang, B. S., Oyola-Reynoso, S., Blaire, G., Delshadi, S., Devillers, T., Ward III, T., Dempsey, N.M., Bloch, J.F.,& Thuo, M. M. (2018). Magnetic two-way valves for paper-based capillary-driven microfluidic devices. ACS omega, 3(2), 2049-2057.

Verma, M. S., Tsaloglou, M. N., Sisley, T., Christodouleas, D., Chen, A., Milette, J., & Whitesides, G. M. (2018). Sliding-strip microfluidic device enables ELISA on paper. Biosensors and Bioelectronics, 99, 77-84.

Shin, J. H., & Park, J. K. (2016). Functional packaging of lateral flow strip allows simple delivery of multiple reagents for multistep assays. Analytical chemistry, 88(21), 10374-10378.

Li, B., Yu, L., Qi, J., Fu, L., Zhang, P., & Chen, L. (2017). Controlling capillary-driven fluid transport in paper-based microfluidic devices using a movable valve. Analytical chemistry, 89(11), 5707-5712.

Liu, M., Wu, J., Gan, Y., Hanaor, D. A., & Chen, C. Q. (2018). Tuning capillary penetration in porous media: Combining geometrical and evaporation effects. International Journal of Heat and Mass Transfer, 123, 239-250.

Liu, Z., Hu, J., Zhao, Y., Qu, Z., & Xu, F. (2015). Experimental and numerical studies on liquid wicking into filter papers for paper-based diagnostics. Applied Thermal Engineering, 88, 280-287.

Liu, M., Wu, J., Gan, Y., Hanaor, D. A., & Chen, C. Q. (2016). Evaporation limited radial capillary penetration in porous media. Langmuir, 32(38), 9899-9904.

Conrath, M., Fries, N., Zhang, M., & Dreyer, M. E. (2010). Radial capillary transport from an infinite reservoir. Transport in porous media, 84, 109-132.

Madhu, N. T., Resmi, P. E., Pradeep, A., & Satheesh Babu, T. G. (2019, November). Design and simulation of fluid flow in paper based microfluidic platforms. In IOP Conference Series: Materials Science and Engineering (Vol. 577, No. 1, p. 012104). IOP Publishing.
Patari, S., & Mahapatra, P. S. (2020). Liquid wicking in a paper strip: An experimental and numerical study. ACS omega, 5(36), 22931-22939.

Ben Neriah, A., Assouline, S., Shavit, U., & Weisbrod, N. (2014). Impact of ambient conditions on evaporation from porous media. Water Resources Research, 50(8), 6696-6712.

Deegan, R. D., Bakajin, O., Dupont, T. F., Huber, G., Nagel, S. R., & Witten, T. A. (2000). Contact line deposits in an evaporating drop. Physical review E, 62(1), 756.

Mosthaf, K., Helmig, R., & Or, D. (2014). Modeling and analysis of evaporation processes from porous media on the REV scale. Water Resources Research, 50(2), 1059-1079.

Haghighi, E., Shahraeeni, E., Lehmann, P., & Or, D. (2013). Evaporation rates across a convective air boundary layer are dominated by diffusion. Water Resources Research, 49(3), 1602-1610.

Modha, S., Castro, C., & Tsutsui, H. (2021). Recent developments in flow modeling and fluid control for paper-based microfluidic biosensors. Biosensors and Bioelectronics, 178, 113026.

Shin, J. H., Park, J., Kim, S. H., & Park, J. K. (2014). Programmed sample delivery on a pressurized paper. Biomicrofluidics, 8(5).

Rivas, L., Medina-Sánchez, M., De La Escosura-Muñiz, A., & Merkoçi, A. (2014). Improving sensitivity of gold nanoparticle-based lateral flow assays by using wax-printed pillars as delay barriers of microfluidics. Lab on a Chip, 14(22), 4406-4414.

Zhang, Y., Odiwuor, N., Xiong, J., Sun, L., Nyaruaba, R. O., Wei, H., & Tanner, N. A. (2020). Rapid molecular detection of SARS-CoV-2 (COVID-19) virus RNA using colorimetric LAMP. MedRxiv, 2020-02.

Wang, S., Ge, L., Song, X., Yu, J., Ge, S., Huang, J., & Zeng, F. (2012). based chemiluminescence ELISA: lab-on-paper based on chitosan modified paper device and wax-screen-printing. Biosensors and bioelectronics, 31(1), 212-218.

Chan, S. K., & Lim, T. S. (2016). A straw-housed paper-based colorimetric antibody–antigen sensor. Analytical Methods, 8(6), 1431-1436.

Ma, L., Nilghaz, A., Choi, J. R., Liu, X., & Lu, X. (2018). Rapid detection of clenbuterol in milk using microfluidic paper-based ELISA. Food chemistry, 246, 437-441.

Chen, D., Love, K. T., Chen, Y., Eltoukhy, A. A., Kastrup, C., Sahay, G., Jeon, A., Dong, Y., Whitehead, K.A., & Anderson, D. G. (2012). Rapid discovery of potent siRNA-containing lipid nanoparticles enabled by controlled microfluidic formulation. Journal of the American Chemical Society, 134(16), 6948-6951.

Machholz, E., Mulder, G., Ruiz, C., Corning, B. F., & Pritchett-Corning, K. R. (2012). Manual restraint and common compound administration routes in mice and rats. JoVE (Journal of Visualized Experiments), (67), e2771.

Takakura H. (2021). Molecular Design of d-Luciferin-Based Bioluminescence and 1,2-Dioxetane-Based Chemiluminescence Substrates for Altered Output Wavelength and Detecting Various Molecules. Molecules (Basel, Switzerland), 26(6), 1618.

Cobb, M. (2015). Who discovered messenger RNA?. Current Biology, 25(13), R526-R532.

Sahin, U., Karikó, K., & Türeci, Ö. (2014). mRNA-based therapeutics—developing a new class of drugs. Nature reviews Drug discovery, 13(10), 759-780.

Pardi, N., Hogan, M. J., Porter, F. W., & Weissman, D. (2018). mRNA vaccines—a new era in vaccinology. Nature reviews Drug discovery, 17(4), 261-279.

Hajj, K. A., & Whitehead, K. A. (2017). Tools for translation: non-viral materials for therapeutic mRNA delivery. Nature Reviews Materials, 2(10), 1-17.

Takakura, H., Kojima, R., Ozawa, T., Nagano, T., & Urano, Y. (2012). Development of 5′-and 7′-Substituted Luciferin Analogues as Acid-Tolerant Substrates of Firefly Luciferase. ChemBioChem, 13(10), 1424-1427.

Branchini, B. R., Magyar, R. A., Murtiashaw, M. H., & Portier, N. C. (2001). The role of active site residue arginine 218 in firefly luciferase bioluminescence. Biochemistry, 40(8), 2410-2418.

Naumov, P., Ozawa, Y., Ohkubo, K., & Fukuzumi, S. (2009). Structure and spectroscopy of oxyluciferin, the light emitter of the firefly bioluminescence. Journal of the American Chemical Society, 131(32), 11590-11605.

Branchini, B. R., Ablamsky, D. M., & Rosenberg, J. C. (2010). Chemically modified firefly luciferase is an efficient source of near-infrared light. Bioconjugate chemistry, 21(11), 2023-2030.

Reddy, G. R., Thompson, W. C., & Miller, S. C. (2010). Robust light emission from cyclic alkylaminoluciferin substrates for firefly luciferase. Journal of the American Chemical Society, 132(39), 13586-13587.

Mofford, D. M., Reddy, G. R., & Miller, S. C. (2014). Aminoluciferins extend firefly luciferase bioluminescence into the near-infrared and can be preferred substrates over D-luciferin. Journal of the American Chemical Society, 136(38), 13277-13282.

Kobayashi, H., Ogawa, M., Alford, R., Choyke, P. L., & Urano, Y. (2010). New strategies for fluorescent probe design in medical diagnostic imaging. Chemical reviews, 110(5), 2620-2640.

Zhang, W., Ma, Z., Du, L., & Li, M. (2014). Design strategy for photoinduced electron transfer-based small-molecule fluorescent probes of biomacromolecules. Analyst, 139(11), 2641-2649.

Isobe, M., Sugiyama, Y., Ito, T., Ohtani, I. I., Toya, Y., Nishigohri, Y., & Takai, A. (1995). New analysis method for protein phosphatase type 2a inhibitors using the firefly bioluminescence system. Bioscience, biotechnology, and biochemistry, 59(12), 2235-2238.

Heffern, M. C., Park, H. M., Au-Yeung, H. Y., Van de Bittner, G. C., Ackerman, C. M., Stahl, A., & Chang, C. J. (2016). In vivo bioluminescence imaging reveals copper deficiency in a murine model of nonalcoholic fatty liver disease. Proceedings of the National Academy of Sciences, 113(50), 14219-14224.

Green, O., Eilon, T., Hananya, N., Gutkin, S., Bauer, C. R., & Shabat, D. (2017). Opening a gateway for chemiluminescence cell imaging: distinctive methodology for design of bright chemiluminescent dioxetane probes. ACS central science, 3(4), 349-358.

Przekora, A., Audemar, M., Pawlat, J., Canal, C., Thomann, J. S., Labay, C., Wojcik, M., Kwiatkowski, M., Terebun, P., Ginalska, G., & Duday, D. (2020). Positive effect of cold atmospheric nitrogen plasma on the behavior of mesenchymal stem cells cultured on a bone scaffold containing iron oxide-loaded silica nanoparticles catalyst. International journal of molecular sciences, 21(13), 4738.

Manaloto, E., Gowen, A. A., Lesniak, A., He, Z., Casey, A., Cullen, P. J., & Curtin, J. F. (2020). Cold atmospheric plasma induces silver nanoparticle uptake, oxidative dissolution and enhanced cytotoxicity in glioblastoma multiforme cells. Archives of Biochemistry and Biophysics, 689, 108462.

Yu, H., Wang, Y., Wang, S., Li, X., Li, W., Ding, D., Gong, X., Keidar, M., & Zhang, W. (2018). Paclitaxel-loaded core–shell magnetic nanoparticles and cold atmospheric plasma inhibit non-small cell lung cancer growth. ACS applied materials & interfaces, 10(50), 43462-43471.

Gunes, S., He, Z., van Acken, D., Malone, R., Cullen, P. J., & Curtin, J. F. (2021). Platinum nanoparticles inhibit intracellular ROS generation and protect against cold atmospheric plasma-induced cytotoxicity. Nanomedicine: Nanotechnology, Biology and Medicine, 36, 102436.

Zhu, W., Lee, S. J., Castro, N. J., Yan, D., Keidar, M., & Zhang, L. G. (2016). Synergistic effect of cold atmospheric plasma and drug loaded core-shell nanoparticles on inhibiting breast cancer cell growth. Scientific reports, 6(1), 21974.

Li, W., Yu, H., Ding, D., Chen, Z., Wang, Y., Wang, S., Li, X., Keidar, M., & Zhang, W. (2019). Cold atmospheric plasma and iron oxide-based magnetic nanoparticles for synergetic lung cancer therapy. Free Radical Biology and Medicine, 130, 71-81.

Cheng, X., Rajjoub, K., Sherman, J., Canady, J., Recek, N., Yan, D., Bian, K., Murad, F., & Keidar, M. (2015). Cold plasma accelerates the uptake of gold nanoparticles into glioblastoma cells. Plasma Processes and Polymers, 12(12), 1364-1369.

He, Z., Liu, K., Manaloto, E., Casey, A., Cribaro, G. P., Byrne, H. J., Tian, F., Barcia, C., Conway, G.E., Cullen, P.J., & Curtin, J. F. (2018). Cold atmospheric plasma induces ATP-dependent endocytosis of nanoparticles and synergistic U373MG cancer cell death. Scientific reports, 8(1), 5298.

He, Z., Liu, K., Scally, L., Manaloto, E., Gunes, S., Ng, S. W., Maher, M., Tiwari, B., Byrne, H.J., Bourke, P., & Curtin, J. F. (2020). Cold atmospheric plasma stimulates clathrin-dependent endocytosis to repair oxidised membrane and enhance uptake of nanomaterial in glioblastoma multiforme cells. Scientific reports, 10(1), 6985.